

Towards Single Spin Magnetometry at mK Temperatures

Inauguraldissertation

zur
Erlangung der Würde eines Doktors der Philosophie
vorgelegt der
Philosophisch-Naturwissenschaftlichen Fakultät
der Universität Basel

von

Dominik Rohner

aus Basel

Basel, 2020

Originaldokument gespeichert auf dem Dokumentenserver der Universität Basel

<https://edoc.unibas.ch>



This work is licensed under a Creative Commons
Attribution-NonCommercial-NoDerivatives 4.0 International License.

The complete text may be reviewed here:

<http://creativecommons.org/licenses/by-nc-nd/4.0/>

b

Genehmigt von der Philosophisch-Naturwissenschaftlichen Fakultät
auf Antrag von
Prof. Dr. Patrick Maletinsky
Prof. Dr. Martino Poggio

Basel, den 18.02.2020

Prof. Dr. Martin Spiess
Dekan

Abstract

The liquefaction of helium and the dilution refrigerator [1] have enabled cooling down objects to 4 K and even mK temperatures. Fascinating effects, such as superconductivity and strongly correlated electron systems (SCES) emerge at these temperatures and can be studied in appropriate cryogenics experiments. A powerful tool to study magnetic phenomena in such systems is a point lattice defect in diamond, the nitrogen-vacancy (NV) center. The NV center contains an electron spin that offers exceptional properties in terms of coherence time [2] and optical addressability [3], and can thereby be employed for high-performance magnetic field sensing [4]. Due to its atom-like size, the NV center can be used for nanoscale magnetometry, particularly in a scanning probe configuration where a single NV is located in a tip. This allows for nanometric spatial resolution combined with sensitivities of $\sim 1 \mu\text{T}/\sqrt{\text{Hz}}$. In this work, we pave the way towards NV magnetometry at mK temperature by implementing NV magnetometry in a dilution refrigerator, so far at 4 K, and by conducting transport experiments on a SCES at mK temperature.

At first, two phenomena in the type-II superconductor $\text{YBa}_2\text{Cu}_3\text{O}_{7-\delta}$ (YBCO) are examined at 4 K in a liquid helium bath cryostat. On the one hand, the Meissner effect is measured over a thin YBCO disk by directly imaging the penetration of magnetic fields into the superconductor. On the other hand, stray magnetic fields emerging from vortices in the same superconductor are imaged with $\sim 30 \text{ nm}$ resolution. In both cases, we benchmark our findings against existing theoretical models and use this analysis to extract quantitative values for the London penetration depth.

Additionally, we examine out-of-plane (OOP)-oriented NV centers with respect to the scanning plane, which offer benefits such as improved sensitivity and data interpretability. OOP-oriented NV centers in our fabricated scanning probes are uniquely identified and used for nanoscale magnetic imaging for the first time.

The oxide interface $\text{LaAlO}_3/\text{SrTiO}_3$, which hosts a two-dimensional electron gas that exhibits SCES physics, is examined in the dilution refrigerator. Transport measurements show signs of superconductivity and laser illumination is found to significantly increase the conductance. In terms of NV magnetometry in a dilution refrigerator at 4 K, current imaging reveals an inhomogeneous current flow through the interface. In contrast to previous findings [5], no magnetic signatures are found.

Lastly, longitudinal T_1 relaxation is studied in a high-density NV ensemble. Relaxation rates at mK are found to be lower than at 4 K, on the order of 1 Hz. However, they are still much higher than in previous findings [6], possibly explainable by spin diffusion out of the laser focus. At mK temperature, a shift of the thermal spin population is observed, corresponding to the Boltzmann distribution.

Overall, in this thesis we can present meaningful results in several areas, some of which have already been published. In the future, we will use the increased sensitivity of OOP-oriented NV magnetometers and explore magnetism and superconductivity in various exotic materials at mK temperatures.

Contents

Titel	a
Abstract	c
Contents	e
List of Abbreviations and Symbols	g
1. Introduction	1
2. NV Magnetometry and mK Dilution Refrigeration	5
2.1. The Nitrogen-Vacancy Center in Diamond	6
2.2. NV Scanning Probe Magnetometry	8
2.3. Dilution Refrigerator and mK Temperatures	10
3. Magnetometry on Superconductors	15
3.1. Theoretical Background	15
3.1.1. London Equations and Meissner Effect	16
3.1.2. Ginzburg-Landau Theory and Vortices	17
3.2. Meissner Effect and Field Penetration	19
3.2.1. Numerical Model	20
3.2.2. Superconducting Sample	21
3.2.3. Results	22
3.3. Vortex Imaging in Superconductors	26
3.3.1. Analytical Models	27
3.3.2. Results	28
3.4. Summary and Outlook	32
4. NV Magnetometry with (111) Scanning Probes	33
4.1. Introduction	33
4.1.1. Magnetic Field Reconstruction	33
4.1.2. Optical Excitation and Collection Efficiency	34
4.1.3. Sensitivity and Other Advantages	35
4.2. Results	36
4.2.1. Sample Fabrication	36
4.2.2. Optical Properties and Polarization Dependence	37
4.2.3. Out-of-Plane NV Magnetometry	39
4.3. Summary and Outlook	40

5. Oxide Interface LAO/STO	43
5.1. Theoretical Background	44
5.2. Results	47
5.2.1. Experimental Samples	47
5.2.2. Electronic Transport Measurements	48
5.2.3. Magnetic Imaging of Currents	50
5.2.4. Magnetism in LAO/STO	51
5.3. Summary and Outlook	52
6. T_1 Relaxation at mK Temperature	55
6.1. Theoretical Background	55
6.2. Results	58
6.3. Summary and Outlook	66
7. Summary and Outlook	67
7.1. Summary	67
7.2. Outlook	69
A. Appendix	75
A.1. Dilution Refrigerator Manual	75
A.2. Cooling Power	79
A.3. NV Bleaching	80
A.4. Code Snippets	82
B. Bibliography	I
Curriculum Vitae	XIII

List of Abbreviations and Symbols

Abbreviations:

AFM	atomic force microscope
DC	direct current
ES	excited state
ESLAC	excited state level anti-crossing
ESR	electron spin resonance
FWHM	full width at half maximum
GHS	gas handling system
GS	ground state
GSLAC	ground state level anti-crossing
IVC	inner vacuum chamber
MC	mixing chamber
MFM	magnetic force microscopy
MW	microwave
NA	numerical aperture
NV	nitrogen-vacancy
ODMR	optically detected magnetic resonance
OOP	out-of-plane
OVC	outer vacuum chamber
PLD	pulsed laser deposition
RF	radio-frequency
RHEED	reflection high-energy electron diffraction
SCES	strongly correlated electron system
SEM	scanning electron microscope
SQUID	superconducting quantum interference device

Chemical elements and compounds:

^3He	helium-3 isotope
^4He	helium-4 isotope
LAO	LaAlO_3
LN_2	liquid nitrogen

STO	SrTiO ₃
YBCO	YBa ₂ Cu ₃ O _{7-δ}

 Constants:

$e = 1.602 \cdot 10^{-19}$ C	elementary charge
$\gamma_{NV} = 27.9$ GHz/T	gyromagnetic ratio of NV spin
$h = 6.626 \cdot 10^{-34}$ m ² kg/s	Planck's constant
$k_B = 1.381 \cdot 10^{-23}$ m ² kg/s ² K	Boltzmann constant
$\mu_B = 9.274 \cdot 10^{-24}$ J/T	Bohr magneton
$\mu_0 = 4\pi \cdot 10^{-7}$ Tm/A	vacuum permeability
$\Phi_0 = h/2e = 2.07$ mT μ m ²	flux quantum

 Physical Quantity:

A	magnetic vector potential
B	magnetic field
B_c	critical field
B _{ext}	external bias magnetic field
B_{NV}	magnetic field projected onto NV axis
E	electric field
e _{NV}	unit vector along NV axis
η	magnetic field sensitivity
η'	magnetic moment sensitivity
γ	relaxation rate between $ m_s = -1\rangle$ and $ m_s = 1\rangle$
I_c	critical current
J	current density
J_c	critical current density
J_φ	current density along $\hat{\varphi}$
$k_{0,1}$	relaxation rate from $ m_s = 0\rangle$ to $ m_s = 1\rangle$
λ_L	London penetration depth
Λ	Pearl Length
m	magnetic moment
m_s	spin quantum number
n_s	superconducting density
Ω	relaxation rate between $ m_s = 0\rangle$ and $ m_s = \pm 1\rangle$
$P_{0,1}(\tau)$	$ m_s = 1\rangle$ population at τ after initialized in $ m_s = 0\rangle$
$\hat{\varphi}$	azimuthal coordinate in cylindrical system
$\hat{\rho}$	radial coordinate in cylindrical system
σ	standard deviation

T	temperature
T_c	critical temperature in superconductivity
T_1	longitudinal relaxation time
T_2	spin coherence time
$T_{m_s 0}$	effective temperature after initialization in $ m_s = 0\rangle$
τ	waiting time after initialization in T_1 experiment
ξ	coherence length
\hat{z}	axial coordinate in cylindrical system
z_S	distance of NV to sample surface
z_{SC}	distance of NV to superconductor

Units:

A	Ampere
g	gram
h	hour
Hz	Hertz
K	Kelvin
mK	millikelvin
m	meter
nm	nanometer
s	second
T	Tesla
μm	micrometer

1. Introduction

Curiosity has always driven humankind to expand their knowledge into more profound and more extreme areas. For instance, researches have been working hard for centuries to reach higher temperatures and higher powers, e.g. for better material processing, more efficient power plants and faster cars. Another quest in the opposite direction has been the pursuit of low temperatures. When Lord Kelvin showed in 1848 that the temperature has an absolute minimum of zero Kelvin and does not extend to negative infinity, the human curiosity was challenged to find out whether, or how close, this absolute zero could be reached. A century of research later in the 1960s, after a few milestones in between, the dilution refrigerator was invented [1, 7], which finally enabled to reach temperatures as low as one hundredth of a degree Celsius above the absolute zero.

In a different field, the search for harder materials has been pursued, e.g. to produce stronger blades, more enduring tools and higher sky-scrapers. While diamond has originally been valued for its beauty and rarity, it has soon been found to be the hardest naturally occurring material overall, and is nowadays used as standard for tools with extreme hardness requirements. Only in the 1970s, however, the optically active nitrogen-vacancy (NV) defects in diamond have been discovered [8], and found to have an electron spin with exceptional properties in terms of coherence time [2], optical addressability [3] and magnetic field sensing [4].

Since the NV center has the size of two atoms, the magnetic field is probed only within that tiny volume. Hence this time, it was the curiosity to explore the smallest dimensions which led to using the NV center in diamond as a sensor to image magnetic stray fields with nanoscale resolution. Finally, the scanning NV magnetometer was realized in 2008 when NV centers were mounted in a scanning probe configuration [9]. This allowed to approach the magnetic sample to within a few 10s of nanometers, and thereby minimize the resolution-limiting sensor-sample distance [10]. Owing to its excellent spatial resolution and magnetic field sensitivity, numerous research results have been found using NV magnetometry both at room temperature and low temperature, e.g. in nanoscale magnetism [11, 12] and current distributions [13–15].

At this point, in spite of promising physics, the mK temperature regime has remained untouched by magnetic imaging using NV centers or other magnetometers. Below 1 K or even 100 mK, thermal fluctuations are so small that even the weakest physical phenomena can occur as they are not destabilized by thermal excitation anymore. One example are strongly correlated electron systems, where the electrons cannot be described individually since they are correlated with all other electrons in the system. These strong correlations are expressed in various phenomena, for instance in a normally insulating material that suddenly becomes superconducting, such as certain oxide interfaces [16]. Other materials become magnetic [17], or obtain spontaneous supercurrents [18] and half-quantum vortices [19].

The Scope of this Thesis

In this thesis, we realize the first mK NV magnetometry setup, using NV scanning probes in a dilution refrigerator. We apply NV magnetometry to image supercurrents at 4K, and discuss the influence of the NV orientation on its magnetometry performance. We further examine a electronic and magnetic properties of a strongly correlated oxide interface, and explore the dynamics of the longitudinal T_1 relaxation at mK temperature.

In Chap. 2, we provide the theoretical basis to understand NV magnetometry and mK dilution refrigeration. The NV level structure is used to explain electron-spin resonance (ESR) and the corresponding magnetic field measurement protocol. Furthermore, the scanning probe magnetometry setup is discussed together with the effect of sensor distance on spatial resolution and sensitivity. Lastly, the principle of mK dilution refrigeration and the structure of our own cryostat and probe stick is discussed in detail.

In Chap. 3, we present our results of NV magnetometry on a type-II superconductor, extracting the London penetration depth by means of Meissner effect and vortex imaging. The Meissner effect is magnetically imaged on a superconducting disk, allowing for a detailed analysis using a numerical model based on the 2nd London equation which we implemented in this thesis. Subsequently, the superconducting current density in the disk is calculated from the experimental magnetic field map using a reverse propagation method. Furthermore, superconducting vortices are imaged with high resolution and analyzed using three analytical models, yielding a penetration depths consistent with the Meissner approach.

The realization of an optimized magnetometry configuration using out-of-plane oriented NV centers is discussed in Chap. 4. At first, the benefits of such out-of-plane magnetometers are elaborated in terms of magnetic field reconstruction and sensitivity. Furthermore, the difference between an out-of-plane and an oblique NV orientation is illustrated by a simulated magnetic field map. We fabricate the out-of-plane NV magnetometers from (111) diamond and characterize them using ESR in an aligned bias magnetic field. Excitation polarization dependent measurements allow to determine the NV orientation and demonstrate the superior optical properties of out-of-plane NVs over the oblique NV orientation in standard (100) diamond. Lastly, one- and two-dimensional magnetometry scans demonstrate the improved interpretability of the data.

Chap. 5 discusses our measurements on the oxide interface $\text{LaAlO}_3/\text{SrTiO}_3$ (LAO/STO). A theoretical introduction covers the superconductivity, the inhomogeneous current density and the magnetic dipoles previously observed in LAO/STO. Subsequently, we reproduce transport measurements on our own samples at mK temperature and find hints of superconductivity. Furthermore, photoconductivity in the oxide interface is observed upon application of green laser light. Using NV magnetometry, we examine the current flow in LAO/STO and confirm the finding of inhomogeneous current flow. Lastly, we detect no magnetic signatures at an error-bar significantly smaller than in previous research. At this point, technical challenges, such as the accelerated bleaching of the NV ESR contrast in the dilution refrigerator, prevent us from performing NV magnetometry at mK temperatures.

In Chap. 6, we discuss T_1 relaxation measurements in a high-density NV ensemble at different temperatures. At first, we provide a theoretical background to T_1 relaxation and decay rates together with previous results on NV spin relaxation at low temperatures. We demonstrate long T_1 times at 4 K and find a spin-state dependence of NV spin relaxation rates. The data can only be reproduced by a model that uses asymmetrical, time-dependent rates. A possible explanation of this surprising observation involves spin diffusion, whose dynamics is demonstrated with a numerical simulation. Furthermore, relaxation rates are measured as a function of bias magnetic field between zero and 200 mT, revealing information about the electric and magnetic field noise spectrum. Finally, at mK temperature we find even longer T_1 times on the order of seconds, and can demonstrate a shift of the equilibrium spin population towards the Boltzmann distribution.

2. NV Magnetometry and mK Dilution Refrigeration

The first production of liquid nitrogen in 1883 by Wróblewski and Olszewski established a reliable means to cool down objects to 77 K (-196°C) and triggered a race to even lower temperatures. The next milestone was set in 1908 when Kamerlingh Onnes managed to liquify helium and therefore reached 4.2 K [20]. Although liquid helium has stayed relatively expensive due to the rareness of the noble gas, it has been widely used in research and other areas where these low temperatures are required. While a decrease of the helium boiling point at lower pressures has allowed for cooling down as low as 1 K, temperatures below 1 K have remained out of reach. However, this changed in 1951 when London proposed the principle of dilution refrigeration, where an endothermic dilution of ^3He into ^4He removes heat from the environment and theoretically allows for arbitrarily low temperatures above 0 K. In 1964, the dilution refrigerator was first realized at Leiden university and temperatures in the order of 10 mK have been established [7, 21]. This has enabled the exploration of novel physics in a previously inaccessible temperature regime.

Concerning nitrogen-vacancy (NV) centers in diamond, these ultra-low temperatures lead to the absence of phonons, creating a non-zero spin polarization by thermalization. Additionally, other spins in the environment are frozen out which reduces the magnetic field noise. Accordingly, NV centers have shown improved relaxation and coherence times at mK temperatures [6, 22]. On the other hand, the prospering field of NV scanning probe magnetometry [10, 11, 14, 23] has been brought to 4 K, yielding new insights into superconductivity and 2D magnetism [12, 13, 15, 24].

However, due to technical challenges the two fields of NV magnetometry and low-temperatures research at mK temperature have not been combined yet, in spite of promising physics one could address with this combination, including strongly correlated electron systems in oxide interfaces [16], graphene [17] or unconventional superconductors [25]. As an example, the oxide interface $\text{LaAlO}_3/\text{SrTiO}_3$ (LAO/STO) has surprisingly shown signs of magnetic dipoles [26, 27] despite its superconductivity below 200 mK. In this case, NV magnetometry could shed light into this rare combination by means of nanoscale imaging of the dipoles and the superconducting currents, and could thereby determine whether coexistence or phase separation is present between the two types of order (Chap. 5). In this work, we present our path towards scanning NV magnetometry at mK temperatures.

2.1. The Nitrogen-Vacancy Center in Diamond

The NV center is a point lattice defect in diamond where two adjacent carbon atoms are replaced by a nitrogen atom and a vacancy. The NV center therefore has a symmetry axis along one of the four $\langle 111 \rangle$ crystal axes (Fig. 2.1a). In this work, we use the term NV to refer to the negatively charged NV^- state that contains a total of 6 electrons, i.e. three from the adjacent carbon atoms, two from the nitrogen atom and one extra electron obtained from a donor. The NV center possesses an electronic ground state (GS) and excited state (ES) split by 1.945 eV (637 nm) with an ES lifetime in the order of 10 ns (Fig. 2.1b). [28]

Furthermore, both electronic states hold an electronic spin triplet with $|m_s = 0\rangle$ and $|m_s = \pm 1\rangle$, denoting the magnetic quantum number with spin quantization axis along the NV axis. The GS $|m_s = 0\rangle$ and $|m_s = \pm 1\rangle$ spin states are separated by a zero-field splitting $D_0 = 2.87$ GHz, and the optical transitions between GS and ES are mostly spin-preserving. Due to an alternative, non-radiative decay channel of the ES, however, the electrons can be trapped in a "dark" singlet manifold (S), which prevents optical cycling during its long lifetime ~ 300 ns. While the singlet states decay into the three GS triplet states at comparable rates, it is fed unequally by the ES triplet states, with a much higher rate from $|m_s = \pm 1\rangle$. In two ways this effect turns out to be very useful: The different rates to and from the singlet state lead to a population transfer from $|m_s = \pm 1\rangle$ to $|m_s = 0\rangle$ under optical excitation, allowing for initialization of the NV spin into $|m_s = 0\rangle$. Furthermore, the higher decay rate from $|m_s = \pm 1\rangle$ to the long-living singlet states results in less NV fluorescence if the

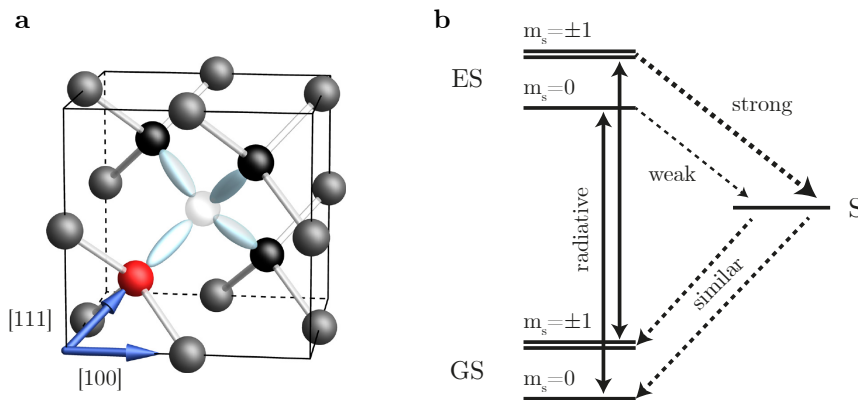


Figure 2.1.: NV center structure and energy levels. (a) Nitrogen-vacancy defect oriented along $[111]$ in a diamond unit cell. Two carbon atoms (black) are replaced by a nitrogen atom (red) and vacancy (white). The blue arrows indicate the $[100]$ and $[111]$ crystal axes. (b) Energy level of the negatively charged NV center. The electronic ground state (GS) and excited state (ES) are separated by 1.945 eV (637 nm). They form an electron spin triplet with $|m_s = 0\rangle$ and $|m_s = \pm 1\rangle$. Higher rates from $|m_s = \pm 1\rangle$ than from $|m_s = 0\rangle$ to the long-living singlet manifold, here depicted simply as S, allows for optical initialization and readout of $|m_s = 0\rangle$.

NV occupies $|m_s = \pm 1\rangle$ as compared to $|m_s = 0\rangle$, which allows for optical readout of the spin state.

Having a closer look at the GS spin triplet, we find that a DC magnetic field causes a Zeeman splitting of the $|m_s = \pm 1\rangle$ states given by $2\gamma_{\text{NV}}B_{\text{NV}}$, where $\gamma_{\text{NV}} = 28 \text{ GHz/T}$ is the gyromagnetic ratio of the NV center and B_{NV} the projection of the field onto the NV axis (Fig. 2.2a). The population can be transferred between $|m_s = 0\rangle$ and $|m_s = \pm 1\rangle$ using resonant microwave (MW) magnetic fields normal to the NV axis. A MW frequency spectrum therefore shows distinct dips in NV fluorescence count rate when the MW frequency corresponds to one of the NV spin transitions and population is transferred from $|m_s = 0\rangle$ to $|m_s = \pm 1\rangle$ (Fig. 2.2b). As a consequence, the magnetic field B_{NV} can be quantitatively measured by determining the ESR frequencies and extracting the Zeeman splitting. In general, the optimal magnetic field sensitivity is given by

$$\eta \approx \frac{\Delta\nu}{\gamma_{\text{NV}}C\sqrt{I_0}}, \quad (2.1)$$

where $\Delta\nu$ denotes the ESR linewidth, I_0 the photon count rate and C the relative contrast between on- and off-resonance MW excitation (Fig. 2.2b).

With $\Delta\nu$ in the MHz range, C in the order of 10% and I_0 in the order of 100 kcps, typical sensitivities lie in the $\mu\text{T}/\sqrt{\text{Hz}}$ range. In the ESR spectrum shown in Fig. 2.2b, however, many measurement points carry little or no information about the ESR frequency, which significantly decreases the effective magnetic field sensitivity. While this can be improved probing only one of the ESR dips using a narrow range of MW frequencies, the optimal sensitivity is only reached when probing the count rate directly at the maximal slope.

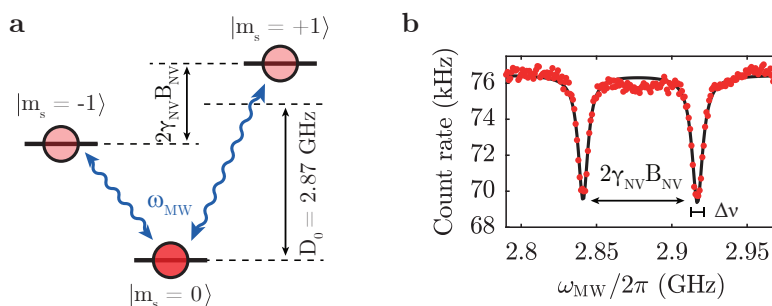


Figure 2.2.: Ground state triplet and electron spin resonance. (a) Electronic ground state spin triplet of the NV center. $|m_s = 0\rangle$ and $|m_s = \pm 1\rangle$ are separated by a zero-field splitting $D_0 = 2.87 \text{ GHz}$. The $|m_s = \pm 1\rangle$ states obtain a Zeeman splitting of $2\gamma_{\text{NV}}B_{\text{NV}}$, with γ_{NV} the gyromagnetic ratio and B_{NV} the projection of the magnetic field onto the NV axis. The spin state populations can be transferred between $|m_s = 0\rangle$ and $|m_s = \pm 1\rangle$ by a microwave (MW) magnetic field. The spin state can be read out optically due to a higher fluorescence rate in $|m_s = 0\rangle$, as indicated by the red circles. (b) NV count rate as a function of applied MW frequency. The dips in count rate indicate the electron spin resonances (ESR) between the $|m_s = 0\rangle \leftrightarrow |m_s = \pm 1\rangle$ states. The ESR linewidth is denoted by $\Delta\nu$.

In particular, two modes of NV magnetometry will be used in this work: One is the full-B method where a spectrum over one or two ESR frequencies is recorded, allowing for a direct extraction of the Zeeman splitting and for a quantitative measurement of the magnetic field over a large field range. The other is the iso-B method, where the MW is fixed at a specific frequency, probing only one particular spin-resonance magnetic field. This allows for semi-quantitative field measurements in a narrow field range, but at a higher efficiency and therefore shorter measurement times.

2.2. NV Scanning Probe Magnetometry

With the NV center wave function being localized on few diamond lattice sites and therefore sensing the magnetic field in the same small volume, the NV is in principle capable of sensing magnetic fields with sub-nm resolution. When external magnetic fields from magnetic samples or current distributions are imaged, however, the limiting factor of the spatial resolution is not the NV center size but its distance to the sample. For nanoscale magnetometry, it is therefore essential to realize a small NV-sample distance. In order to implement this, we employ diamond scanning probes with ~ 200 nm diameter nanopillars containing single NV centers ~ 10 nm from the diamond surface (Fig. 2.3). Using tuning fork based atomic force microscope (AFM) distance control, we reach an overall NV-sample distance z_{NV} in the order of 50 nm. To continuously address and read out the NV center, we position it in the focus of the optical confocal microscope and laterally scan the sample to obtain a one- or two-dimensional magnetic field map of B_{NV} . This measurement configuration constitutes a highly versatile tool to image nanoscale magnetic fields on the surface of magnetic samples or current distributions.

In the following, we consider the simple picture of a magnetic dipole to estimate the spatial resolution in magnetometry. On length scales larger than a magnetic object,

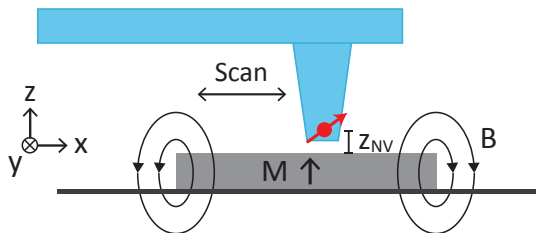


Figure 2.3.: NV scanning probe magnetometry setup. A diamond scanning probe (blue) containing a single NV spin (red) in the apex of a nanopillar. The scanning probe is scanned laterally over a magnetic sample of magnetization M . The small NV-sample distance $z_{\text{NV}} \sim 50$ nm enables imaging of nanoscale magnetic stray fields.

the magnetic stray field approaches the shape of a dipole, given by

$$\mathbf{B}_{\text{dipole}}(\mathbf{r}) = \frac{\mu_0}{4\pi r^2} \frac{3\mathbf{r}(\mathbf{m} \cdot \mathbf{r}) - \mathbf{m}r^2}{r^3}, \quad (2.2)$$

where \mathbf{m} is the magnetic moment, \mathbf{r} the spatial coordinate relative to the dipole, $r = |\mathbf{r}|$ and μ_0 the vacuum permeability. The strong $1/r^3$ distance dependence emphasizes the importance of small distances to sense weak magnetic moments. In contrast to monopole fields $\propto 1/r^2$, this implies that a larger sensor-sample distance can in general not be compensated by a larger sensor that integrates the measured signal over a larger area [29]. When laterally scanning over a magnetic dipole at distance d , the measured magnetic field shows a peak whose amplitude scales with $1/d^3$, while the width of the field (FWHM), and thus the spatial resolution, is directly given by d (Fig. 2.4a).

Furthermore, we can define a sensitivity towards magnetic dipoles, which determines the smallest magnetic dipole that can be detected within a certain time, analogously to the previously defined magnetic field sensitivity. The magnetic moment sensitivity towards an out-of-plane oriented moment of strength of m is given by

$$\eta' = \eta/B_{\text{dipole}} = \eta \cdot \frac{2\pi d^3}{\mu_0 m}. \quad (2.3)$$

The scaling of resolution and sensitivity is shown in Fig. 2.4b, illustrating that the sensitivity is the primary motivation to reduce the sensor-sample distance. This is valid for magnetic sources that are smaller than the measurement distance d and show dipolar magnetic fields.

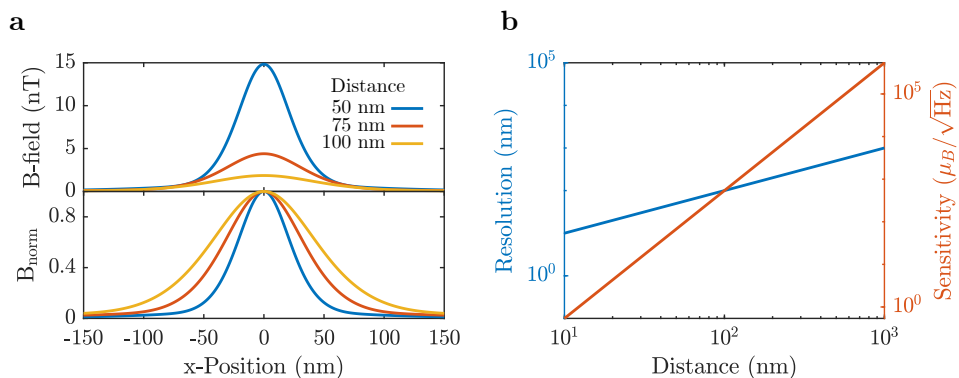


Figure 2.4.: Resolution and sensitivity towards magnetic dipoles. (a) Top: Magnitude of the magnetic field from an out-of-plane magnetic dipole of $1 \mu_B$ as a function of lateral position for distances $d = 50$ nm, 75 nm and 100 nm. The quick decay of the field $\propto 1/d^3$ illustrates the need for small distances to sense magnetic dipoles. Bottom: Same curves normalized to their maximal value. The width of the magnetic field and thus the spatial resolution scale with d (b) Plot to indicate different scaling of resolution and magnetic dipole sensitivity with distance, assuming a magnetic field sensitivity $\eta = 1 \mu\text{T}/\sqrt{\text{Hz}}$.

2.3. Dilution Refrigerator and mK Temperatures

With a liquid helium temperature of 4.2 K, extendable to 1 K at low pressure, other methods are needed to achieve temperatures below 1 K to explore novel physics e.g. of correlated electron systems. First proposed by Heinz London in 1951 and realized at Leiden university in 1964 [7], the dilution refrigeration is a widely used technique which constitutes the only method to continuously cool down large masses to ultracold temperatures < 300 mK [30]. The dilution refrigeration uses liquid ^4He and ^3He , and is based on a phase separation between a concentrated ^3He phase and a dilute, superfluid $^3\text{He}/^4\text{He}$ phase below 900 mK (Fig. 2.5a). The dilution of ^3He from the concentrated phase into the superfluid phase corresponds to an evaporation process which is endothermic and allowed due to an increase of entropy. Therefore, the endothermic dilution process takes up heat and cools down the environment, which is the driving force of the dilution refrigerator. To that end, the phase separation is controlled to be in a large-area mixing chamber, and by maintaining a continuous ^3He flow into the dilute phase the thermally connected experiment can be efficiently cooled. In general, the working principle of a dilution refrigerator is as follows (Fig. 2.5b): ^3He gas is pumped into a cryostat, liquefies as it is cooled down and forms the concentrated phase. It then reaches the mixing chamber where it enters the dilute $^3\text{He}/^4\text{He}$ phase

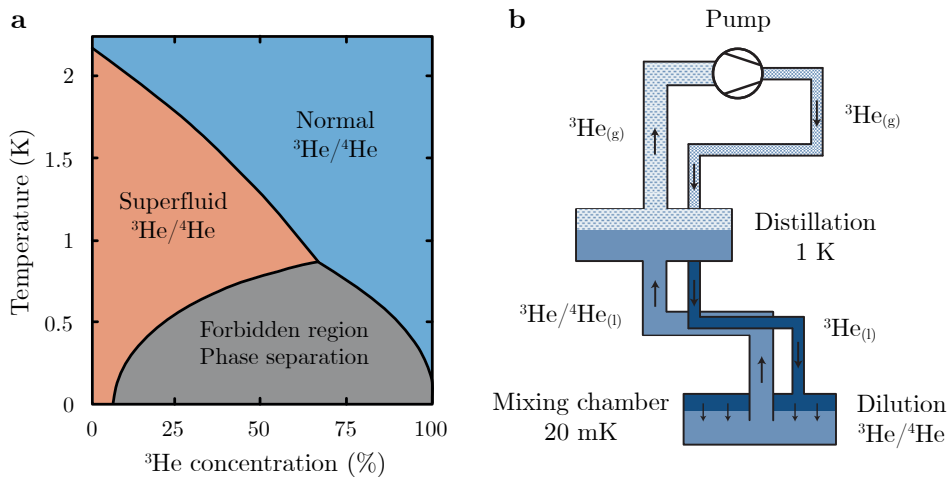


Figure 2.5.: Helium phase separation and dilution refrigeration. (a) Helium phase diagram as a function of temperature and ^3He concentration. Below 900 mK, a phase separation (grey) occurs between a concentrated ^3He phase (blue) and a superfluid, dilute $^3\text{He}/^4\text{He}$ phase (red). Together with an endothermic dilution process, this enables a controlled cooling mechanism. (b) Working principle of a dilution refrigerator. Concentrated liquid ^3He (dark blue) is diluted into the $^3\text{He}/^4\text{He}$ phase (light blue) in the the mixing chamber. After passing through the dilute phase, it is distilled in the distillation chamber using a turbo pump, and re-enters the cycle. The dotted area indicates the gas phase.

and takes up heat. After passing through the dilute phase, the ^3He reaches the distillation chamber where its removal is supported by pumping on the distillate, and then re-enters the cycle. The lower boiling temperature of ^3He compared to ^4He allows for cycling of pure ^3He .

As a concrete realization, we use a CF-CS81 dilution refrigerator from Leiden Cryogenics – a cryogen-free system that offers relatively quick top-loading of the experiment. The cryostat consists of two separate vacuum chambers, i.e. the inner vacuum chamber (IVC) which contains the mixing chamber and the experiment, and the outer vacuum chamber (OVC) used for isolation of the IVC (Fig. 2.6). The cryostat contains five massive plates spaced at 14 cm each which are thermally isolated from each other by fiberglass tubes and successively get colder. The first two plates in the OVC are the 50 K and 4 K plates which are cooled by a two-stage pulse tube refrigerator, eliminating the need for liquid helium. The 4 K plate adjoins the IVC which holds the 1 K plate, the 50 mK plate and the mixing chamber (MC) plate, which can reach temperatures as low as 20 mK at small thermal loads. While the ^3He dilution refrigeration happens on the MC plate, the cooling ^3He distillation is located in the distillation chamber on the 1 K plate. The process of the ^3He circulation is maintained by the pumps of the gas handling system (GHS) which is described later (see Fig. 2.8). Furthermore, the cryostat contains a superconducting vector magnet providing magnetic fields up to 1/1/5 Tesla ($x/y/z$) in strength.

At the heart of the mK-setup lies the probe stick which holds the experiment and enters the cryostat through 81 mm holes in the center of each plate (Fig. 2.7). The probe stick can be top-loaded into the cryostat while it is at 4 K, which allows for a relatively short turn-around time for sample exchange of one day in total. In order to deliver the cooling power to the experiment, the probe stick is thermally connected to the cold cryostat plates by a mechanical clamping mechanism actuated by pressurized gas (Fig. 2.7 left). The scanning probe setup is located at the lower end of the probe stick (Fig. 2.7 right) and consists of two stacks with three-axis piezo-driven positioners and scanners (Attocube) as well as an Attocube low-temperature objective with a working distance of 0.65 mm and a numerical aperture of 0.82. While the tip stack positions the NV center scanning probe in the focal point of the objective to enable optical readout, the sample stack holds the sample which is scanned laterally below the NV for magnetic imaging. Sample and tip are held at low temperatures by a direct thermal link through a supersonic welded copper braid from the top of the stacks to the MC plate. The optical access to the experiment through 8 mm holes in the center of each plate is realized by a confocal microscope mounted on top of the probe stick. Four coaxial cables with vacuum feed-throughs enable the delivery of MW magnetic fields to the NV center to drive ESR. Additionally, multiple electrical lines allow for control of the positioners, readout of the sensors and application of voltages and currents to the sample.

Fig. 2.8 shows the control panel of the dilution refrigerator gas handling system (GHS) with valves and pumps, as seen in the control software and on the GHS itself. In normal operation, ^3He is pumped from the distillation chamber by turbo pump S1 (Pfeiffer ATP 2300 M), backed by dry pump S3 (Edwards GX1000N) and supported by compressor S6 if necessary. It then passes a liquid nitrogen cold trap to remove other gases, re-enters the cryostat and is diluted in the mixing chamber. The software contains an "Auto" mode which automatically controls valves and pumps for cooldown

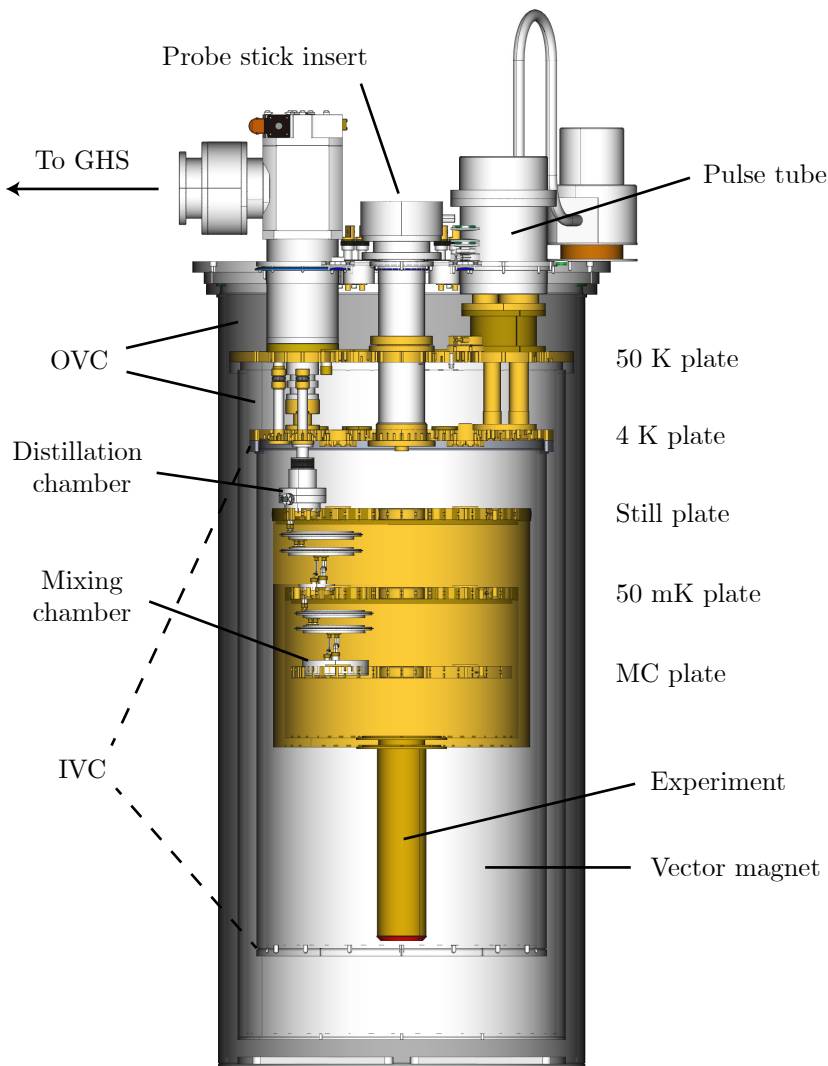


Figure 2.6.: Structure of the dilution refrigeration cryostat. Outer (OVC) and inner vacuum chamber (IVC) contain five cold plates. The pulse tube (top right) cools 50 K plate and 4 K plate, while still plate, 50 mK plate and mK plate are cooled by the $^3\text{He}/^4\text{He}$ dilution cycle managed by the gas handling system (GHS). The lowest temperature $\sim 20\text{mK}$ is reached by the ^3He dilution in the mixing chamber. The ^3He is pumped out again in the distillation chamber. The experiment is top-loaded through the probe stick insert, transferred through the center of the plates and positioned in the center of the vector magnet.

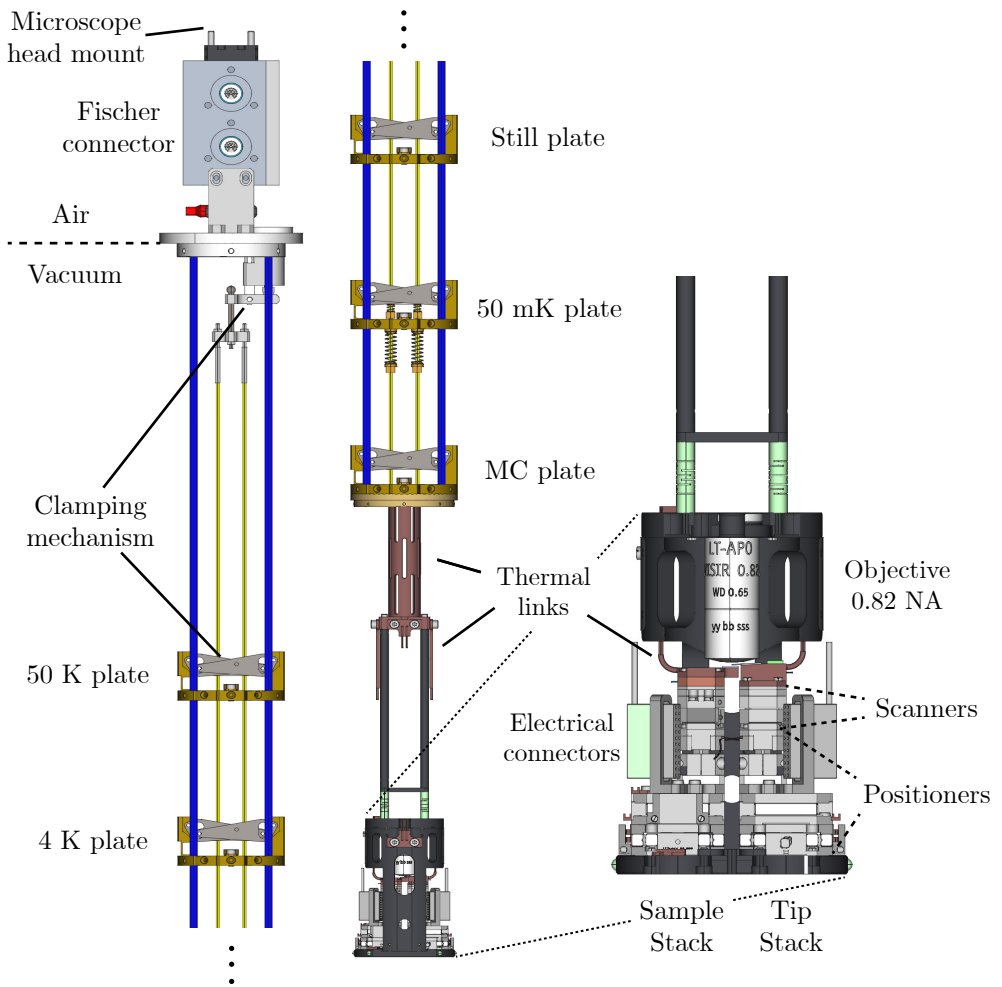


Figure 2.7.: Design of probe stick and experiment. The top-loaded probe stick is thermally connected to the cryostat plates by mechanical clamping at each plate (left). The confocal microscope head for NV center readout is mounted on top of the probe stick (top left). Electrical connections, e.g. Fischer connectors and MW lines, allow for positioning, excitation and readout of NV center, sample and sensors. The bottom of the probe stick (right) holds the scanning probe setup with tip stack, sample stack and objective. Each stack offers full three-dimensional control, containing three long-range positioners and three short-range scanners. The sample and scanning probe holders possess a direct thermal link to the MC plate.

and normal operation, as well as a recovery mode which retracts the $^3\text{He}/^4\text{He}$ mixture out of the cryostat.

Before and after operation, the helium gas is stored in a ^3He and a ^4He tank in the GHS which can be accessed through valves 9 and 10 or 9, 14, 11, respectively (c.f. Fig. 2.8). As recommended before each cooldown, the dilution cycle can be pumped out through valve A8, A9 and pump S4. Concerning the cryostat vacuum chambers, i.e. probe, OVC and IVC, they can be pumped out individually by S4 an external turbo pump. If the dilution refrigeration cycle is not running, the cryostat can still be used for operation at 4K. In this case, a small amount of helium exchange gas in the order of 10^{-2} mbar is inserted into the IVC for thermal coupling of the experiment to the pulse-tube cooled 4K plate. A detailed operation manual for the dilution refrigerator is presented in A.1. This dilution refrigerator is used for our experiments on LAO/STO (Chap. 5) and T_1 relaxation (Chap. 6), while a different low-temperature setup with a liquid helium bath cryostat (attoLiquid 1000) is used for the other experiments at 4K (Chap. 3). This latter setup is described in detail in [31] and will not be further described here.

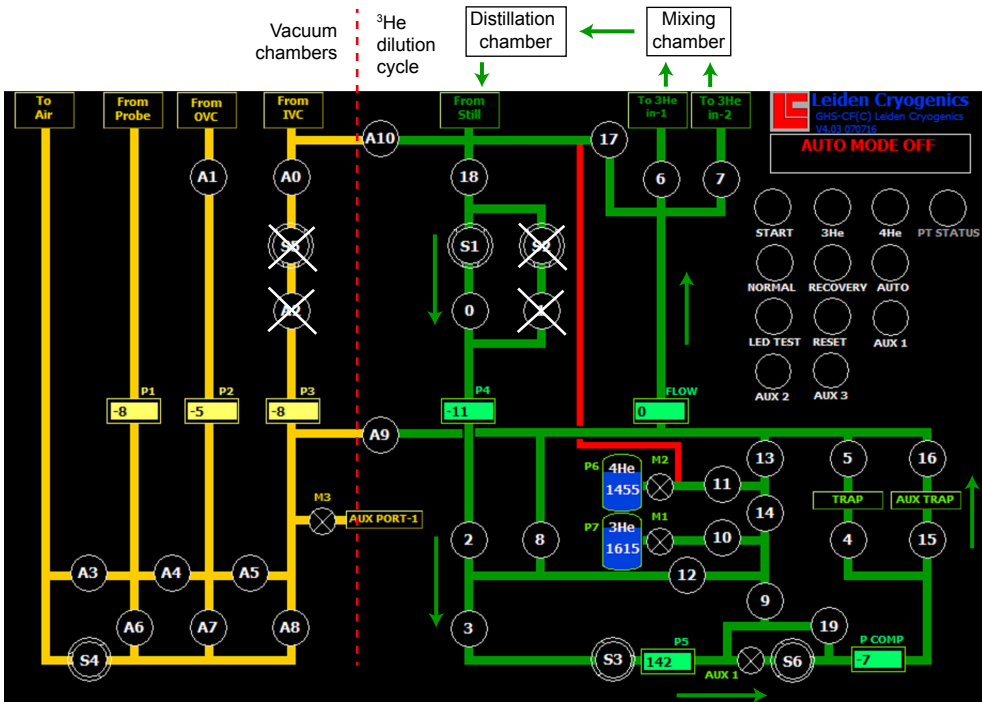


Figure 2.8.: Control panel of the gas handling system (GHS). GHS control panel of the DF-CS81 dilution refrigerator from Leiden Cryogenics. Green lines (right) represents the $^3\text{He}/^4\text{He}$ cycle for dilution refrigeration, while yellow lines (left) represents the connections to the vacuum chambers. Valves in the dilution cycle, other valves, and pumps are denoted by numbers 0-18, A0-A10, and S1-S6, respectively. The green arrows indicate the normal dilution circulation through mixing chamber, distillation chamber, pumps and cold traps.

3. Magnetometry on Superconductors

Since its beginning, superconductivity has been a prominent research field with its fascinating properties, such as perfect electrical conductivity and perfect diamagnetism. Furthermore, it has led to relevant technological developments such as SQUIDS, superconducting magnets and levitating trains. In this chapter, we discuss our experiments on superconductivity in which we observe two prominent phenomena, i.e. the Meissner effect and vortices in the superconducting condensate using nanoscale scanning NV magnetometry.

While the Meissner effect describes the magnetic field expulsion from the superconductor, a vortex constitutes a magnetic flux tube transversing the superconductor. Both phenomena occur over certain characteristic length scales. In the Meissner effect, the magnetic field can still penetrate the superconductor up to a certain depth, the London penetration depth λ_L . Analogously, the width over which magnetic fields spread in a vortex is non-zero and given by the same parameter λ_L . Furthermore, λ_L determines the superconducting density n_s (see below, Eq. 3.3). With λ_L being a central parameter of a superconductor, it is therefore of high interest to perform precise and reliable measurements of it.

However, measurements of λ_L have been challenging, and previous methods involve SQUID [32], muon spin rotation [33, 34], far-infrared spectroscopy [35], AC susceptibility [36] and electron spin resonance of Gd ions [37]. Conversely, our approach consists of quantitative nanoscale NV magnetometry, where the effects of interest, i.e. Meissner screening or vortices, are imaged in real-space. This direct approach requires minimal interpretation and offers the possibility to measure λ_L in a spatially resolved way. In the following, we first give the theoretical background necessary to understand the two phenomena, then present our results and show how we analyze them to extract λ_L . The results presented in this chapter are published in [13, 15].

3.1. Theoretical Background

Superconductivity was discovered in 1911, when Kamerlingh Onnes used liquid Helium to cool mercury to ~ 4 K. He observed that the electrical resistance of mercury suddenly vanished below a critical temperature T_c , a phenomenon that was completely unthinkable at that time (Fig. 3.1). Twenty-two years later in 1933, Meissner and Ochsenfeld discovered the other fundamental property of superconductivity, perfect diamagnetism, when they observed the expulsion of magnetic field when a material becomes superconducting. While perfect conductivity itself could explain field expulsion due to induced currents when a magnetic field is applied, it cannot explain the onset of field expulsion when the field is already present before the superconducting state – making the perfect diamagnetism, or the Meissner effect, a distinct property of superconductivity.

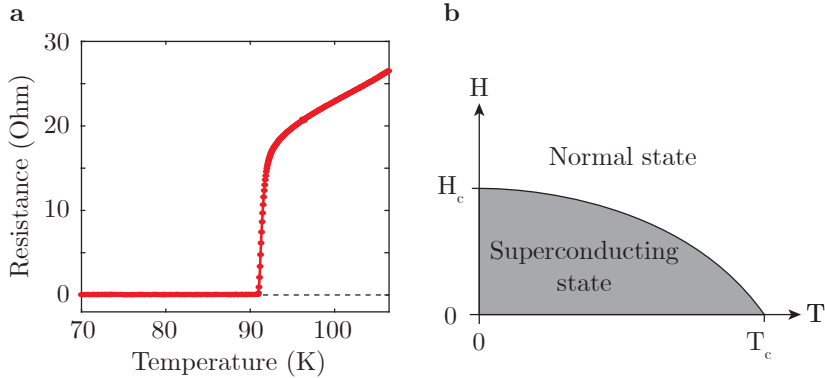


Figure 3.1.: Critical temperature and superconducting phase diagram. (a) Superconducting transition of the high-temperature superconductor $\text{YBa}_2\text{Cu}_3\text{O}_{7-\delta}$ (YBCO), which is used in our experiments (Sec. 3.2 and 3.3). The electric resistance abruptly drops to zero below the critical temperature $T_c = 91$ K. **(b)** Superconducting phase diagram, where the superconducting state is obtained below the critical temperature T_c and the critical field H_c .

3.1.1. London Equations and Meissner Effect

The two fundamental properties of superconductivity, i.e. perfect conductivity and perfect diamagnetism, were first described phenomenologically in 1935 by the London brothers. They established the two London equations which describe the current density \mathbf{J} in a superconductor in terms of electric field \mathbf{E} and magnetic field \mathbf{B} .

$$\frac{\partial \mathbf{J}}{\partial t} = \frac{n_s e^2}{m_e} \mathbf{E} = \frac{1}{\mu_0 \lambda_L^2} \mathbf{E}, \quad (3.1)$$

$$\nabla \times \mathbf{J} = -\frac{n_s e^2}{m_e} \mathbf{B} = -\frac{1}{\mu_0 \lambda_L^2} \mathbf{B}, \quad (3.2)$$

with the London penetration depth

$$\lambda_L = \sqrt{\frac{m_e}{\mu_0 e^2 n_s}}, \quad (3.3)$$

with the superconducting current density n_s , elementary charge e , electron mass m_e and vacuum permeability μ_0 . The perfect electrical conductivity is described by the 1st London equation, where an electric field causes an acceleration of the charge and the absence of electric field causes a constant current density, corresponding to zero resistance. The 2nd London equation describes the Meissner effect: A magnetic field causes a curl of current density that opposes the field, producing a magnetic field that counteracts the external field. Therefore, a superconductor fully screens the magnetic field in the bulk, provided the superconductor is large enough for the currents to entirely cancel the external field (Fig. 3.2). As seen in both equations, λ_L is a key parameter as it is connected to the superconducting density n_s and determines how

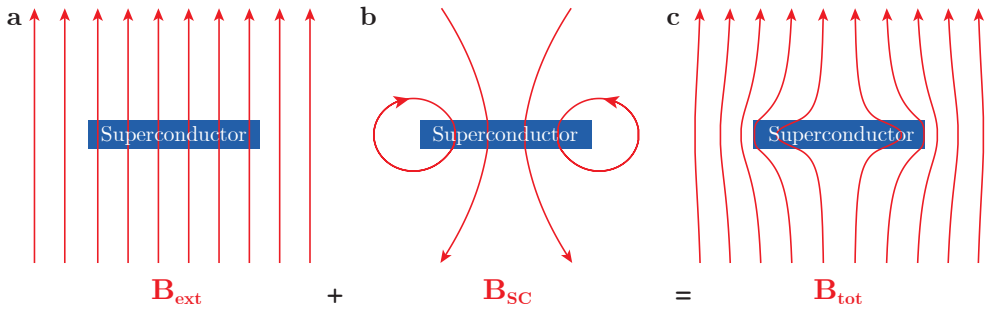


Figure 3.2.: Simulated Meissner response of a superconductor to an external magnetic field. (a) An external magnetic field B_{ext} is applied perpendicular to a superconducting disk with London penetration depth λ_L , radius $12\lambda_L$ and thickness $4\lambda_L$. The magnetic field lines are represented by the red arrows. (b) Magnetic response B_{SC} caused by superconducting currents in the disk according to the 2nd London equation. (c) Resulting magnetic field B_{tot} , illustrating the partial field expulsion and penetration. The current density and magnetic field is calculated with the numerical model described in Sec. 3.2.1.

strongly the superconductor reacts to electric and magnetic fields. Using Ampère’s law $\nabla \times \mathbf{B} = \mu_0 \mathbf{J}$, one can rewrite the 2nd London equation to

$$\nabla^2 \mathbf{B} = \frac{1}{\lambda_L^2} \mathbf{B}, \quad (3.4)$$

which illustrates the decay of the magnetic field inside the superconductor. The length scale of field penetration is found to be λ_L , therefore the name London penetration depth.

3.1.2. Ginzburg-Landau Theory and Vortices

Since the London equations are not sufficient to describe more complex phenomena such as superconducting vortices, we examine a more detailed theory of superconductivity that was established in 1950 by Ginzburg and Landau. They postulated that the superconducting state can be described by a complex order parameter $\psi(\mathbf{r}) = |\psi(\mathbf{r})|e^{i\varphi(\mathbf{r})}$, where $|\psi(\mathbf{r})|^2 = n_s(\mathbf{r})$ is the superconducting density and φ the superconducting phase. The Ginzburg-Landau equations describe the behavior of $\psi(\mathbf{r})$ inside the superconductor and result from energy minimization. They are given by

$$\alpha\psi + \beta|\psi|^2\psi + \frac{1}{2m^*}(-i\hbar\nabla - e^*\mathbf{A})^2\psi = 0, \quad (3.5)$$

$$\mathbf{J} = \frac{e^*}{m^*}|\psi|^2(\hbar\nabla\varphi - e^*\mathbf{A}) = e^*|\psi|^2\mathbf{v}_s, \quad (3.6)$$

where α and β are phenomenological parameters, \mathbf{A} the magnetic vector potential, $\mathbf{v}_s = \frac{1}{m^*}(\hbar\nabla\varphi - e^*\mathbf{A})$ the superfluid velocity and m^* and e^* effective mass and charge of a superconducting charge carrier [38]. The latter was subsequently identified as a

Cooper pair, consisting of two electrons which together form a boson and condense into a ground state described by the wavefunction ψ [39]. Neglecting the non-linear term $\beta|\psi|^2\psi$ in the first Ginzburg-Landau equation and considering weak magnetic fields, we can derive

$$\nabla^2\psi = \frac{1}{\xi^2}\psi, \quad \text{with} \quad \xi = \frac{\hbar}{\sqrt{2m^*|\alpha|}}. \quad (3.7)$$

The coherence length ξ is the characteristic length scale of the superconducting state $\psi(\mathbf{r})$ over which $\psi(\mathbf{r})$ can vary in the presence of defects or boundaries. Overall, on the one hand the superconducting density $|\psi(\mathbf{r})|^2$ determines λ_L which describes the length scale of the magnetic field penetration into the superconductor. On the other hand, ξ describes the length scale of the build-up of n_s inside the superconductor to its maximal value $|\psi|_{\text{max}}^2$. It can also be shown that ξ corresponds to the size of a Cooper pair.

The two characteristic length scales, λ_L and ξ , have further implications on superconductivity. In general, a superconductor stays in the superconducting state due to the energy gain from condensation in the bosonic ground state. In presence of magnetic fields, however, it can be energetically favourable to reduce the magnetic field energy by punctually suppressing the superconducting state and allowing field penetration through the superconductor. According to this energy trade-off between superconductivity and field penetration, we find two types of superconductors: Type-I superconductors with $\lambda_L < \xi/\sqrt{2}$, and type-II superconductors with $\lambda_L > \xi/\sqrt{2}$, where the latter permits field penetration due to a smaller cost to punctually leave the superconducting state and a larger gain from the field penetration (Fig. 3.3) [38]. This phenomenon, a non-superconducting core together with a magnetic flux penetration of one flux quantum $\Phi_0 = h/2e = 2.07 \text{ mT}\mu\text{m}^2$, constitutes a superconducting vortex and was first predicted by Abrikosov in 1957 [40]. While the size of a vortex core is

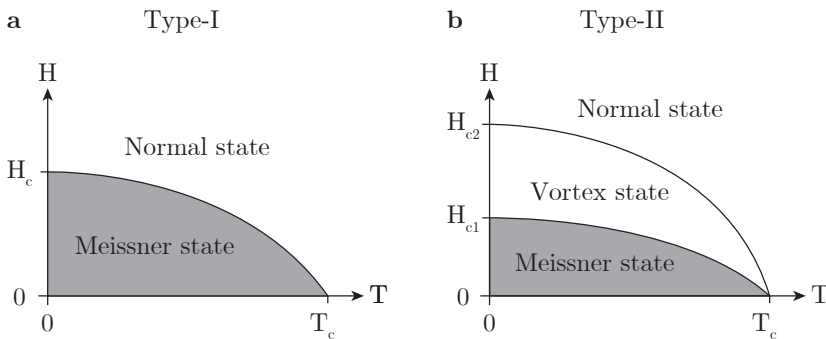


Figure 3.3.: Type-I and type-II superconductors. (a) A type-I superconductor with $\lambda_L < \xi/\sqrt{2}$ has only one critical field H_c below which it is in the regular superconducting Meissner state. (b) A type-II superconductor with $\lambda_L > \xi/\sqrt{2}$ has an additional state between two critical fields H_{c1} and H_{c2} . In this vortex state, the superconductor allows for penetration of magnetic flux tubes with non-superconducting cores.

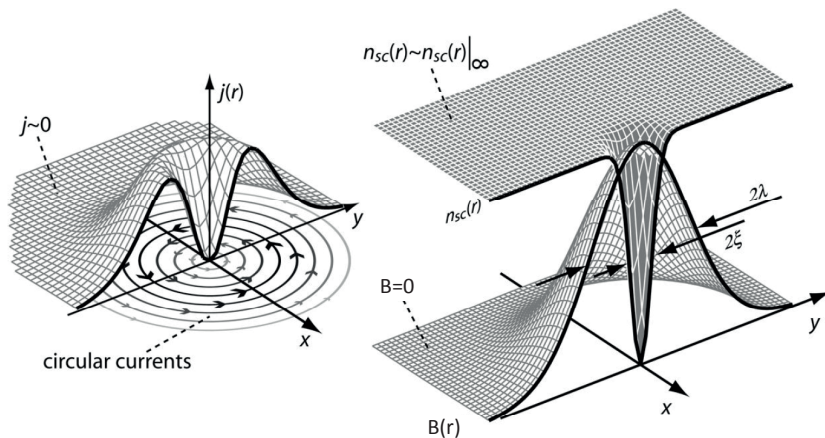


Figure 3.4.: Current density, superconducting density and magnetic field of a vortex. A superconducting vortex consists of circular currents around the non-superconducting core of width ξ . The circular currents generate a magnetic field which decays over a length scale λ_L away from the vortex core. The magnetic flux through the vortex is quantized in units of $\Phi_0 = h/2e$. Figure adapted from [41].

given by ξ , the size of the circular currents around it and the associated magnetic field is given by λ_L (Fig. 3.4).

3.2. Meissner Effect and Field Penetration

In this section, we demonstrate imaging of Meissner screening and magnetic field penetration in a disk-shaped, microscopic sample of a type-II superconductor using nanoscale NV magnetometry. We perform quantitative analysis of the data using a numerical model to accurately extract the London penetration depth λ_L . Furthermore, we determine the underlying superconducting current distribution in the superconducting sample exposed to a magnetic field [15].

The perfect diamagnetism or the Meissner effect is based on the 2nd London equation and is one of the defining properties of superconductivity. The expulsion of an external magnetic field is readily demonstrated by a levitating magnet above a cooled superconductor, which constitutes a popular school experiment. However, while the magnetic field is completely expelled from the bulk, it penetrates the superconductor at the edge up to a certain depth, the London penetration depth λ_L .

Thus far, nanoscale resolution requirements have prevented direct real-space measurements of λ_L which is in the order of 100 nm for most superconductors [35–37]. However, such real space imaging of the magnetic field would constitute a particularly reliable and straightforward method to determine λ_L , requiring minimal modelling or interpretation. We here present spatial measurements of λ_L by nanoscale imaging of the magnetic field penetration in the superconductor, as well as a measurement of the current distribution.

3.2.1. Numerical Model

In order to quantitatively interpret experimental magnetic field maps and determine the London penetration depth λ_L , we had to develop a model to calculate magnetic fields and current densities inside and outside a superconductor. Since our sample consists of a superconducting disk and we apply an out-of-plane magnetic field $\mathbf{B}_{\text{ext}} \parallel \hat{\mathbf{z}}$, we can take advantage of the cylindrical symmetry. Expressing the 2nd London equation in cylindrical coordinates, we obtain

$$\begin{aligned} \nabla \times \mathbf{J} &= \left(\frac{1}{\rho} \frac{\partial J_z}{\partial \varphi} - \frac{\partial J_\varphi}{\partial z} \right) \hat{\boldsymbol{\rho}} + \left(\frac{\partial J_\rho}{\partial z} - \frac{\partial J_z}{\partial \rho} \right) \hat{\boldsymbol{\varphi}} + \frac{1}{\rho} \left(\frac{\partial(\rho J_\varphi)}{\partial \rho} - \frac{\partial J_\rho}{\partial \varphi} \right) \hat{\mathbf{z}} \\ &= -\frac{1}{\mu_0 \lambda_L^2} \mathbf{B}, \end{aligned} \quad (3.8)$$

with ρ being the radial, φ the azimuthal, and z the axial coordinate. Considering the z -component of Eq. 3.8, and setting $J_\rho = J_z = 0$ for symmetry reasons, we obtain

$$\frac{\partial J_\varphi}{\partial \rho} + \frac{J_\varphi}{\rho} = -\frac{1}{\mu_0 \lambda_L^2} B_z. \quad (3.9)$$

Using this relation, we can build a numerical model to calculate the circular current density $J_\varphi(\rho, z)$ in a two-dimensional grid of current loops throughout the superconducting disk of radius R_{SC} and thickness d_{SC} (Fig. 3.5 a).

Expressing Eq. 3.9 in numerical form, we get

$$J_\varphi(n+1, z) = J_\varphi(n, z) - \Delta\rho \left(\frac{J_\varphi(n, z)}{\rho} + \frac{1}{\mu_0 \lambda_L^2} B_z \right), \quad (3.10)$$

where $J_\varphi(n, z)$ denotes J_φ at height z and radial distance $\rho(n)$, at the n^{th} step from the disk center outwards with step size $\Delta\rho$. Using the Euler method, the boundary condition $J_\varphi(\rho = 0, z) = 0$ and starting condition $B_z = B_{\text{ext}}$, we can calculate the current distribution in the disk. The z -component of the magnetic field is then given by $B_z(\rho, z) = B_{\text{ext}} + \sum b_z$, where $\sum b_z$ is the sum over the contributions of all the current loops in the two-dimensional grid as obtained by the Biot-Savart law. Iteratively calculating the superconducting currents and the updated magnetic fields, we arrive at the final current distribution. This allows for calculating the resulting fields inside as well as outside the superconductor, which is necessary for the analysis of experimental data. Note that while being proportional to B_{ext} , the current distribution $J(\rho, z)$ depends non-trivially on λ_L . However, due to its simplicity and reduced dimensionality, the model performs fast and can be used for data fitting, even though each function call in the fitting protocol requires a full calculation of the current distribution.

The resulting current density and magnetic field upon application of $B_{\text{ext}} = 1.7$ mT in z -direction is calculated for a superconducting disk with $R_{\text{SC}} = 3 \mu\text{m}$, $d_{\text{SC}} = 119$ nm and $\lambda_L = 249$ nm (Fig. 3.5a). These are the parameters used later in the quantitative analysis of the experimental data (Sec. 3.2.3). As expected, the magnetic field is significantly decreased in the bulk of the superconductor, however, it still amounts to $\sim 40\%$ of the applied field due to the thin shape of the superconductor (Fig. 3.5b). For complete field expulsion, a superconducting disk would have to fulfil $d_{\text{SC}}, R_{\text{SC}} \gg \lambda_L$,

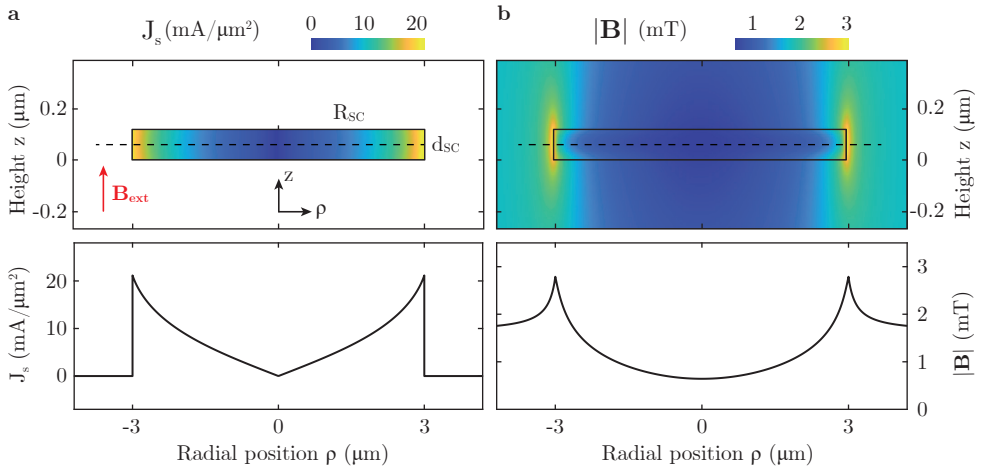


Figure 3.5.: Simulated current density and magnetic field in a superconducting disk. (a) Current density calculated in a grid of 300×24 current loops for 10 nm resolution in a superconducting disk of $R_{SC} = 3 \mu\text{m}$ and $d_{SC} = 119 \text{ nm}$. Penetration depth $\lambda_L = 249 \text{ nm}$ and external field $B_{\text{ext}} = 1.7 \text{ mT}$. The current density increases strongly towards the radial edge of the sample, while it is almost constant over z since $d_{SC} < \lambda_L$. Note that the z -coordinate is scaled up by factor 5 for better visibility. (b) Corresponding magnetic field inside and outside the superconductor, where the decreased field in the disk is a result of the Meissner effect. However, the magnetic field penetrates the superconductor over a length scale related to λ_L . Bottom panels in (a) and (b) represent current density and magnetic field in a horizontal cross section through the disk, as indicated by the dashed line.

yielding $\mathbf{B} \sim 0$ and $\mathbf{J} \sim 0$ at a distance $\gg \lambda_L$ from the edge. Despite $R_{SC} \sim 12\lambda_L$, this relation is not fulfilled due a thickness $d_{SC} \sim \lambda_L/2$. In the center of the disk, we find a linear radial increase of the current density, which corresponds to a constant curl of current and thus a constant magnetic field. Close to the edge of the superconductor, however, both $|\mathbf{B}|$ and J increase super-linearly, and the magnetic field at the edge even exceeds the applied field due to a compression of field lines by the Meissner effect. With this numerical model, we have a powerful tool to quantitatively analyze the experimental data in order to extract the London penetration depth λ_L .

3.2.2. Superconducting Sample

A suitable superconducting sample of high quality is essential to obtain accurate and reliable data on magnetic field penetration. In order to be able to fully describe the Meissner effect by the 2nd London equation and therefore with the described numerical model, we need a superconductor that is deep in the type-II regime. In this case, the coherence length ξ is negligible compared to the London penetration depth λ_L , allowing for the assumption of a constant superconducting density n_s up to the sample edge. For this reason, we perform our experiments on both Meissner effect (Sec. 3.2.3) and vortices (Sec. 3.3) in thin films of the prototypical superconductor $\text{YBa}_2\text{Cu}_3\text{O}_{7-\delta}$

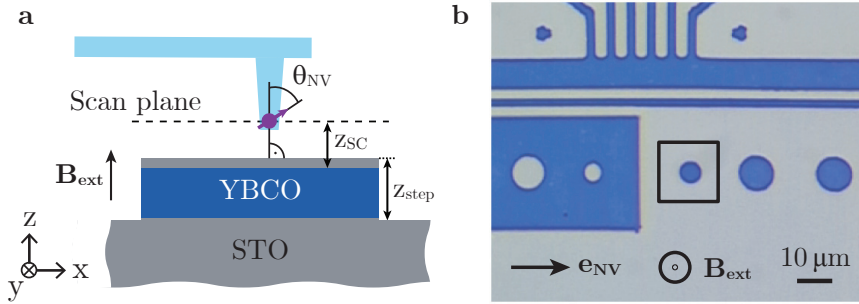


Figure 3.6.: Scanning probe magnetometer and superconducting sample geometry. (a) Cross-sectional schematic of the NV scanning probe and the superconducting YBCO disk of thickness $d_{\text{YBCO}} = 119$ nm and step size $z_{\text{step}} = 140$ nm. The NV spin is oriented at an angle $\theta_{\text{NV}} \sim 54.7^\circ$ to the sample normal and the NV-to-superconductor distance z_{SC} can be determined in the data analysis with the numerical model. (b) Layout of the YBCO film (blue) in top-view, with the disk used to study the Meissner effect highlighted in the square. The NV axis \mathbf{e}_{NV} projected onto the plane is illustrated by the arrow. The external magnetic field $B_{\text{ext}} = 1.7$ mT is applied out-of-plane as indicated in (a) and (b).

(YBCO) with a critical temperature $T_c = 91$ K (Fig. 3.1). The type-II superconductor YBCO is amongst the best-studied high- T_c superconductors and therefore well suited to demonstrate nanoscale Meissner and vortex imaging and measure λ_L . Previously reported values of λ_L for YBCO range from 91 nm to 280 nm for different levels of oxygen doping [35–37], while the coherence length ξ is reported to be in the order of 1 nm [42].

The YBCO film was fabricated by our collaborators in the groups of Profs. D. Kölle and R. Kleiner at the university of Tübingen. Starting with a (001)-oriented single crystal SrTiO_3 (STO) substrate, a film of c -axis oriented YBCO with thickness $d_{\text{SC}} = 119$ nm was grown epitaxially using pulsed laser deposition. A cover layer of 16 nm STO protects the YBCO material from oxygen diffusion. Argon ion milling was used to structure the film into stripes, areas and circles, creating a step height $z_{\text{step}} = 140$ nm (Fig. 3.6).

3.2.3. Results

We here report on the results in nanoscale imaging of the Meissner effect, its analysis and the extraction of the London penetration depth λ_L . In order to study the Meissner effect and extract λ_L , we examine a $6\ \mu\text{m}$ diameter superconducting disk and apply an out-of-plane magnetic field $B_{\text{ext}} = 1.7$ mT. The scanning probe containing a single NV center is then brought in close proximity $z_{\text{SC}} \lesssim 100$ nm of the superconductor (Fig. 3.6). At each point of a scan over the superconducting disk, we extract B_{NV} by measuring the scanning NV’s ESR Zeeman splitting (c.f. Sect. 2.1).

A representative, two-dimensional map of B_{NV} over an YBCO disk is shown in Fig. 3.7a. The high fields observed at the edge of the disk, together with a significant decrease of magnetic field in the bulk evidence field expulsion and the Meissner effect.

The striking asymmetry of B_{NV} , where the left part of the image shows significantly higher fields than the right part, is caused by the oblique measurement axis given by the NV orientation \mathbf{e}_{NV} with angle θ_{NV} to the sample normal. The measured fields B_{NV} in the right part of the disk approach zero, which, is not due to a complete suppression of the magnetic field but due to a vanishing projection of the field onto the NV axis, given by $B_{\text{NV}} = \mathbf{B} \cdot \mathbf{e}_{\text{NV}}$.

Considering $\theta_{\text{NV}} = 54.7^\circ$ as expected for (100)-oriented diamond, we can reproduce the asymmetry in a simulation based on the model presented in Sect. 3.2.1. We find excellent agreement between data and simulation using $\lambda_L = 250$ nm and $z_{\text{NV}} = 100$ nm (Fig. 3.7b). Note that the model includes a topographic step of amplitude $z_{\text{step}} = 140$ nm at the edge of the disk in order to accurately reproduce the data in that area.

In order to obtain a more quantitative analysis of the magnetic field penetration into the YBCO disk and to accurately extract λ_L , we perform a high resolution line scan over the disk (Fig. 3.8a). We find again a prominent asymmetry of B_{NV} which is readily explained by the relative orientation of the NV axis and the magnetic field lines

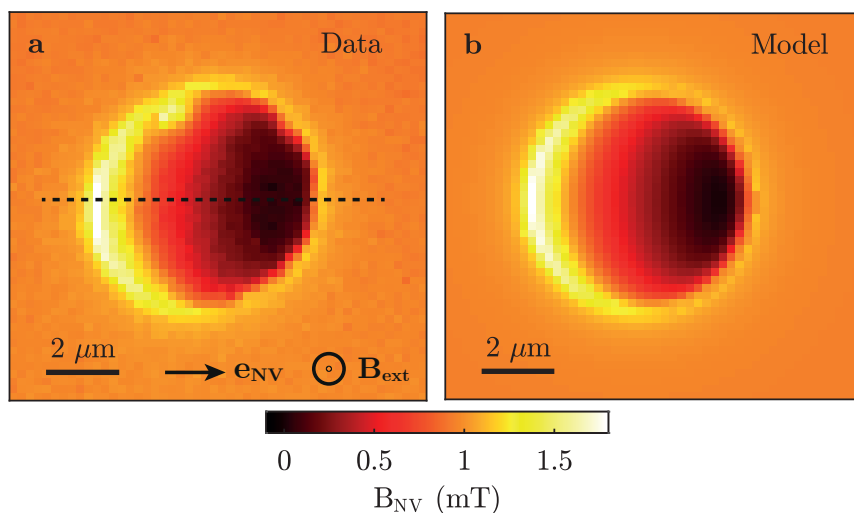


Figure 3.7.: Two-dimensional magnetometry on a superconducting YBCO disk and numerical simulation. (a) Quantitative map of the magnetic field B_{NV} measured with the scanning NV spin above an YBCO disk of radius $r_{\text{SC}} = 3 \mu\text{m}$ and thickness $d_{\text{SC}} = 119$ nm. The bias magnetic field $B_{\text{ext}} = 1.7$ mT is applied out-of-plane. Low magnetic fields are observed in the center of the disk due to Meissner screening and maximal fields at the edges of the disk due to compression of the expelled field lines. The absence of rotational symmetry of B_{NV} around the disk center is a result of the NV axis which is tilted away from the sample normal by an angle θ_{NV} . The dashed line indicates the position of the high-resolution line scan in Fig. 3.8a. (b) Corresponding two-dimensional map of B_{NV} calculated with the numerical model described in Sec. 3.2.1, using $\lambda_L = 250$ nm, $z_{\text{SC}} = 100$ nm and $\theta_{\text{NV}} = 54.7^\circ$ as manually set input parameters.

(Fig. 3.8b). Fitting this low-noise data with our numerical model (c.f. Sect. 3.2.1), we find excellent agreement and can reliably extract $\lambda_L = 249 \pm 3$ nm, $z_{\text{NV}} = 70 \pm 5$ nm and $\theta_{\text{NV}} = 55.3 \pm 0.4^\circ$. The small error bars, given by the uncertainty of the fit, demonstrate the validity of the numerical model and the capability of our experimental setup to measure quantitative nanoscale magnetic fields.

We can therefore demonstrate by means of scanning probe magnetometry that the magnetic field penetration is excellently described by the 2nd London equation, and that nanoscale field maps can be employed to accurately measure the London penetration depth λ_L . Moreover, our results agree with the fact that YBCO is a deep type-II superconductor, where the coherence length $\xi \ll \lambda_L$ is not large enough to significantly influence the current distribution.

In order to further investigate the accuracy and robustness of the obtained values for λ_L and z_{SC} , we apply a Bayesian analysis of the line scan data shown in Fig. 3.8a. This method samples through λ_L and z_{SC} and determines their likelihood to describe the data – an approach that is more computationally intensive but more robust and less prone to errors than conventional data fitting. For each pair of λ_L and z_{SC} ,

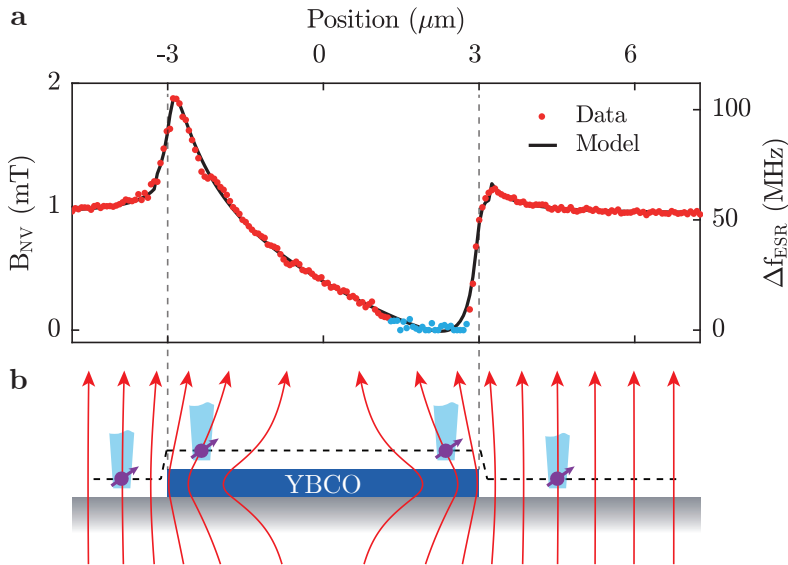


Figure 3.8.: High-resolution line scan with quantitative analysis. (a) Measurement of B_{NV} and corresponding Zeeman splitting Δf_{ESR} across the YBCO disk along the trajectory indicated in Fig. 3.7a. The black line shows the fit with the numerical model that yields a penetration depth $\lambda_L = 249 \pm 3$ nm and distance $z_{\text{SC}} = 70 \pm 5$ nm. Data points marked in blue are excluded from the fit due to insufficient Zeeman splitting. (b) Magnetic field lines (red) around the YBCO disk in the Meissner state. The scanning probe with the NV spin orientation (purple arrow) is illustrated in various positions to explain the asymmetry of B_{NV} . The dashed line illustrates the topography with step size z_{step} over which the scan is performed. This topography is taken into account in the model.

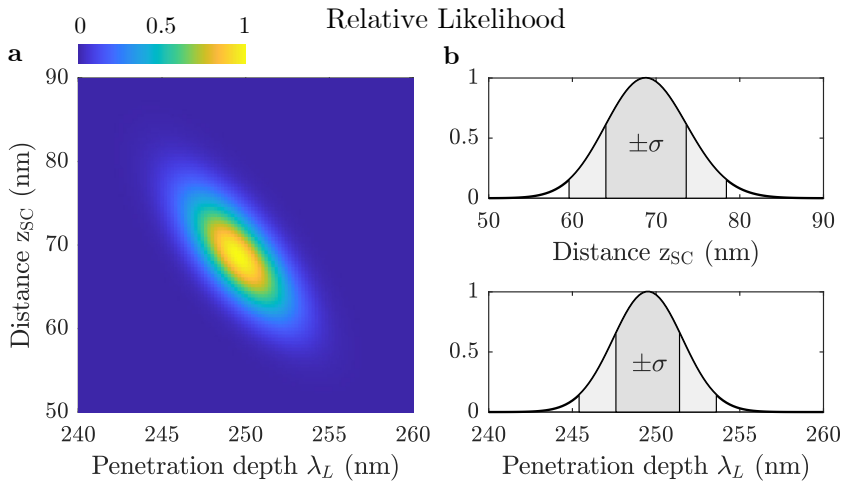


Figure 3.9.: Bayesian data analysis of λ_L and z_{NV} . (a) Relative likelihoods of a set of λ_L and z_{NV} to describe the line scan data in Fig. 3.8a. The elliptical shape of the distribution with a negative slope of -2.7 demonstrates an anticorrelation between the two parameters with a smaller uncertainty in λ_L . (b) Likelihood distribution projected onto λ_L (top) and z_{NV} (bottom). The extracted values are $\lambda_L = 249 \pm 2$ nm and $z_{SC} = 69 \pm 5$ nm, validating the previous data fit. The standard deviation is denoted by σ .

the B_{NV} curve is calculated and subtracted from the data, yielding an unnormalized likelihood of $R^{-\frac{n-1}{2}}$, with R being the residual sum of squares and n the number of data points [43]. Consistent with our initial analysis, the maximum likelihood for λ_L and z_{SC} is found at $\lambda_L = 249 \pm 2$ nm and $z_{SC} = 69 \pm 5$ nm (Fig. 3.9a). However, the distribution shows a significant anticorrelation between λ_L and z_{SC} with an aspect ratio of 3.6 and a slope $\partial z_{SC} / \partial \lambda_L = -2.7$. The anticorrelation arises from the fact that an increase of either λ_L or z_{SC} blurs the magnetic field map, implying that an increase of one parameter can be partially compensated by a decrease of the other. Overall, we obtain result with small error bars in spite of the described anticorrelation. We obtain a particularly small relative error in λ_L of only 1%, while a larger error in z_{SC} of 7% provides robustness against distance fluctuations (Fig. 3.9b). We conclude that our method of measuring the field penetration in real-space is a powerful approach to determine the London penetration depth λ_L .

In addition, we can use our quantitative data to investigate the underlying superconducting current density \mathbf{J} in the YBCO disk. To that end, we apply a back-propagation method in Fourier space to convert the two-dimensional map of B_{NV} into a corresponding map of \mathbf{J} [44]. Using the B_{NV} data shown in Fig. 3.7a, this reverse propagation yields circular currents in the YBCO disk which increase in amplitude towards the edge of the disk (Fig. 3.10). In order to gain more insight, the current density is plotted radially from the center of the disk and reveals an increasing slope of the J vs. ρ curve, again yielding good agreement with the numerical model (c.f. Fig. 3.5a).

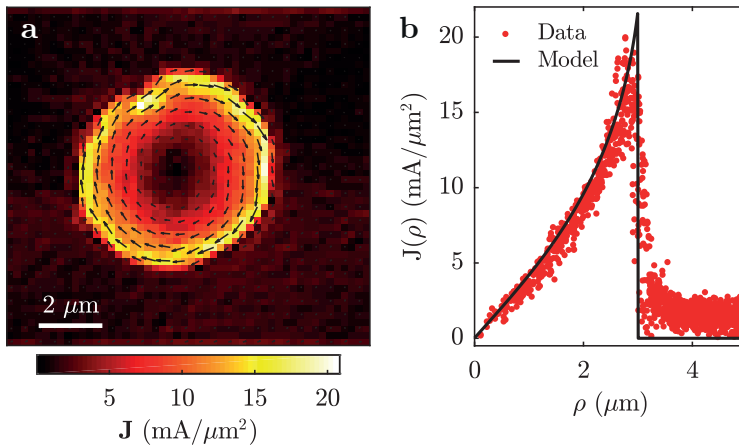


Figure 3.10.: Analysis of the current distribution in the superconducting disk. (a) Current density \mathbf{J} reconstructed by reverse-propagation of the magnetometry data in Fig. 3.7a. In accordance with the 2nd London equation, the circular current generates a magnetic field counteracting the external field B_{ext} . (b) Azimuthal average of the current density $J(\rho)$ as a function of distance ρ to the disk center, along with the current density calculated with the numerical model (c.f. Sect. 3.2.1 and Fig. 3.5a).

We have demonstrated that nanoscale NV magnetometry is a useful tool to examine the magnetic field penetration into a superconductor and to measure the London penetration depth λ_L . The value of $\lambda_L \sim 250 \text{ nm}$ measured in our YBCO sample lies within the range of previously reported values, where, however, a large variation in λ_L was reported and assigned to different YBCO qualities and measurement methods [35–37]. In the following, we will examine another phenomenon of superconductivity, i.e. vortices, in order to learn more about type-II superconductors and determine λ_L using a different approach.

3.3. Vortex Imaging in Superconductors

In this section, we present our NV magnetometry experiments on vortices in a type-II superconductor. We further discuss the analysis of the nanoscale data using three different analytical models for the determination of the London penetration depth λ_L .

Despite largely staying in the superconducting state, a type-II superconductor can incorporate local points of non-superconductivity and permit penetration of magnetic flux quanta, i.e. vortices, by maintaining circular currents. Studying nanoscale magnetic fields of superconducting vortices is highly relevant since their size and shape allow for the extraction of λ_L (c.f. Fig. 3.4) [13], and may even reveal information on the ratio between λ_L and the coherence length ξ . Further insights into microscopic mechanisms of superconductivity can be gained by examining vortex dynamics, such as vortex-vortex [45] and vortex-current interactions [46] and vortex pinning dynamics [47, 48].

Various techniques have been developed to microscopically study vortices [49–51], involving scanning tunnelling microscopy (STM) [52–54], SQUIDs [29, 46–48, 55] and magnetic force microscopy (MFM) [45, 56, 57]. While these approaches have delivered valuable insight into superconductivity and vortices, they have remained limited in terms of spatial resolution, quantitateness and invasiveness. On the other side, the NV spin is non-invasive, offers nanoscale resolution and is thus ideally suited for the quantitative study of vortex stray magnetic fields. [13].

3.3.1. Analytical Models

Magnetic stray fields emerging from superconducting vortices have been described by different analytical models, offering varying ability to reproduce experimental data and extract information about penetration depth λ_L and sensor-to-superconductor distance z_{SC} . The most straightforward model is the monopole model which describes the vortex as a magnetic monopole located at distance λ_M below the surface of the superconductor. The monopole-like field is then given by

$$\begin{aligned} B_z(\rho, z_{SC}) &= \frac{\Phi_0}{2\pi} \frac{\lambda_M + z_{SC}}{[\rho^2 + (\lambda_M + z_{SC})^2]^{3/2}}, \\ B_r(\rho, z_{SC}) &= \frac{\Phi_0}{2\pi} \frac{\rho}{[\rho^2 + (\lambda_M + z_{SC})^2]^{3/2}}, \end{aligned} \quad (3.11)$$

where $\Phi_0 = h/2e$ is the magnetic flux quantum and $2\Phi_0$ corresponds to the effective magnetic charge of the monopole. The radial coordinate and axial distance of the sensor above the superconductor are given by ρ and z_{SC} , respectively. Despite its simplicity, the monopole model is justified since a dipole-like character of the B -field is prohibited by the Meissner effect which does not allow for penetration of magnetic field through the superconductor next to the vortex. Field lines can thus not close next to the vortex, leaving a monopole field as a good approximation at distances $z_{SC} > \lambda_M$. The monopole model has been applied by various research groups to study individual vortices [58], vortex mechanics [56] and kinked vortices [57]. However, while the monopole model has been a useful tool to describe basic vortex properties and interactions, it is insufficient to analyze vortex stray fields at distances smaller than the London penetration depth λ_L , and can intrinsically not be used to determine λ_L . This arises from the fact that its only free parameter is the axial sensor-to-monopole distance $z_{SC} + \lambda_M$, making the two parameters z_{SC} and λ_M indistinguishable.

The Pearl model, on the other hand, constitutes a full analytical solution of the London equations, describing a vortex in a thin-layer type-II superconductor of thickness $d_{SC} \ll \lambda_L$ [59]. Its essential parameter is the Pearl length Λ , an effective penetration depth which is increased due to the limited current in the thin superconducting layer and given by $\Lambda = 2\lambda_L^2/d_{SC}$. Within the Pearl model, the vortex stray field is expressed as

$$A_\varphi(\rho, z_P) = \frac{\Phi_0}{2\pi} \int_0^\infty \frac{J_1(q\rho)e^{-q|z_P|}}{1 + \Lambda q} dq, \quad (3.12)$$

where J_n is the n^{th} Bessel function, A_φ denotes the azimuthal component of the magnetic vector potential \mathbf{A} , where $\mathbf{B} = \nabla \times \mathbf{A}$. Note that the sensor-to-vortex

distance z_P is the distance to the infinitely thin Pearl vortex, which for superconductors of non-zero thickness d_{SC} is not the same as z_{SC} . The Pearl model is a good approximation to the vortex stray field as long as $d_{\text{SC}} < \lambda_L$, and allows to extract both penetration depth λ_L and sensor distance z_P [13]. However, it starts to break down when $d_{\text{SC}} \gtrsim \lambda_L$, as Λ stops being a valid parameter and the thickness of the superconductor becomes relevant for the size and shape of the vortex.

In that regime, it is advantageous to use the Carneiro model which considers the thickness of the superconductor d_{SC} as a separate parameter and offers an exact, analytical solution of the vortex stray field [60]. The only condition to be fulfilled is that $\xi \ll \lambda_L$, such that the superconducting density n_s can be assumed as constant. The magnetic field of a vortex is then given by

$$\begin{aligned} B_z(\rho, z_{\text{SC}}) &= \frac{\Phi_0}{2\pi\lambda_L^2} \int_0^\infty dk \frac{kJ_0(k\rho)}{k^2 + \lambda_L^{-2}} f(k, z_{\text{SC}}), \\ B_r(\rho, z_{\text{SC}}) &= \frac{\Phi_0}{2\pi\lambda_L^2} \int_0^\infty dk \frac{J_1(k\rho)}{k^2 + \lambda_L^{-2}} g(k, z_{\text{SC}}), \end{aligned} \quad (3.13)$$

with

$$f(k, z) = c_1 e^{-kz}, \quad g(k, z) = c_1 k e^{-kz}, \quad (3.14)$$

and

$$\begin{aligned} c_1(k) &= [(k + \tau)e^{\tau d_{\text{SC}}} + (k - \tau)e^{-\tau d_{\text{SC}}} - 2k] \frac{\tau}{c_2}, \\ c_2(k) &= (k + \tau)^2 e^{\tau d_{\text{SC}}} - (k - \tau)^2 e^{-\tau d_{\text{SC}}}, \end{aligned} \quad (3.15)$$

with $\tau = \sqrt{k^2 + \lambda_L^{-2}}$. This sophisticated analytical model contains all relevant parameters and allows for a quantitative analysis of our nanoscale vortex data and a reliable extraction of λ_L and z_{SC} for superconductors deep in the type-II regime.

3.3.2. Results

In this section, we discuss the results of magnetic field measurements on vortices in a superconductor and demonstrate how their careful analysis yields essential parameters of the superconductor and sensor. Just as in the Meissner effect experiment, we use a thin-film sample of YBCO, fabricated by the same group in Tübingen (Sec. 3.2.2). Two different YBCO film thicknesses are used: $d_{\text{YBCO}} = 100$ nm in sample A and $d_{\text{YBCO}} = 150$ nm in sample B (Fig. 3.11a).

In order to create vortices in spite of the strong pinning potential in YBCO, we perform field cooling by having an external out-of-plane magnetic field $\hat{\mathbf{B}}_{\text{ext}} \parallel \hat{\mathbf{z}}$ applied before cooling the sample below T_c into the vortex phase. The strong pinning fixes the vortex positions, allowing for further cooling of the sample into the Meissner phase, and even turning off B_{ext} , without losing the vortices. The obtained vortex density is expected to be proportional to B_{ext} , and their total magnetic flux should correspond to the initially penetrating flux, which is bundled into vortices as the superconducting state is reached.

Indeed, when we apply $B_{\text{ext}} = 0.4$ mT we find a total of 27 vortices in a scan area of $15 \times 15 \mu\text{m}^2$ (Fig. 3.11b). This corresponds to a vortex density of $0.12 \mu\text{m}^{-2}$, fairly matching the expected value of $0.4 \text{ mT} / \Phi_0 = 0.19 \mu\text{m}^{-2}$, with Φ_0 being the magnetic

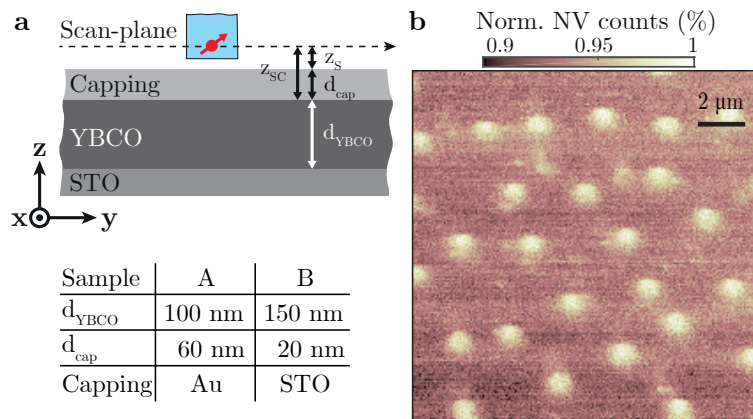


Figure 3.11.: Sample design and ensemble vortex imaging. (a) Layout of sample and scanning NV sensor. The superconducting YBCO film of thickness d_{YBCO} was grown on an STO substrate and covered by a protective STO layer of thickness d_{cap} . Key parameters for samples A and B are summarized in the table. The red arrow in the blue structure represents the NV spin in the diamond nanopillar, with the NV-to-superconductor distance z_{SC} and NV-to-surface distance z_{S} . (b) Iso-magnetic field image of an ensemble of vortices in sample A imaged after field cooling in $B_{\text{ext}} = 0.4$ mT. For the experiment, the microwave frequency ν_{MW} is fixed to the NV zero-field splitting at 2.87 GHz, while scanning the sample and monitoring the NV fluorescence. The bright areas indicate regions with high field where the Zeeman splitting exceeds the ESR half linewidth of 6 MHz, i.e. where $B_{\text{NV}} > 0.22$ mT.

flux quantum and thus the flux of a superconducting vortex. The vortices appear randomly distributed and do not form a lattice which would require a much higher density.

In order to gain more quantitative insight into the vortex stray field, we image this field with high detail (Fig. 3.12a). Owing to the close proximity of our NV sensor to the sample, we find stray magnetic fields exceeding 1 mT in the vicinity of the vortex. The stray field falls off over a length scale ~ 500 nm away from the vortex, yielding a first estimate of the penetration depth.

Despite the circular symmetry of the vortex, our data reveal a strong asymmetry of the B_{NV} map (Fig. 3.12a), again caused by the oblique measurement axis of the NV center with regard to the sample normal (see Sec. 3.2.3). Further scans examine the vortex stray field in more detail, covering a substantial volume of the stray field (Fig. 3.12b). The magnetic field falls off quickly at larger heights, implying strongly diverging field lines as already suggested by the monopole model.

Finally, in order to obtain reliable values of the London penetration depth λ_L and the NV-to-superconductor distance z_{SC} , we conduct high-resolution line scans along both symmetry axes of the B_{NV} map (Fig. 3.13). As we gain a detailed view on the symmetric and asymmetric shape of B_{NV} , we can use these high-resolution data sets for fitting with the different models discussed above (Sec. 3.3.1). Strikingly, the monopole model fails to reproduce the measured data, demonstrating the observation

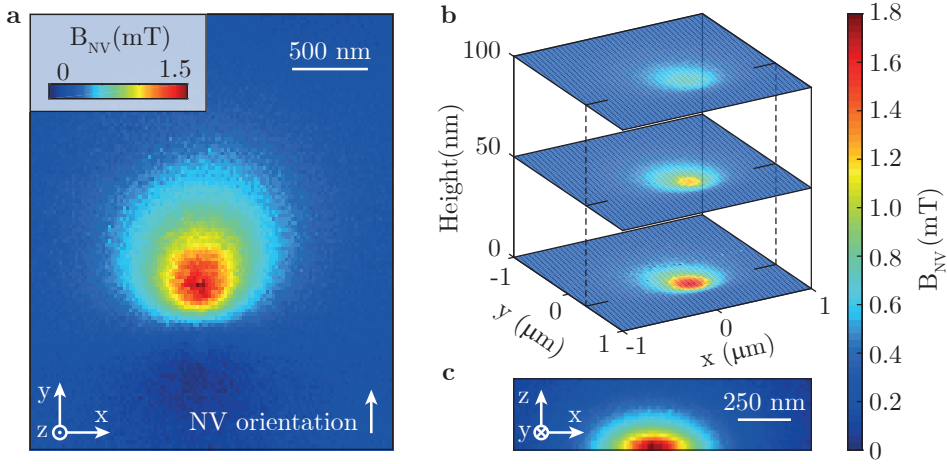


Figure 3.12.: Quantitative mapping of a vortex stray field. (a) Image of the magnetic stray-field from a single vortex in sample A, obtained with the NV magnetometer in AFM contact. The stray-field projection onto the NV axis is obtained by measuring the Zeeman splitting in optically detected ESR at each of the 120×120 points of the scan. The width of the observed vortex stray-field is in the order of the Pearl length Λ , being much larger than our spatial resolution. (b) Three-dimensional reconstruction of B_{NV} . Scans are performed at two out-of-contact heights of 50 nm and 100 nm, as indicated. (c) Vertical scan through the vortex stray-field in the x - z -plane indicated in (b).

of non-trivial vortex stray fields and small $z_{\text{SC}} \ll \lambda_M$. The fit yields an NV-to-monopole distance $z_{\text{SC}} + \lambda_M \sim 400$ nm, which is not a very useful quantity due to the poor fit quality and the indistinguishability of z_{SC} and λ_M .

The Pearl model, on the other hand, is able to reproduce the non-trivial behavior of the vortex stray field and yields an excellent fit to the data. The extracted Pearl length is $\Lambda = 840 \pm 20$ nm, which corresponds to $\lambda_L = 251 \pm 4$ nm considering the thickness $d_{\text{YBCO}} = 150$ nm, where the error bars originate from the uncertainty of the fit [13]. The NV-to-vortex distance is found to be $z_P = 104 \pm 2$ nm, which constitutes the distance to an infinitely thin superconducting layer since the Pearl model does not consider a thickness of the superconductor. In order to extract the distance of the NV to the superconductor and to the sample surface, we make the assumption that the infinitely thin Pearl vortex is placed in the center of the YBCO film. Considering $d_{\text{YBCO}}/2 = 75$ nm and $d_{\text{cap}} = 20$ nm yields an NV-to-superconductor distance $z_{\text{SC}} = 29 \pm 2$ nm and an NV-to-surface distance $z_S = 9 \pm 2$ nm.

While the Carneiro model gives a more complete solution to the vortex stray field, it shows a very similar fit quality and yields a consistent penetration depth $\lambda_L = 249 \pm 3$ nm as compared to the Pearl model. The extracted distance $z_{\text{SC}} = 51 \pm 2$ nm corresponds to $z_S = 31 \pm 2$ nm, and significantly deviates from z_{SC} as obtained with the Pearl model. However, this fit is much more reliable since the thickness of the superconducting film is not negligible compared to the distance of the sensor.

Overall, we find a high fit quality and precise measurement of λ_L with both models,

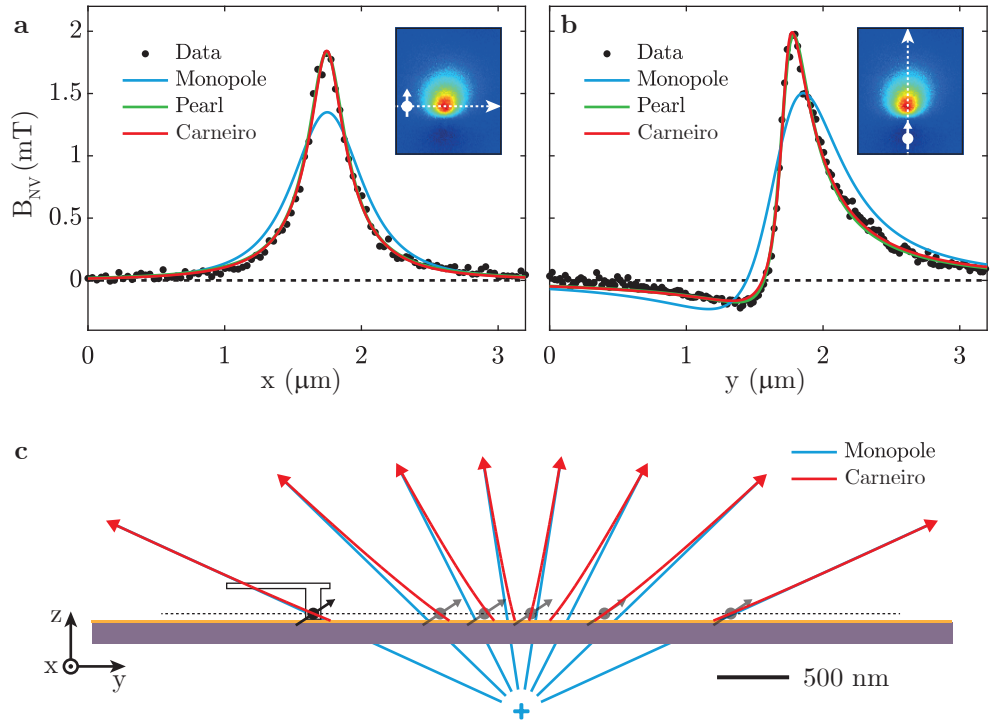


Figure 3.13.: Quantitative stray-field analysis and determination of London penetration depth. (a, b) High-resolution measurements of the magnetic field B_{NV} of a vortex in sample B along the symmetry axis x and the asymmetric axis y axis, as illustrated in the insets. The blue, green and red lines represent the best fits using the monopole, Pearl and Carneiro model, respectively. While the monopole model fails, we can reliably determine the London penetration depth $\lambda_L = 249 \pm 3$ nm and NV-to-superconductor distance $z_{\text{SC}} = 51 \pm 2$ nm with the Carneiro fit. (c) Calculated magnetic field lines of the vortex close to the superconductor using the monopole (blue) and Carneiro model (red), illustrating the strong discrepancy between the two models at small distances $z_{\text{SC}} \lesssim \Lambda$. In all panels, the small arrow illustrates the orientation of the NV spin with respect to the sample.

and a reliable measurement of z_{SC} with the Carneiro model. The extracted value of $\lambda_L = 249 \pm 3$ nm agrees excellently with the results obtained studying the field penetration in the Meissner effect, where $\lambda_L = 249 \pm 2$ nm in the same material. Moreover, due to the near-perfect fitting of the Carneiro model, we can confirm the strong type-II character of YBCO with $\xi \ll \lambda_L$, since a varying n_s would change the shape of the vortex stray field. A meaningful benchmark for magnetometry is set with the sensor-to-surface distance $z_S \sim 30$ nm, opening the door to study demanding nanoscale phenomena beyond the Meissner effect and vortex imaging.

3.4. Summary and Outlook

In this chapter, we discussed the magnetometry results on a type-II superconductor YBCO, specifically Meissner and vortex imaging. With the nanoscale resolution of the NV magnetometer, we are able to image the Meissner effect in great detail and measure the magnetic field penetration into a superconducting disk. Using a numerical model to analyze the data, we measure the London penetration depth λ_L for the first time directly in real-space using a scanning probe, opening the door for spatially resolved measurements of λ_L . The reconstructed current distribution in the superconducting disk confirms the characteristic, non-linear dependence of the current density on distance from the vortex core, as found through the 2nd London equation.

Furthermore, we have obtained meaningful results on superconducting vortices. The nanometer-range distance of the NV sensor allows for detection of the non-trivial vortex shape, clearly differing from a simple monopole. A fit with a more elaborate model yields a reliable measure of both λ_L and distance z_{NV} . The values of λ_L in YBCO obtained with the two methods, i.e. Meissner effect and vortex imaging, are consistent and found to be $\lambda_L = 249 \pm 3$ nm.

In the future, we can make further use of our nanoscale scanning probe setup, e.g. to measure spatial variations of λ_L , by examining magnetic field penetration or vortices in different positions. Patterns of superconducting edges to measure field penetration or tight vortex lattices could enable μm -range spatial resolution of λ_L .

Another interesting field is the study of different superconductor types. While the London equations do not consider the coherence length ξ , the field penetration only obeys the London equations in deep type-II superconductors. Type-I and border type-I/type-II superconductors in the Meissner state have a deeper field penetration and a different shape of the magnetic field, which could be used to determine the ratio of λ_L and ξ . Analogously, vortices in type-II superconductors close to the type-I limit have magnetic fields which are extended over a larger area and shaped differently due to the large ξ [61]. Furthermore, vortex dynamics is a promising field, where vortex-vortex [45] and vortex-current interactions [46] could be explored. Pinning strengths of vortices [47] could be studied in terms of magnetic field noise, which would be measurable with the NV center using T_1 or T_2 relaxometry [28, 62, 63].

Overall, studying these effects as a function of temperature and magnetic field, which influence λ_L and ξ , would allow for deeper insights into the physics of superconductors. Lastly, the use of an out-of-plane NV magnetometer, such as a (111)-oriented scanning probe, can provide more sensitive and easily interpretable magnetic field images and thereby enhance the visibility of the discussed effects (Chap. 4).

4. NV Magnetometry with (111) Scanning Probes

While diamond scanning probes with single NV centers in nanopillars constitute an effective approach for nanoscale magnetometry (Fig. 4.1b), all reported implementations of such scanning probes consist of diamond tips fabricated from (100)-oriented material, which is the most commonly available crystal orientation for high purity diamonds. As a result, such (100)-oriented scanning probes yield field maps of $B_{\text{NV}} = \mathbf{B} \cdot \mathbf{e}_{\text{NV}}$, where the measurement axis $\mathbf{e}_{\text{NV}} \parallel \langle 111 \rangle$ is oriented at $\theta_{\text{NV}} = 54.7^\circ$ from the sample normal (cf. Chap. 3). However, this magnetometry configuration with oblique measurement angles (Fig. 4.1c) can be significantly improved using NV centers oriented normal to the scanning plane (Fig. 4.1d). Their main benefit lies in the increased sensitivity, easily interpretable data and usability in high out-of-plane magnetic fields. The results presented in this chapter are published in [64].

4.1. Introduction

4.1.1. Magnetic Field Reconstruction

It is well established that single-axis vector magnetometers measuring the out-of-plane (OOP) magnetic field component with respect to the scanning plane represent the optimal measurement configuration [65], particularly to reconstruct the three-dimensional field components and to gain quantitative information about the underlying sample magnetization [66]. The primary reason for this is that a magnetic field map of an in-plane component (e.g. $B_x(x, y)$) contains limited information about the field maps of other components. With z being the OOP and x and y the in-plane coordinates (cf. Fig. 4.1), the relation between B_x (analogously B_y) and B_z can be derived from Laplace's equation and yields [65]

$$-k b_x(k_x, k_y) = i k_x b_z(k_x, k_y), \quad (4.1)$$

where b_x and b_z are the corresponding magnetic field maps in Fourier space, k_x and k_y the in-plane k -vector components and $k = \sqrt{k_x^2 + k_y^2}$. With $b_x \propto (k_x/k) \cdot b_z$, b_x therefore diminishes for k -vectors close to parallel to the y -axis. The magnetic field b_{NV} detected by an NV center oriented at an angle θ_{NV} to the z -axis and an azimuthal orientation along the x -axis is a combination of the OOP and the in-plane component, and therefore given by

$$|b_{\text{NV}}| = \sqrt{\cos(\theta_{\text{NV}})^2 + \sin(\theta_{\text{NV}})^2 (k_x/k)^2} \cdot |b_z|. \quad (4.2)$$

An in-plane oriented NV center with $\theta_{\text{NV}} = 90^\circ$ therefore measures a field in the range of $|b_{\text{NV}}| \in [0, |b_z|]$ depending on the in-plane orientation of the k -vector, with

an average of $0.64 |b_z|$ over k -vector orientations. In the case of NV centers in (100)-oriented diamond with $\theta_{\text{NV}} = 54.7^\circ$, we measure a magnetic field in the range of $|b_{\text{NV}}| \in [0.58, |b_z|]$ with an average of $0.80 |b_z|$ over all k -vector orientations. Together with measurement noise, this leads to a lower signal-to-noise ratio in the reconstructed magnetic field components and to an increased necessary measurement time (see Sec. 4.1.3). Therefore, the OOP vector magnetometer acquires the most information on all three magnetic field components and yields a better signal-to-noise ratio in commonly employed reverse propagation methods [44, 65].

4.1.2. Optical Excitation and Collection Efficiency

Furthermore, an OOP NV orientation is advantageous since it constitutes the optimal orientation of the NV optical dipoles with respect to the optical excitation and collection axes. It thereby optimizes the optical addressing of the NV center, removes its polarization angle dependence and further improves the magnetic field sensitivity [67]. In general, the polarization dependence of the excitation is based on the fact that the optical transitions of the NV center are related to two optical dipoles lying in the plane orthogonal to the NV axis [68]. For linearly polarized excitation with polarization angle φ_e , the NV excitation rate $P(\varphi_e)$ is proportional to the projection of the polarization onto these dipoles. Below saturation, $P(\varphi_e)$ is therefore given by [69, 70]

$$P(\varphi_e) = \chi_e(\varphi_e) P_0, \quad (4.3)$$

$$\chi_e(\varphi_e) = \sin^2(\varphi_e - \varphi_{\text{NV}}) + \cos^2(\theta_{\text{NV}}) \cos^2(\varphi_e - \varphi_{\text{NV}}),$$

where P_0 is the reference excitation rate which depends on the excitation power, and θ_{NV} and φ_{NV} are the polar and azimuthal angles of the NV axis with respect to the excitation axis (cf. Fig. 4.2c). The count rate I for unpolarized fluorescence light is then given by

$$I(\varphi_e) = \frac{1}{2} [1 + \cos^2(\theta_{\text{NV}})] \eta \chi_e P_0, \quad (4.4)$$

where η denotes the overall collection efficiency of the microscope. Therefore, the maximal and polarization independent count rate $I_{\text{max}} = \eta P_0$ is found only for the OOP NV orientation. For non-OOP orientations, the count rate depends on the excitation polarization angle φ_e . Considering the optimal count rate I_{opt} at $\varphi_e = 90^\circ + \varphi_{\text{NV}}$, non-OOP NV centers still only yield a reduced count rate

$$I_{\text{opt}} = \frac{1}{2} [1 + \cos^2(\theta_{\text{NV}})] I_{\text{max}}, \quad (4.5)$$

which is up to a factor 2 smaller than for the OOP orientation. For non-polarized (np) or randomly polarized excitation, as in case of non-optimized excitation polarization, this difference becomes even more pronounced and yields in average

$$I_{\text{np}} = \frac{1}{4} [1 + \cos^2(\theta_{\text{NV}})]^2 I_{\text{max}} \quad (4.6)$$

at excitation powers below saturation.

NV centers in common, (100)-oriented diamond are oriented at $\theta_{\text{NV}} = 54.7^\circ$ to the sample normal. Therefore, compared to OOP NVs, they yield only $I_{\text{opt}}^{100} = \frac{2}{3} I_{\text{max}}$ if the linear excitation polarization angle φ_e is optimized. Without optimized polarization angle, they yield only $I_{\text{np}}^{100} = \frac{4}{9} I_{\text{max}}$ in average. In case of excitation powers above

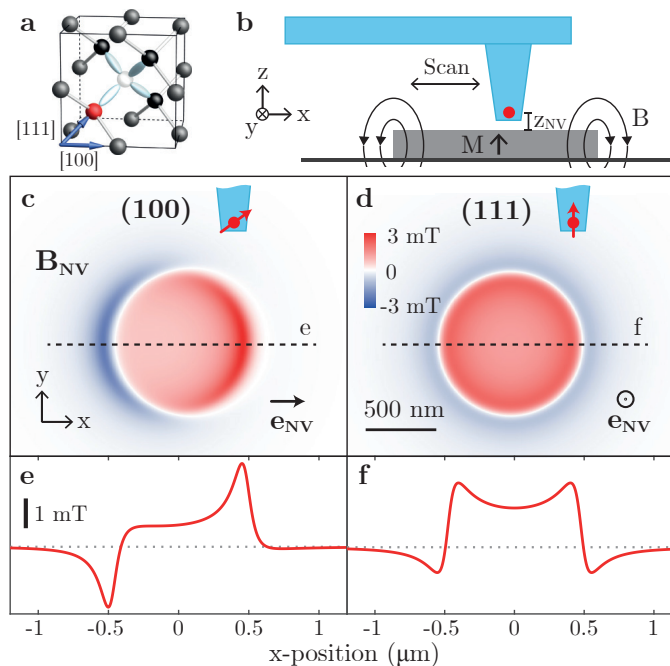


Figure 4.1: NV magnetometry setup and comparison between (100) and (111) scanning probes. (a) Atomic structure of the NV center in diamond. Nitrogen atom and vacancy are represented by red and white spheres, with the [111] and [100] directions as indicated. (b) Scanning probe magnetometry with a single NV center (red point) in a diamond nanopillar. The NV center is scanned at a height z_{NV} over a thin-film magnet. (c) Calculated magnetic field map $B_{NV}(x, y)$ for a (100)-oriented diamond tip, with $z_{NV} = 70$ nm, disk diameter $1 \mu\text{m}$, and areal magnetization $M = 1$ mA. (d) Same as in (c) but for an out-of-plane (OOP)-oriented NV in a (111)-oriented diamond tip. (e, f) Linecuts through the maps shown in (c, d). Only for the OOP-oriented NV magnetometer, the rotational symmetry of the sample is reflected in B_{NV} .

saturation, the dependence on the excitation polarization angle is lost and the same count rate I_{opt} is obtained as for the optimized polarization angle.

4.1.3. Sensitivity and Other Advantages

Overall, we can make an estimate of the combined magnetometry performance in terms of count rate and magnetic signal, comparing (111) scanning probes with OOP-oriented NVs to conventional (100) scanning probes. Without using a dedicated excitation polarization control and considering a small excitation power limited by an acceptable heat load on the sample, we obtain an average $I_{\text{np}}^{100} = \frac{4}{9} I_{\text{max}}$ as discussed in Sec. 4.1.2. Furthermore, considering the measured magnetic field $|b_{NV}|$ derived in Sec. 4.1.1, we can estimate the necessary measurement time t for a given signal-to-noise ratio, which scales as $t \propto |b_{NV}|^{-2} I^{-1}$. Without optimized excitation polarization,

we find that (111) scanning probes offer 3.5 times shorter measurement times than conventional (100) scanning probes, averaged over all in-plane k -vector orientations. In case φ_e is optimized or in conditions where high excitation powers can be applied, the resulting measurements times are still 2.3 times shorter with OOP NV scanning probes. A further advantage is the equal sensitivity towards magnetic fields in all in-plane directions, which is essential if the sample orientation cannot be controlled, or if the sample needs to be probed in different directions.

Additionally, stray field maps obtained with non-OOP magnetometers exhibit distortions which complicate interpretation of their maps, especially if the angle of the measured field component is not exactly known (Fig. 4.1c,d). Besides these general advantages of an OOP measurement axis, the photophysics of the NV center demands that the NV axis \mathbf{e}_{NV} is well aligned to external fields once they are $\gtrsim 10$ mT, to maintain practicable ODMR contrast [71]. However, studies of many prominent physical phenomena, such as quantum Hall effect [72] or Skyrmions [73], require large OOP bias magnetic fields, which is only compatible with an OOP NV orientation.

Motivated by these considerations, we present the first experimental realization of diamond scanning probes with OOP-oriented NV centers. These devices require the use of (111)-oriented diamond for scanning probe fabrication, where one of the four possible NV orientations is OOP with regard to the scanning plane. Diamond nanopillars on (111)-oriented diamond have already been demonstrated [67], however no scanning probe fabrication or NV magnetometry has been realized with this crystal orientation. Here, we overcome this shortcoming, fabricate and characterize (111)-oriented, all-diamond scanning probes and experimentally demonstrate their performance in nanoscale magnetic imaging.

4.2. Results

4.2.1. Sample Fabrication

The starting point of our fabrication is electronic grade, (111)-oriented single crystal diamond (IIa technologies), which was laser-cut and polished to a $50\ \mu\text{m}$ thin diamond plate. Near-surface NV centers with a depth ~ 10 nm are created by ion-implantation with ^{14}N at 6 keV and a density of $3 \times 10^{11}\ \text{cm}^{-2}$, followed by vacuum annealing at 800°C . The cantilevers and nanopillars are etched into the diamond by two steps of reactive ion etching (RIE) inductively coupled plasma (ICP), using the E-Beam resist HSQ as a mask in the oxygen plasma [23]. We obtain arrays of $10\ \mu\text{m} \times 20\ \mu\text{m}$ sized cantilevers with ~ 300 nm diameter nanopillars, where cantilevers and pillars have a depth of $2\ \mu\text{m}$ each (Fig. 4.2a). An optimized etching plasma and mask shape is used to obtain a parabolic-like nanopillar shape, which offers better waveguiding properties and collection efficiency [74]. The resulting structures are subsequently released by a deep etch of $\sim 45\ \mu\text{m}$ to a free-standing structure, where the diamond cantilevers are attached to a diamond holding frame by thin bridges only (Fig. 4.2a). For scanning probe magnetometry, individual cantilevers are detached from bulk diamond using micromanipulators and attached to a quartz tuning fork for AFM distance control during the magnetometry scans [23].

To characterize the resulting NV scanning probes, we employ a homebuilt confocal optical microscope operating under ambient conditions (Fig. 4.2b). The NV centers

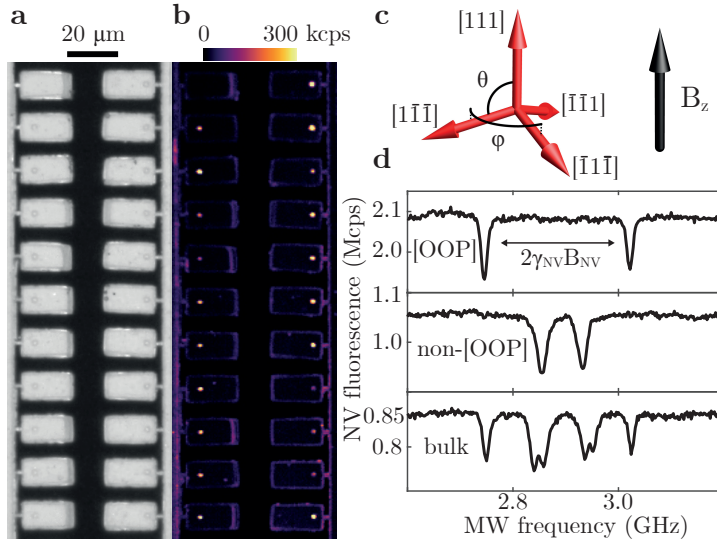


Figure 4.2.: Fabricated scanning probes and characterization of NV orientations. (a) Optical microscopy image of an array of the finalized scanning probes fabricated from a (111)-oriented single crystal diamond. (b) Same area as in (a) imaged by confocal microscopy. The bright dots on the cantilevers correspond to nanopillars containing varying numbers of NV centers. (c) Visualization of the NV orientations and the applied magnetic field in z -direction. φ and θ denote the angles in the spherical coordinate system. (d) ODMR spectra recorded on differently oriented NV centers in scanning probes and bulk diamond. An OOP bias magnetic field of ~ 5 mT yields an almost perfect overlap of the ODMR frequencies of the three non-OOP NV orientations.

are addressed by a microscope objective with numerical aperture 0.8, excited non-resonantly with a green laser (532 nm) and the NV fluorescence is collected between 600 nm and 800 nm wavelength. A metal wire placed close to the focal spot of the microscope is used to apply microwave magnetic fields to drive NV spins for ODMR.

Our fabrication results in a few hundred scanning probes on the diamond chip, a subset of which is investigated for the present study. Applying a magnetic field along the sample normal allows us to discriminate the OOP-oriented NVs (i.e. [111]) from the non-OOP-oriented ones (i.e. $[1\bar{1}\bar{1}]$, $[\bar{1}1\bar{1}]$ and $[\bar{1}\bar{1}1]$) (Fig. 4.2c). Specifically, ODMR of OOP-oriented NVs shows a Zeeman splitting of $2\gamma_{\text{NV}}B_{\text{NV}}$, with the gyromagnetic ratio $\gamma_{\text{NV}} = 28$ GHz/T, which is three times larger than that of the other three orientations (Fig. 4.2d).

4.2.2. Optical Properties and Polarization Dependence

To gain more insight into the properties of (111)-oriented NV scanning probes, we explore the excitation polarization dependence of NV fluorescence under linearly polarized excitation in our devices. As will be shown, this allows for a microwave-free discrimination of the four possible NV orientations. In (111)-oriented diamond, we

find the OOP-oriented [111] NV centers on the one hand, and the three non-OOP orientations $[\bar{1}\bar{1}\bar{1}]$, $[\bar{1}\bar{1}\bar{1}]$ and $[\bar{1}\bar{1}\bar{1}]$ with $\theta_{\text{NV}} = 70.5^\circ$ on the other hand. While the former have the maximal count rate I_{max} which is independent of excitation polarization angle φ_e , the latter show a polarization angle dependence which corresponds to the NV excitation rate expressed in Eq. (4.3) and (4.4). At excitation powers below saturation, the count rate of these non-OOP-oriented NV centers is therefore given by

$$I^{\bar{1}\bar{1}\bar{1}}(\varphi_e) = I_{\text{opt}}^{\bar{1}\bar{1}\bar{1}} \left[\sin^2(\varphi_e - \varphi_{\text{NV}}) + \frac{1}{9} \cos^2(\varphi_e - \varphi_{\text{NV}}) \right], \quad (4.7)$$

where $\bar{1}\bar{1}\bar{1}$ represents all three non-OOP orientations, and $I_{\text{opt}}^{\bar{1}\bar{1}\bar{1}} = \frac{5}{9} I_{\text{max}}$.

In our experiment, we use a liquid crystal polarization rotator (Thorlabs LCR1-532) to rotate the linear polarization of the excitation laser, which is set to a power below NV saturation, while collecting NV fluorescence without polarization discrimination. Fig. 4.3a shows data for three representative NVs oriented along the three non-OOP-oriented NV axes in our (111) scanning probes, where we observe distinct minima of $I^{\bar{1}\bar{1}\bar{1}}(\varphi_e)$, reaching $\sim 0.23 I_0^{\bar{1}\bar{1}\bar{1}}$ at $\varphi_e = \varphi_{\text{NV}}$ for each dataset. As expected, φ_{NV} is shifted by $\pm 120^\circ$ between the three cases due to the three-fold symmetry of the diamond lattice viewed along the [111] direction. The minima of $I^{\bar{1}\bar{1}\bar{1}}(\varphi_e)$ exceed the expected value of $0.11 I_0^{\bar{1}\bar{1}\bar{1}}$, which we assign to background fluorescence and the onset of optical saturation.

One the other hand, the low polarization angle dependence of the OOP-oriented NVs (Fig. 4.3 b) allows for a reduced experimental complexity without polarization rotation, while offering a higher count rate and better magnetic field sensitivity. Additionally, lower excitation powers compared to other NV orientations can be used, allowing for a smaller thermal load on the sample, which is particularly important

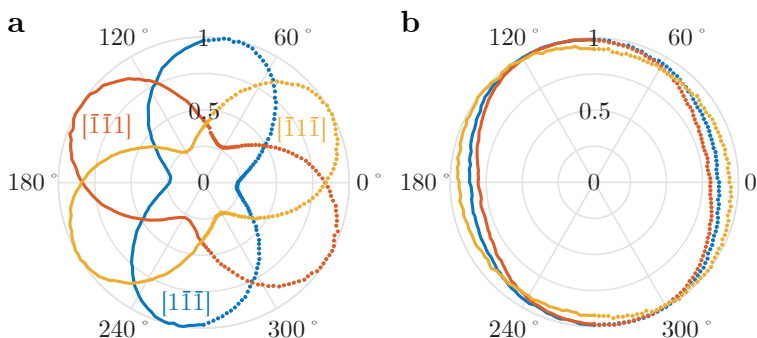


Figure 4.3.: Polarization angle dependent excitation. (a) Dependence of the measured NV count rate on the excitation polarization angle φ_e , for the three NV center orientations away from the out-of-plane (OOP) direction in a (111)-oriented scanning probe. The strong dependence on the polarization angle allows for identification of the NV orientations. (b) Same as in (a) for three OOP-oriented NV centers, all of which show only a weak dependence on polarization angle. In both graphs, points represent experimentally measured data, while lines correspond to the same data shifted by 180° . For each dataset, the count rates are normalized to their maximal value.

in cryogenic experiments. The remaining polarization dependence we attribute to mechanisms which break the cylindrical symmetry of the examined structures, such as off-center positioning of the NV centers in the pillar [67, 75], asymmetric pillar shapes, and transverse strain experienced by the NV [76].

4.2.3. Out-of-Plane NV Magnetometry

Finally, we conduct experiments to demonstrate the practical benefits of OOP-oriented NV centers by using one of our (111) scanning probes with a [111]-oriented NV center for nanoscale magnetic imaging. For this, we map magnetic stray fields emerging from a thin magnetic film (Ta/CoFeB(1 nm)/MgO) with OOP magnetization, as commonly employed for experiments in spintronics and skyrmionics [77, 78]. The sample geometry consists of an arrangement of $1\ \mu\text{m}$ wide stripes to generate a non-trivial stray field distribution.

A typical NV magnetometry image obtained over a “T-shaped” section of the CoFeB pattern is shown in Fig. 4.4a. The characteristic outcome of employing an OOP-oriented NV for this experiment is that the measured stray field shows qualitatively the same behavior at every edge of the magnetic film, irrespective of edge orientation. Specifically, B_{NV} shows a sharp sign-reversal with a zero-crossing and a near-perfect antisymmetric behavior along the magnetic film edge (Fig. 4.4b,c). This behavior is in contrast to magnetometry with non-OOP oriented scanning NV centers [11–13, 15], where the qualitative behavior of B_{NV} near sample edges depends on the orientation of the edge (see Fig. 4.1c, Fig. 3.7, Fig. 3.12). The quantitative data obtained with our tip can be fitted by an analytical function, from which the sample magnetization M and NV-to-sample distance z_{NV} can be extracted [79]. In the present case, where only the OOP component of the stray field is measured, the magnetic field takes the simple form

$$B_{\text{NV}}(x) = B_z(x) = -\frac{\mu_0 M}{2\pi} \frac{x}{x^2 + z_{\text{NV}}^2}, \quad (4.8)$$

where the x -coordinate represents the lateral displacement from the magnet edge, μ_0 the vacuum permeability and M the two-dimensional sample magnetization. A fit to the linecuts in Fig. 4.4b,c yields $M = 1.1 \pm 0.1\ \text{mA}$ and $z_{\text{NV}} = 81 \pm 17\ \text{nm}$, $78 \pm 2\ \text{nm}$, and $55 \pm 2\ \text{nm}$ for the three edges observed. The difference in z_{NV} found between the different edges can be explained by geometrical factors originating from a small angular misalignment of a few degrees of the scanning tip with respect to the sample normal (Fig. 4.4d). Importantly, we find in all cases that $z_{\text{NV}} < 100\ \text{nm}$, demonstrating the excellent spatial resolution of our (111)-oriented diamond probes in NV magnetometry.

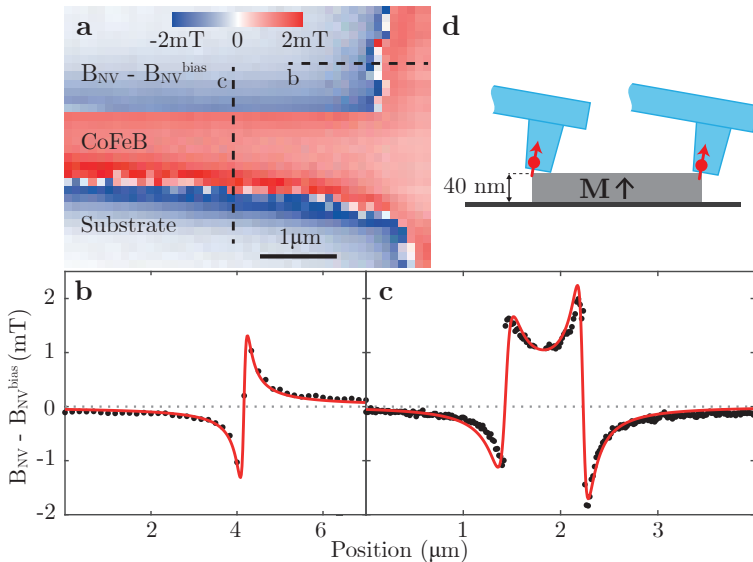


Figure 4.4.: Out-of-plane magnetometry on a thin magnetic layer. (a) Two-dimensional map of B_{NV} obtained with an OOP-oriented NV center on a patterned, 1 nm thin CoFeB film. (b, c) Independently measured line cuts of B_{NV} along the lines indicated in (a). The red lines are analytical fits to the data (see text), which allow for a quantitative determination of M and z_{NV} . In contrast to other NV orientations, B_{NV} shows the same antisymmetric behavior across each sample edge, irrespective of the edge orientation. (d) Illustration of the tilt-induced variation of z_{NV} between adjacent edges, responsible for the unequal maxima of B_{NV} observed in (c).

4.3. Summary and Outlook

In this chapter, we discussed the benefits of (111)-oriented diamond scanning probes with OOP-oriented NV centers and demonstrated their first experimental realization. The motivation to use such OOP NVs for magnetometry is manifold, ranging from improved photonic properties and enhanced signal-to-noise ratio to ease of data interpretation and usability in large OOP bias magnetic fields.

Following a fabrication process that is analogous to the one of (100)-oriented scanning probes, we characterized the (111)-oriented tips using ODMR, where the OOP-oriented NV centers could be identified unambiguously. Furthermore, we discussed the photonic advantages of OOP-oriented NVs in terms of collection efficiency [67, 69], magnetic field sensitivity and polarization independent excitation efficiency, while allowing for a reduced experimental complexity and lower excitation powers. Using polarization angle dependent fluorescence collection under linearly polarized excitation, we demonstrated the identification of all four possible NV orientations. Lastly, an NV magnetometry scan using an OOP NV center yielded an easily interpretable magnetic field map of the sample and confirmed the expected antisymmetric shape across the edges of the magnetic film.

Future developments of our (111)-oriented diamond probes could include an im-

proved yield of scanning probes with single $[111]$ -oriented NVs by using deterministic alignment of the nanopillars onto the corresponding NV centers in the fabrication process. While this approach would be already useful in conventional (100) -oriented tips, it would even be more relevant in (111) -oriented scanning probes where only one of the four NV orientations is usable for OOP magnetometry. Moreover, improvements of the parabolic nanopillar shape and its waveguiding properties [74] could further enhance the optical excitation and readout of OOP-oriented NV centers, yielding higher count rates, lower NV saturation powers, and better magnetic field sensitivities.

5. Oxide Interface LAO/STO

In this chapter, we discuss the extraordinary properties of the oxide interface LAO/STO and present our results concerning our studies of electronic transport, superconductivity, inhomogeneous current flow, and magnetism which we addressed using scanning NV magnetometry on this material. Since the discovery of conductivity at the interface of the two intrinsically insulating oxides SrTiO₃ (STO) and LaAlO₃ (LAO) in 2004 [80], the exploration of oxide interfaces has been a prominent field of research in mesoscopic condensed-matter physics. Further interest was sparked in 2007 when superconductivity was demonstrated at the LAO/STO interface at temperatures below 200 mK [16, 81]. Additionally, the research on LAO/STO has yielded discoveries such as inhomogeneous current flow along crystal axes [82, 83] and the exceptional co-existence of magnetism and superconductivity [5]. In the following, we provide a background of the previous research on LAO/STO in the mentioned directions, which we will use as a reference to reflect the results obtained by transport measurements and NV magnetometry on this material.

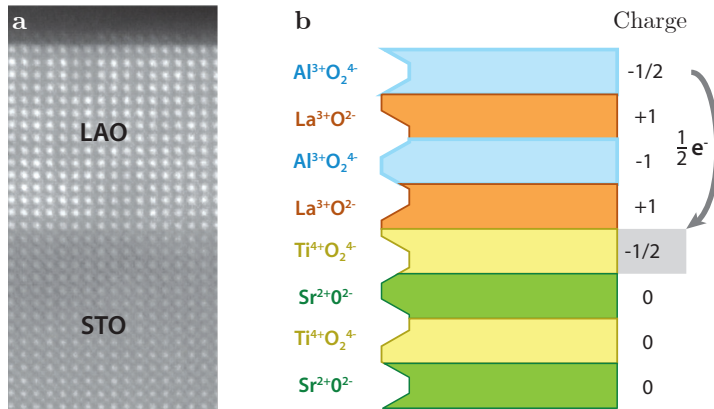


Figure 5.1.: Structure of the LAO/STO oxide interface. (a) Cross-section of a crystalline LAO/STO sample imaged by a scanning transmission electron microscope (STEM), where the bright dots represent the massive La and Sr atoms. The conductive oxide interface is formed between the STO substrate and, in this case, the 15 LAO layers. Figure adapted from [16]. (b) Schematic representation of two LAO and STO layers with two sublayers each. Each LAO layer is composed of a $\text{La}^{3+}\text{O}^{2-}$ sublayer carrying an elementary charge e per unit cell, and an $\text{Al}^{3+}\text{O}_2^{4-}$ sublayer with a charge of $-e$ per unit cell. Each STO layer is composed of a $\text{Sr}^{2+}\text{O}^{2-}$ sublayer and an $\text{Ti}^{4+}\text{O}_2^{4-}$ sublayer, both being charge-neutral. A charge of 0.5 electrons per unit cell is transferred from the surface to the interface due to minimization of the electrostatic potential energy. Figure adapted from [84].

5.1. Theoretical Background

A typical LAO/STO sample consists of a (001)-oriented SrTiO₃ substrate with alternating SrO and TiO₂ sublayers and a few LaAlO₃ layers consisting of LaO and AlO₂ sublayers. The interface between the two is formed by a TiO₂ and a LaO sublayer, and the sample surface consists of an AlO₂ sublayer (Fig. 5.1). It has been shown that for at least four LAO layers [85], the oxide interface becomes conductive and exhibits a sheet resistance $\sigma_S = 10 - 30 \text{ k}\Omega/\square$ at room temperature and $\sim 500 \Omega/\square$ at 10 K [86]. The emergence of conductivity is owed to the formation of a mobile two-dimensional electron gas at the oxide interface due to an electron transfer from the LaO surface sublayer to the TiO₂ sublayer at the interface.

The transfer of 0.5 electrons per unit cell (Fig. 5.1b) balances the charge distribution and reduces the electrostatic potential energy [87]. The transferred electrons show a high mobility due to a weak confining potential in the TiO₂ interface sublayer and a low sheet resistance [80]. The electron transfer to the interface requires a certain amount of energy, which is only compensated by the electrostatic energy if at least four LAO layers are present, leading to the LAO thickness threshold for the interface conductivity.

Moreover, the occurrence of superconductivity was discovered in the LAO/STO interface, where the two-dimensional electron gas condenses into a superconducting phase below a critical temperature $T_c \sim 200 \text{ mK}$ [16, 86]. Fig. 5.2a shows a typical V vs. I curve of a LAO/STO sample as a function of applied current at different temperatures below 300 mK [16]. The corresponding critical current densities J_c depend on

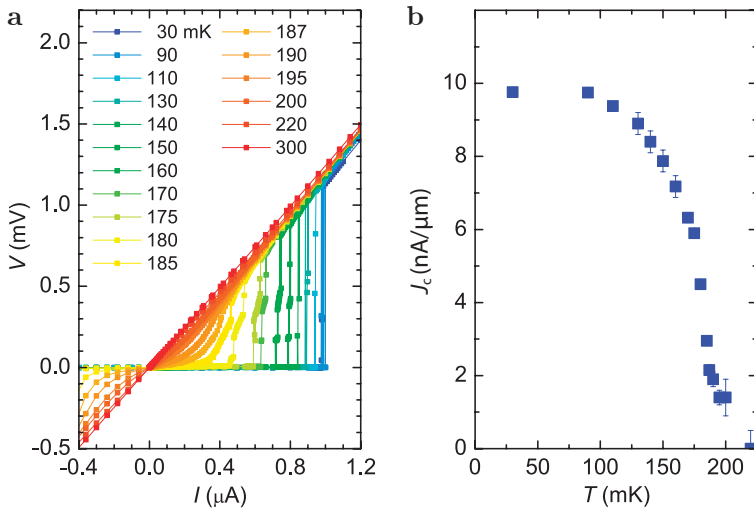


Figure 5.2.: Superconductivity and critical temperature in LAO/STO. (a) Voltage as a function of current through a $100 \mu\text{m}$ wide channel at temperatures below 300 mK in a sample with 8 LAO layers. The vertical jumps indicate the transition between superconductivity and normal conductivity. (b) Corresponding critical current density vs. temperature. Figures adapted from [16].

temperature and approach $10 \text{ nA}/\mu\text{m}$ (Fig. 5.2b). Note that this current density is small for magnetometry purposes, with magnetic stray fields only in the order of few nT. Furthermore, the application of a back-gate voltage allows to tune both normal conductivity and superconductivity in LAO/STO. Since positive back-gate potentials draw additional electrons from the surface to the interface, they can decrease the sheet resistance by almost two orders of magnitude, allowing for tuning of T_c from zero to $\sim 300 \text{ mK}$ [81]. Our own electric transport measurements in LAO/STO are presented in Sect. 5.2.2.

Concerning non-superconducting currents, significant spatial inhomogeneities in current density have been observed in LAO/STO [82, 83]. The magnetic field created by inhomogeneous currents was measured using a SQUID scanning magnetometer, and the obtained field map $B_z(x, y)$ contains information on the underlying current distribution in the oxide interface (Fig. 5.3). It was found that the current flows in narrow paths and preferably along the LAO/STO crystal axes, rather than directly with the applied electric field as it would be the case in a homogeneous metallic layer. We present our own magnetometry experiments on inhomogeneous current distributions in Sect. 5.2.3.

Furthermore, prominent ferromagnetic signatures in the LAO/STO interface have been observed [5] and demonstrated to be stable over a large range of back-gate voltage

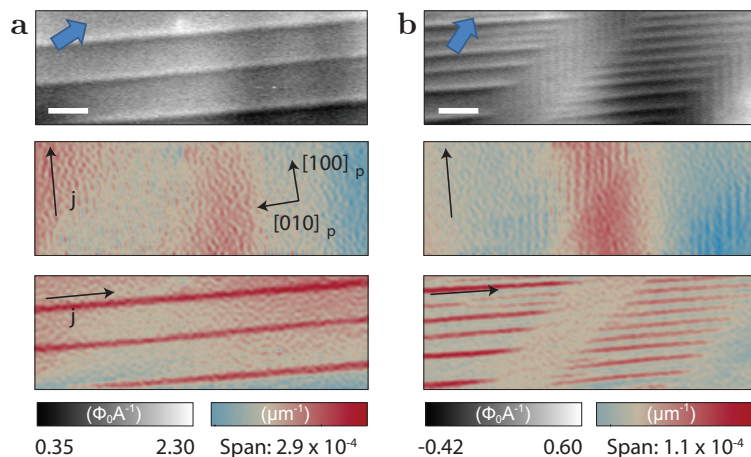


Figure 5.3.: Inhomogeneous flow of non-superconducting current in LAO/STO. (a) Measured magnetic flux and corresponding current density in an unpatterned LAO/STO sample with 5 layers of LAO, at 4 K. Top: Magnetic flux normalized by applied current, measured by an a.c. SQUID. The blue arrow denotes the direction of the applied electric field. Middle, bottom: back-propagated current density along the [100] and [010] crystal axis, respectively. The current density is normalized by the applied current. The current flows in narrow paths primarily along the crystal axes, particularly along the [010] direction. (b) Same measurement in another position of the sample. Note that the indicated current density span is only relative, since a homogeneous offset in current density is not displayed in the magnetic stray field. The scale bar is $30 \mu\text{m}$. Figures adapted from [83].

[27]. Intriguingly, these magnetic features persisted even below the superconducting critical temperature, which may constitute a rare case of coexistence of magnetism and superconductivity. This is especially surprising since superconductivity with its Meissner effect is generally not compatible with magnetism, and since strong magnetic fields above the critical field quench superconductivity. However, a multitude of dipole-like magnetic features of varying strength and preferably in-plane orientation were detected using SQUID magnetometry (Fig. 5.4a) [27]. The observed magnetic moments were in the order of $10^7 \mu_B$ and therefore provided large enough signal to be imaged at a high signal-to-noise ratio (Fig. 5.4b). Considering the magnetic flux of $10 \text{ m}\Phi_0$ and the loop area of $7 \mu\text{m}^2$ in the employed SQUID, the average magnetic field over the SQUID loop can be estimated to $3 \mu\text{T}$. Due to the rapid fall-off of the dipole field $\propto 1/r^3$, these magnetic moments could be detected much more easily by a technique that allows measuring the stray magnetic field closer to the sample, NV magnetometry being an ideal candidate. At a typical NV-sample distance of 70 nm, the in-plane dipoles would produce magnetic fields in the order of 30 mT, exceeding the NV sensitivity by more than four orders of magnitude. Another estimate is more conservative and assumes a homogeneous distribution of the magnetic moment over an area the size of the SQUID loop, yielding a density of $1.4 \mu_B/\text{nm}$. The resulting fields are in the order of $20 \mu\text{T}$ for in-plane magnetic moments, still one order of magnitude above the NV sensitivity (Sect. 5.2.4).

Furthermore, ferromagnetism in LAO/STO was imaged at room temperature using magnetic force microscopy (MFM) [88]. However, the magnetic signatures emerged only after electron depletion of the interface using negative back-gate voltages. The magnetic patterns appeared randomly and were not correlated upon cycling of the back-gate voltage. Additionally, in-plane magnetism of LAO/STO was demonstrated

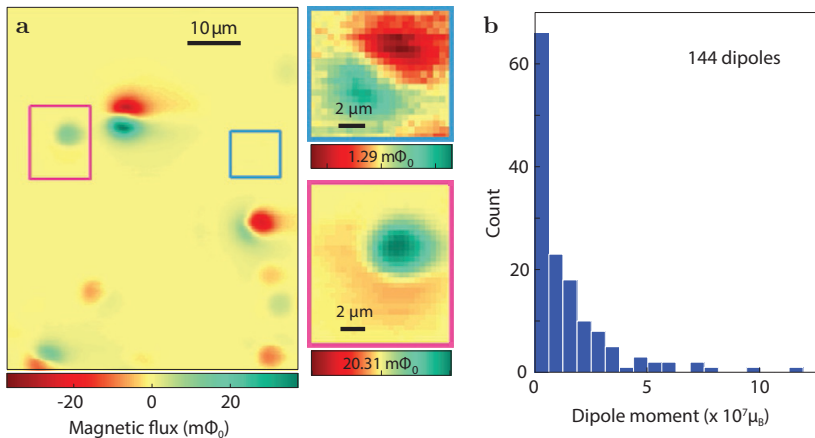


Figure 5.4.: Observation of magnetic moments in LAO/STO. (a) Magnetic flux measured using a SQUID. Several prominent dipolar features of varying magnitude are detected in the scan area. Individual dipoles are shown in the insets. (b) Histogram of the strength of the observed magnetic dipoles in the order of $10^7 \mu_B$. Figures adapted from [5].

by magnetic torque magnetometry over a large temperature range, from the superconducting regime to 200 K [26].

However, the ferromagnetism in LAO/STO was proposed to be non-intrinsic and originate from oxygen vacancy defects in the interfacial TiO_2 sublayer or the LAO layers [89]. Therefore, the observed magnetic features in the oxide interface may depend on material quality, and may not be present in samples without oxygen vacancies. Overall, the LAO/STO interface holds many interesting physical properties which we will examine using low-temperature transport measurements and NV magnetometry.

5.2. Results

In this section, we discuss our results on the oxide interface LAO/STO. We examine three samples in terms of electronic transport, current distribution and intrinsic ferromagnetism. Using electronic transport measurements, we examine superconducting properties of our samples. In order to examine the current distribution and the intrinsic ferromagnetic properties we use our NV magnetometry technique. In the following, we present each measurement in detail.

5.2.1. Experimental Samples

The LAO/STO samples were fabricated in the group of Prof. J.-M. Triscone at the university of Geneva. The sample is fabricated starting with a single crystal STO substrate and using a positive photoresist to pre-structure the sample geometry (Fig. 5.5a). The areas which will not hold a functional oxide interface later are covered with 20 nm of amorphous STO. As a next step, LAO is deposited on the substrate by pulsed laser deposition (PLD), using a 246 nm laser with 10 ns pulses of 35 mJ energy applied at a repetition rate of 1 Hz. The growth is monitored by reflection high-energy electron diffraction (RHEED) and 8 to 10 layers of LAO are deposited for our samples. To ensure optimal mobility of the deposited LAO and the growth of a fully saturated oxide without oxygen vacancies, the temperature is held at 800°C at an oxygen pressure of 10^{-4} mbar [90]. As a result, a functional LAO/STO interface is formed on the single crystal STO in the sample structure, whereas a non-functional interface is formed beside the structure on the amorphous STO.

We obtain three samples, here referred to as sample A, B and C. Sample A with 10 LAO layers consists of LAO/STO bulk areas and channels of widths ranging from 10 μm to 300 μm . Four contacts each allow for 4-point measurements of the electrical resistance, which eliminate contributions from the background resistance of the contacts (Fig. 5.5a). The structure is then contacted using gold bonding wires of 30 μm diameter. Sample B contains 8 layers of LAO. It is used to test the quality of the material by measuring the resistance over a 3 μm wide and 150 μm long channel, as a function of temperature (Fig. 5.5b). The resistance of the two-dimensional electron gas shows a metal-like temperature dependence, and the small resistance of the narrow channel of 7 k Ω at 4 K indicates a low defect density of the fabricated device (Fig. 5.2a). Additionally, sample C is fabricated which contains a contacted back-gate, allowing for measurements as a function of back-gate voltage. Sample C is structured to a 200 μm wide and 500 μm long LAO/STO channel with 8 layers of LAO.

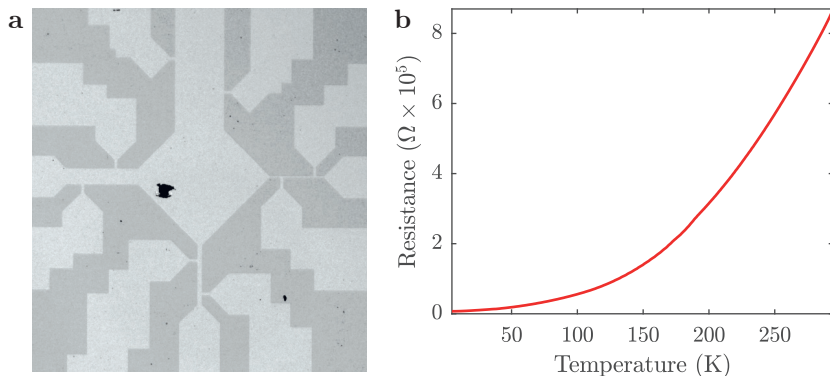


Figure 5.5.: Sample layout and temperature dependent resistance (a) Geometry of sample A with single crystal (bright) and amorphous LAO/STO (dark). The structure contains channels of $10 \mu\text{m}$ to $300 \mu\text{m}$ widths and $200 \mu\text{m}$ length. (b) Electrical resistance of sample B vs. temperature from room-temperature to liquid helium temperature of 4.2 K , measured over a $3 \mu\text{m}$ wide and $150 \mu\text{m}$ long channel.

5.2.2. Electronic Transport Measurements

A characteristic property of the oxide interface LAO/STO is its two-dimensional superconductivity below $T_c = 200 \text{ mK}$ and $J_c = 10 \text{ nA}/\mu\text{m}$ [16]. To test the superconducting properties of our sample and compare them to previous results, we mount the sample in our dilution refrigerator and measure the resistance as a function of various parameters, in either 2-point or 4-point measurement configuration. For the temperature dependence, we use a heater close to the sample and are thereby able to control the temperature between 25 mK and a few Kelvin. In a 2-point measurement over the $100 \mu\text{m}$ wide channel in sample A, we find a distinct resistance step of 150Ω at a sensor temperature of 550 mK , indicating a critical temperature T_c and superconductivity below it (Fig. 5.6a). To explain the discrepancy of the observed T_c with the one in literature $\sim 200 \text{ mK}$, we note that the temperature sensor and the heater are not located directly at the sample. A residual resistance of $2.8 \text{ k}\Omega$ in the 2-point measurement is reasonable, considering a bonding contact resistance of $1 \text{ k}\Omega$ each and additional resistances. Measuring the resistance as a function of current, we find a similar behavior with an increase of 200Ω at a critical current $I_c = 1.1 \mu\text{A}$ (Fig. 5.6b). This corresponds to a critical current density $J_c = 11 \text{ nA}/\mu\text{m}$ in the $100 \mu\text{m}$ channel, in accordance with the literature value of $10 \text{ nA}/\mu\text{m}$ [16]. Furthermore, an increase of the resistance is observed in sample A when applying an out-of-plane magnetic field which quenches superconductivity at the interface. The critical field is measured to be $B_c = 3 \text{ mT}$, with a resistance increase of 150Ω similar to the critical temperature and current. This value of B_c is below the value of 20 mT found in [91], which is possibly due to the use of a high back-gate voltage of 80 V in this work, which stabilized the superconducting state.

Lastly, we test the influence of the back-gate voltage on the electrical resistance over a $200 \mu\text{m}$ channel in sample C in a 4-point measurement, finding a near-linear decrease of electrical resistance with back-gate voltage from 500Ω at 0 V down to

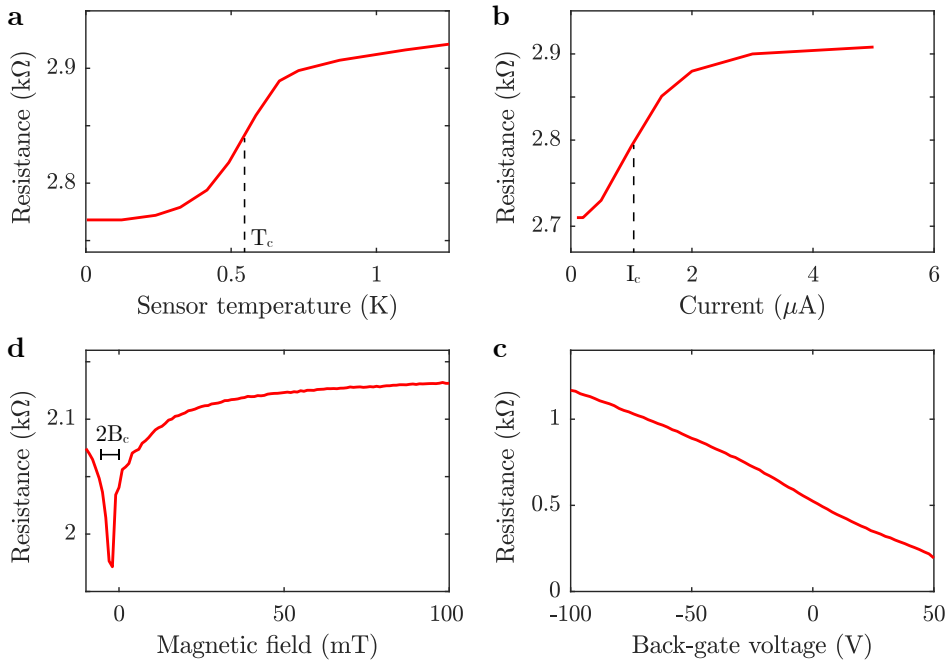


Figure 5.6.: Electrical resistance in the LAO/STO interface in samples A and C. (a) Resistance as a function of temperature with critical temperature $T_c = 550$ mK at $J = 50$ nA. Note that the temperature sensor and the heater are located in the sample stack, and that the measured temperature does not directly reflect the sample temperature. (b) Resistance as a function of current with a critical current $I_c = 1.1$ μA , corresponding to $J_c = 11$ nA/ μm , at $T \sim 50$ mK. (c) Resistance as a function of out-of-plane magnetic field with critical field $B_c = 3$ mT. Note that the shift of the minimum resistance to negative fields is caused by hysteresis when scanning from high to low fields. (a-c) are measured in a 2-point configuration over the 100 μm wide channel in sample A. (d) Resistance as a function of back-gate voltage at $T \sim 25$ mK and $J = 100$ nA, in a 4-point measurement over a 200 μm wide channel in sample C.

200 Ω at 50 V. This is consistent with the fact that the conductance in LAO/STO is given by electrons which are pulled from the LAO surface to the oxide interface by the positive back-gate potential. According to previous research [91], we would expect that the resistance drops to zero at a back-gate voltage ~ 20 V at 15 mK, where the interface electron density becomes large enough for superconductivity. However, despite the 4-point measurement configuration, we do not reach zero resistance at a back-gate voltage up to 50 V, implying that no complete superconductivity is reached over the examined channel.

An unexpected observation is made when the electrical resistance over a channel is measured while scanning the sample with respect to the laser focus at 4 K. The position of the laser focus is found to have a strong influence on the electrical resistance through the 10 $\mu\text{m} \times 200$ μm LAO/STO channel in sample A. Specifically, the

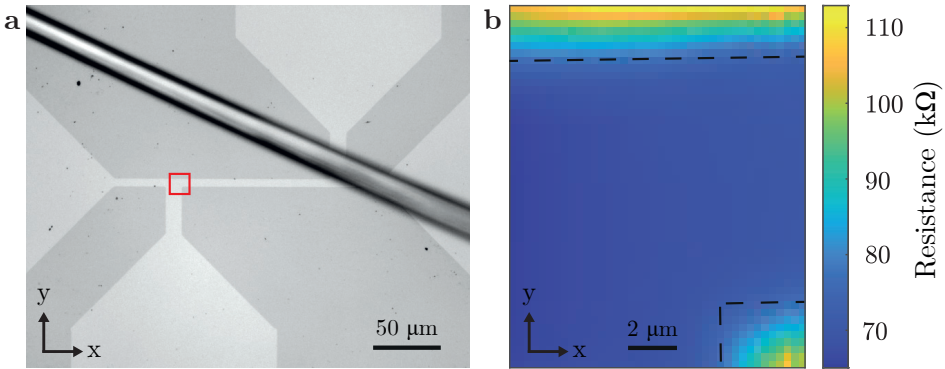


Figure 5.7.: Photoconductivity in LAO/STO sample A at 4 K. (a) A $10\ \mu\text{m}$ wide LAO/STO channel with a nearby metal wire for MW excitation used in later experiments (Sec. 5.2.3, 5.2.4). The highlighted area corresponds to the scanned area in (b). (b) Measured resistance during a two dimensional scan of the LAO/STO junction with respect to the laser focus position. The resistance decreases significantly when the laser is focused onto the LAO/STO channel.

resistance is reduced by almost a factor 2 when the laser is focused onto the channel as compared to laser excitation next to the channel (Fig. 5.7). The resistance decrease implies that the 532 nm laser light increases the carrier density by trapping electrons in the oxide interface, an effect that is described as persistent photoconductivity [92].

5.2.3. Magnetic Imaging of Currents

In order to measure the homogeneity of the current distribution in LAO/STO, we take advantage of the channels to confine the current within a suitable cross-section and examine the magnetic stray field generated by our currents. While superconductivity may be present locally in our sample even in the absence of zero global resistance, a current density $J_c = 10\ \text{nA}/\mu\text{m}$ allows only for stray fields in the order of nT. With our typical DC sensitivities $\sim 1\ \mu\text{T}/\sqrt{\text{Hz}}$, resolving such small fields would be extremely slow and not practicable. Also with other techniques, no superconducting currents in LAO/STO have been imaged as of now. However, ohmic currents in LAO/STO have been imaged previously and shown non-trivial inhomogeneities (see Fig. 5.3) [83].

In our sample, we apply a current of $50\ \mu\text{A}$ through the $10\ \mu\text{m}$ wide channel in sample A (see Fig. 5.7). We then measure the magnetic field B_{NV} in a line scan over the channel, finding a correlation of the topographical step onto the LAO/STO channel and the onset of magnetic signatures in the order of $10\ \mu\text{T}$ (Fig. 5.8a). Examining the magnetic stray field on the LAO/STO channel in two dimensions, we again find areas of varying magnetic field of the same order of magnitude (Fig. 5.8c). Applying reverse propagation to the magnetic field data, we obtain an image of the current density \mathbf{J} and find an inhomogeneous, narrow current flow in the oxide interface, which cannot be explained in terms of the channel geometry (Fig. 5.8d). The current density in the narrow channel is in the order of $15\ \mu\text{A}/\mu\text{m}$, compared to an expected average density of $5\ \mu\text{A}/\mu\text{m}$, and shows a sharp angle of 90° . This flow channel may be of

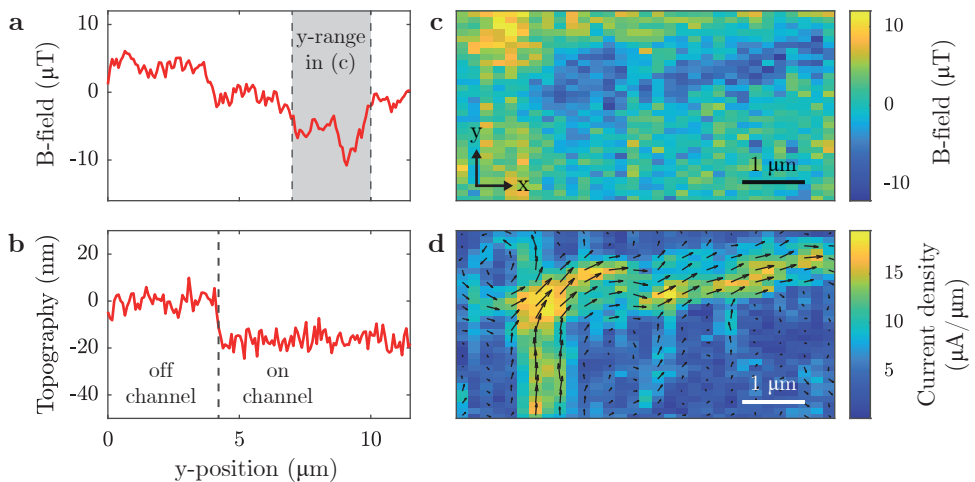


Figure 5.8.: Magnetic imaging of current flow in sample A at 4 K. (a) Measured magnetic field B_{NV} as a function of sample position across a $10 \mu\text{m}$ wide LAO/STO channel with $50 \mu\text{A}$ of current applied. The shaded area on the channel highlights the y -range covered in the 2D scan in (c). (b) Topographical data of the LAO/STO channel in the same measurement as (a). (c) Two-dimensional map of B_{NV} on the $10 \mu\text{m}$ LAO/STO channel as indicated in (a) applying the same current. (d) Corresponding back-propagated current density, using $z_{NV} = 50 \text{ nm}$, $\theta_{NV} = 54.7^\circ$ and $\varphi_{NV} = 90^\circ$.

the same nature as the ones in [83], and could therefore also be caused by structural grain boundaries in LAO/STO.

5.2.4. Magnetism in LAO/STO

Finally, we examine our LAO/STO sample in terms of intrinsic ferromagnetism as reported in [5]. Therefore, we conduct two-dimensional magnetometry scans on the sample, in both iso-B and full-B measurement mode. However, in three iso-B scans on a total area of $394 \mu\text{m}^2$ on sample A, we didn't find any signatures of magnetism (Fig. 5.9a). Taking into account ESR contrast, line width and measurement noise of our experiment, we can set an upper limit of $18 \mu\text{T}$ for the stray magnetic fields above the sample. This corresponds to a limit to the in-plane magnetic dipoles of $6.7 \times 10^3 \mu_B$, considering a typical NV-sample distance of 70 nm , μ_B being the Bohr magneton.

In order to detect weaker magnetic signals, we conduct 14 full-B scans on a total area of $2.2 \times 10^3 \mu\text{m}^2$ on sample A and C, recording an ESR spectrum in each point. Again, no magnetic textures are detected and the noise level in the measured field B_{NV} is $4 \mu\text{T}$, which allows only for in-plane magnetic dipoles $\lesssim 1.6 \times 10^3 \mu_B$, considering a 70 nm NV-dipole distance. A more conservative estimate takes into account that the magnetic moment may be distributed over an area as large as the SQUID loop in the

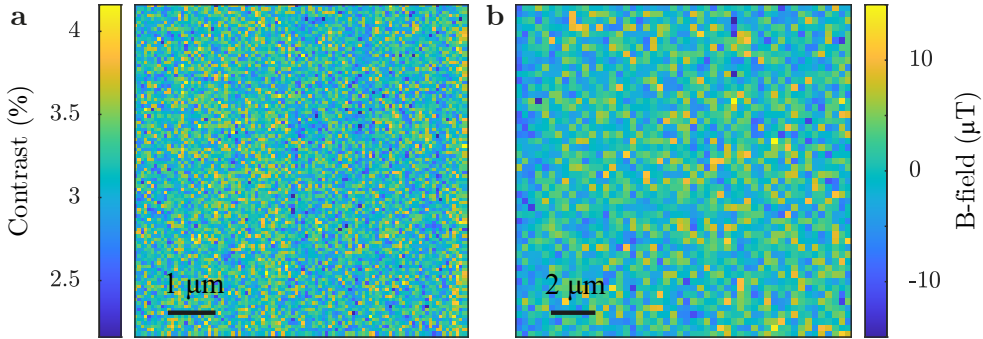


Figure 5.9.: Examining magnetism in LAO/STO at 4 K. **(a)** Representative iso-magnetic field scan in sample A at a bias field of 3 mT along the NV axis. No magnetic signatures are observed in the scan area of $49 \mu\text{m}^2$. With a full ESR contrast of 4.6%, line width of 7 MHz and a measured noise level of 0.33%, the resulting uncertainty in B_{NV} is $18 \mu\text{T}$. **(b)** Representative full-B scan on sample C at a bias field of 10 mT. No magnetic features are observed in the scan area of $225 \mu\text{m}^2$ at a noise level of $4 \mu\text{T}$.

previous measurement (see Fig. 5.4). In this case, the noise floor of $4 \mu\text{T}$ corresponds to an allowed dipole moment of $2.3 \times 10^6 \mu_B$.

Overall, after measuring in various positions on two LAO/STO samples and not finding any magnetic signatures, we can exclude magnetic moments $\gtrsim 1.6 \times 10^3 \mu_B$ in case of point-like magnetic dipoles, 4 orders of magnitude smaller than the magnetic moments $\sim 10^7 \mu_B$ reported in [5]. In case of distributed magnetic moments, we can still exclude magnetic dipoles four times smaller than in [5]. We attribute the absence of these magnetic dipoles to the high material quality of our samples, since the previously reported magnetic moments may be based on oxygen vacancy defects [89]. Note that we could measure the magnetic field at a significantly higher sensitivity if we wouldn't have an issue with progressive bleaching of the NV ESR contrast (see A.3).

5.3. Summary and Outlook

We presented our results of scanning NV magnetometry on three LAO/STO samples which were fabricated by the group of Prof. Triscone in Geneva. We characterized the transport properties at mK temperatures and found hints of superconductivity. Surprisingly, we observed a strong influence of the green laser position on the electrical resistance. In terms of magnetometry, we measured the magnetic field of an ohmic current sent through an LAO/STO stripe, and found an inhomogeneous current distribution. In contrast to previous research [5], we didn't find any ferromagnetic signatures in the oxide interface, which we attribute to the high quality of our sample.

In spite of the absence of strong magnetic moments as reported in [5], we cannot exclude weaker forms of magnetism in our LAO/STO samples which generate stray fields below $4 \mu\text{T}$ at the location of the NV. To that end, we could use out-of-plane oriented NVs and improved collection efficiencies due to an optimized nanopillar shape

to increase the magnetic field sensitivity. Additionally, improved diamond surface quality could yield a higher and more stable ESR contrast with narrower line widths. In that case, magnetic fields could be measured at lower noise levels, allowing for observation of weaker magnetic features which are possibly present even in high-quality samples.

Furthermore, more detailed 4-point transport measurements with a close-proximity temperature sensor could provide better insight into the superconducting properties of the samples. Making further use of our scanning confocal setup, we could examine the dependence of the LAO/STO sheet resistance on laser position in more detail, using different laser powers and channel widths. Additionally, the investigation of inhomogeneous current flow as a function of previous laser exposure position would be an insightful experiment, which fits the capabilities of our scanning probe setup well. Another possible experiment would be the investigation of the dependence of LAO/STO properties on scanning probe potential, using a conductive layer on the diamond cantilever [90]. Finally, the detection of weak magnetic fields generated by the low-density supercurrents could be realized using improved magnetic field sensitivity as in AC NV magnetometry, together with an improved experimental stability allowing for extra-long measurement times. This would allow for measuring nanoscale spatial variations of the superconducting density and yield novel insight into the nature of oxide interfaces.

6. T_1 Relaxation at mK Temperature

T_1 relaxation between $|m_s = 0\rangle$ and $|m_s = \pm 1\rangle$ of the NV center ground state spin is driven by magnetic noise at the corresponding transition frequencies. Our study of the T_1 relaxation is motivated by the transition of the short T_1 times in the order of seconds at 4 K [93] to the very long T_1 times in the order of hours at 100 mK [6]. Furthermore, the T_1 time as a function of bias magnetic field yields an insight into the magnetic noise spectrum due to sources in the environment of the NV, such as the prominent resonance with the nitrogen spin $\frac{1}{2}$ [93], or the more subtle resonance with hydrogen nuclear spins [62]. NV Relaxometry can also be applied with spatial resolution using a scanning probe, in which case spatial variations of the field noise level can be probed [94, 95]. Ultimately, $T_2 < 2T_1$ is the fundamental limit of the coherence time T_2 , which is a key figure of merit in fields like quantum computing [96] and quantum sensing [97]. It is therefore important to understand the mechanisms that limit the spin lifetime T_1 and how they scale with temperature. In this chapter, we demonstrate the increase of T_1 at low temperatures and discuss a combination of measurement sequences, allowing for extraction of different decay rates between the three ground state spin levels of the NV. Furthermore, we show that a correct description of our data requires time-dependent rates, which could be explainable by spin diffusion. Additionally, we present a detailed relaxation rate spectrum over bias magnetic field and find decreasing rates with bias field, indicating a decrease of the magnetic and electric noise level with frequency. Lastly, at mK temperatures we find indications of a non-negligible thermal spin polarization both at low and high magnetic fields.

6.1. Theoretical Background

The decay of a spin population, or longitudinal relaxation, happens over a time T_1 . Such T_1 relaxation is a process where the spin population relaxes into a thermal, mixed state due to its coupling to the environment. With the NV center ground state consisting of the $|m_s = 0\rangle$ and $|m_s = \pm 1\rangle$ sublevels, a total of six rates exist between the states in general, where the rates in opposite directions are related by the Boltzmann distribution (Fig. 6.1a). As a common simplification, however, the six rates can be reduced to the two rates Ω and γ , where Ω describes the four rates between $|m_s = 0\rangle$ and $|m_s = \pm 1\rangle$, and γ describes the two rates between $|m_s = 1\rangle$ and $|m_s = -1\rangle$ (Fig. 6.1b). The relaxation time T_1 in the NV center usually defines the decay of the $|m_s = 0\rangle$ population and is given by $T_1 = 1/(3\Omega + \gamma)$ [98].

The distinction between Ω and γ is useful since the corresponding transitions are intrinsically different. While the transition between $|m_s = 0\rangle$ and $|m_s = \pm 1\rangle$ is driven by fluctuating magnetic fields, the transition between $|m_s = -1\rangle$ and $|m_s = 1\rangle$ is driven by fluctuating electric fields or strain. Therefore, the relaxation rate Ω is given

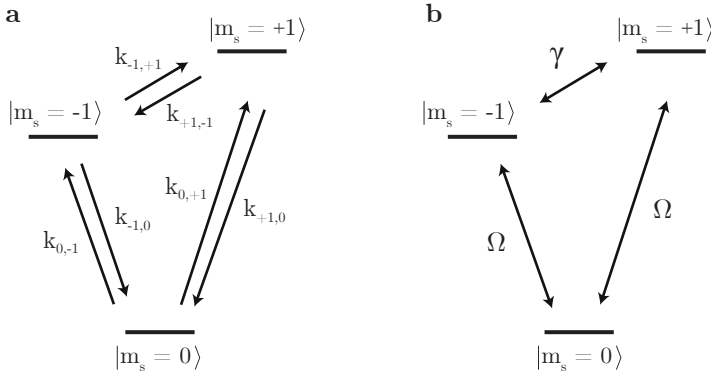


Figure 6.1.: Relaxation rates in the NV center ground state. (a) Full model: In principle, all six relaxation rates between the three states $|m_s = 0\rangle$ and $|m_s = \pm 1\rangle$ can be different, where the rates in opposite direction are related by the Boltzmann distribution. **(b)** Simplified model: Rate Ω between $|m_s = 0\rangle$ and $|m_s = \pm 1\rangle$, and rate γ between $|m_s = -1\rangle$ and $|m_s = +1\rangle$. This two-rate model takes into account the intrinsically different nature of the corresponding transitions.

by the magnetic noise at the transition frequency $\nu_{0,\pm 1}$, and γ is given by the electric noise at $\nu_{-1,1}$. In that way, measuring Ω and γ as a function of bias magnetic field can be used to deduce the magnetic and electric noise spectrum.

At room temperature, the lifetime of the NV spin is usually dominated by spin-lattice interactions. At low temperature, when the phonon contribution becomes negligible, the limiting factor of the NV spin lifetime is magnetic and electric field noise, as discussed previously. In high-density NV ensembles, however, a significant amount of magnetic noise is generated intrinsically, through dipole-dipole interactions with the surrounding spins [93]. The interacting spins can switch their states and perform so-called cross-relaxation, a process where a local equilibrium of the spin populations can be reached relatively quickly. Global relaxation, however, requires spin-lattice interaction or external noise sources, and may happen over much longer time scales at low temperatures [6].

As shown in [93], the relaxation rate $1/T_1$ is on the order of kHz at room temperature and rapidly decreases with lower temperatures due a decreased phonon population. At low temperature, however, the relaxation rate reaches a level given by the magnetic field noise and therefore the spin density in the diamond (Fig. 6.2a). In the particularly high-density NV ensemble sample "S2" which we will study subsequently, and where $[N] = 50$ ppm and $[NV] = 16$ ppm, the relaxation rate stays as high as 20 Hz at low temperature, which is several orders of magnitude higher than in other samples under comparable conditions.

A measurement of the relaxation rate as a function of bias magnetic field in sample S2 at 296 K reveals the existence of prominent noise peaks at particular fields (Fig. 6.2b) [93]. Three peaks of the relaxation rate are found, i.e. the resonance between all NV center orientations at 0 mT, the resonance with spins with $S = \frac{1}{2}$ such as nitrogen which occurs at 51 mT, and a resonance with the NVs of different

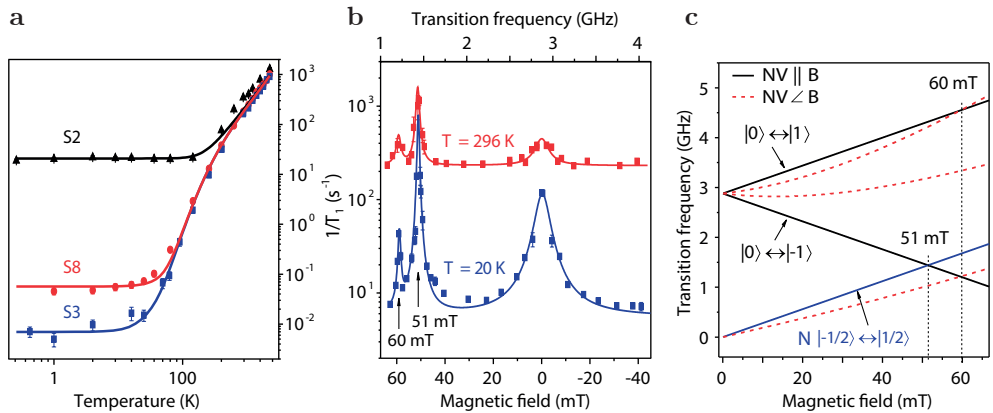


Figure 6.2.: Relaxation rate as a function of temperature and magnetic field. (a) Relaxation rates $1/T_1$ as a function of temperature. The three samples S2, S8 and S3 have decreasing nitrogen and NV density, correlating with the relaxation rate at low temperature. Sample S2 with $[N] = 50$ ppm and $[NV] = 16$ ppm will be used in the experiments in Sec. 6.2. (b) Relaxation rate $1/T_1$ in sample S2 as a function of bias magnetic field aligned with one NV orientation, at room temperature and at 20 K. The three peaks indicate the resonances with other NV orientations and with nitrogen spins with $S = \frac{1}{2}$. (c) Frequency of the $|m_s = 0\rangle$ to $|m_s = \pm 1\rangle$ transitions as a function of bias magnetic field, for NVs aligned with the magnetic field (black) and oriented at an angle of 109° (red dashed) to the the field. The transition frequency of the electron spins $S = \frac{1}{2}$ of nitrogen defects between the $|m_s = \pm \frac{1}{2}\rangle$ states is shown on blue. The resulting spin resonances between different NV orientations occur at 0 mT and 60 mT, and the resonance with spin $S = \frac{1}{2}$ occurs at 51 mK. Figures adapted from [93].

orientations at 60 mT (Fig. 6.2c). At 20 K, these peaks are even more prominent, which indicates that the corresponding relaxation mechanisms show a much weaker temperature dependence than direct spin-lattice relaxation.

Furthermore, T_1 relaxation in NV centers has been studied at temperatures down to 50 mK. Since the zero-field splitting $D_0 = 2.87$ GHz corresponds to a temperature of $T = hD_0/k_B = 137$ mK, with h the Planck constant and k_B the Boltzmann constant, the Boltzmann distribution between the spin states becomes an important factor in this temperature range. Fig. 6.3 shows NV spin relaxation curves obtained at temperatures between 50 mK and 250 mK in a sample with $[N] \leq 200$ ppm and $[NV] = 40$ ppm, where the $|m_s = 0\rangle$ population reaches up to 88% [6]. On the other hand, extremely long T_1 times up to 8 hours were observed, which were limited by the phononic vacuum modes. In contrast, the data from [93] in Fig. 6.2a shows a much shorter T_1 time, and a plateau down to 5 K, with no indication in data or model that T_1 would increase further at lower temperatures. Since also in [6] a similarly high-density NV ensemble was used, it is not obvious what causes the gap between the measurements at 4 K and at mK.

On the one side, this gap could hint towards fundamentally different relaxation

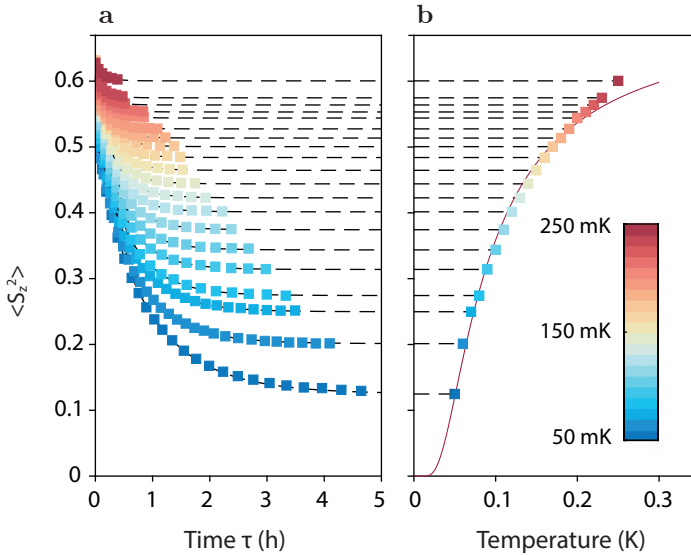


Figure 6.3.: Relaxation at mK temperature and shift of equilibrium population. (a) Measurement of $\langle S_z^2 \rangle$, as a function of waiting time τ in a sample with $[N] \leq 200$ ppm and $[NV] = 40$ ppm, at temperatures between 50 mK and 250 mK without external magnetic field. The $|m_s = 0\rangle$ populations and T_1 times both increase with decreasing temperatures. (b) The corresponding equilibrium population after relaxation fits to the Boltzmann distribution (red line). Figures adapted from [6].

mechanisms at the two temperature regimes or indicate large differences between the samples or experiments. On the other side, a possible cause is the different measurement method: While Jarmola et al. [93] used a confocal microscope to locally address the NVs, comparable to our approach, Astner et al. [6] read out the NVs by coupling to a cavity, yielding a global measurement over all NVs in the diamond. With this motivation, we will report on our own T_1 relaxation measurements at 4 K and 100 mK (Sec. 6.2), using the same high-density sample "S2" [93].

6.2. Results

In order to measure the longitudinal T_1 relaxation of NV spins, the spins are initialized into $|m_s = 0\rangle$ or $|m_s = \pm 1\rangle$ and the remaining spin population is measured after a waiting time τ . As an experimental realization, we use a non-resonant green laser to initialize the NV center into $|m_s = 0\rangle$, and can optionally swap the initialized state to either of the $|m_s = \pm 1\rangle$ states using a resonant MW π pulse (Fig. 6.4a). The spin state readout is also done by the green laser, where the population in $|m_s = 0\rangle$ contributes to a higher count rate. Analogously, a population swap using a π pulse at the end of the sequence maps $|m_s = \pm 1\rangle$ onto $|m_s = 0\rangle$ and therefore enables readout of either of the $|m_s = \pm 1\rangle$ populations. Fig. 6.4b shows the decay of the spin populations $P_{0,0}(\tau)$ and $P_{1,0}(\tau)$, with the subscript numbers corresponding to initial and final spin state,

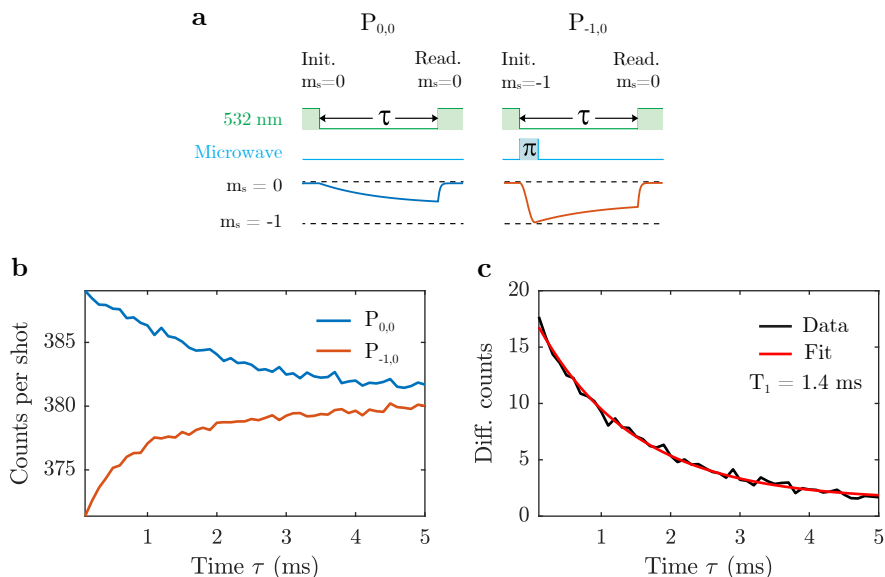


Figure 6.4.: T_1 relaxation measurement sequence and data at room temperature. (a) Measurement sequences for $P_{0,0}(\tau)$ and $P_{-1,0}(\tau)$, which denote the $|m_s = 0\rangle$ populations after initializing in $|m_s = 0\rangle$ and $|m_s = -1\rangle$, respectively. A green 532 nm laser is used to polarize the NV centers into $|m_s = 0\rangle$, and again read out the $m_s = 0$ population after a waiting time τ . A MW π pulse can transfer the initial population to $|m_s = \pm 1\rangle$. The population decay of the initial $|m_s = 0\rangle$ (blue) and $|m_s = -1\rangle$ (red) is illustrated. Figure adapted from [93]. (b) T_1 relaxation at room temperature and $B = 0$ in the high-density ensemble S2 that was also used in [93]. The measured count rate as a function of waiting time τ corresponds to the $|m_s = 0\rangle$ population. $P_{0,0}(\tau)$ and $P_{1,0}(\tau)$ denote the $|m_s = 0\rangle$ population after initializing in $|m_s = 0\rangle$ and $|m_s = 1\rangle$, respectively. Note that the $|m_s = 0\rangle$ population decays to $\frac{1}{3}$, however, in this measurement an experimental brightness drift over τ shifted this to higher values. (c) Population difference $P_{0,0}(\tau) - P_{1,0}(\tau)$ that yields an exponential fit with time constant $T_1 = 1.4 \pm 0.2$ ms. Note that an offset of 1.4 ± 0.5 allowed for a better fit.

in the same high-density sample "S2" used to acquire the data shown in Fig. 6.2 [93], at $B = 0$ and room temperature. In both cases, the population exponentially approaches equilibrium as $P_{0,0}(\tau) - P_{1,0}(\tau) \propto e^{-t/T_1}$, over a relaxation time constant T_1 . A fit yields 1.4 ± 0.2 ms (Fig. 6.4c). While this value for T_1 is shorter than the usual few milliseconds at room temperature [22], the result is consistent with the findings reported in [93]. The increased decay rate we find can be attributed to the high intrinsic noise level in the high-density ensemble, especially at zero magnetic field where all NV orientations are mutually in resonance.

In order to learn more about the internal fluctuating magnetic and electric fields in the sample, we cool the sample down to 4 K to eliminate the phonon-induced relaxation mechanisms which dominate at high temperatures. The much longer T_1 times

at low temperature make it necessary to optimize the pulse sequence for long waiting times. Therefore, we decrease the laser power to $3\ \mu\text{W}$ such that the bright high-density sample can be read out for a much longer time of 1 ms, without saturating the APD. Due to the low laser power, the initialization time was set to 50 ms. Improved MW π pulses were performed using adiabatic fast passage, where the MW frequency is swept over the ESR line, in this case over a range of 200 MHz in $32\ \mu\text{s}$.

To extract more information about the relaxation process, we measure all four possible relaxation processes occurring between $|m_s = 0\rangle$ and $|m_s = -1\rangle$, i.e. $P_{0,0}(\tau)$, $P_{0,-1}(\tau)$, $P_{-1,-1}(\tau)$ and $P_{-1,0}(\tau)$, at a bias magnetic field of 10 mT. As expected, we observe much longer relaxation times ~ 100 ms than at room temperature. However, rather than an overlay of the two curves $P_{0,0}(\tau)$ and $P_{-1,-1}(\tau)$ on upper side one side and of the two curves $P_{0,-1}(\tau)$ and $P_{-1,0}(\tau)$ on the lower side, as it would be the case for

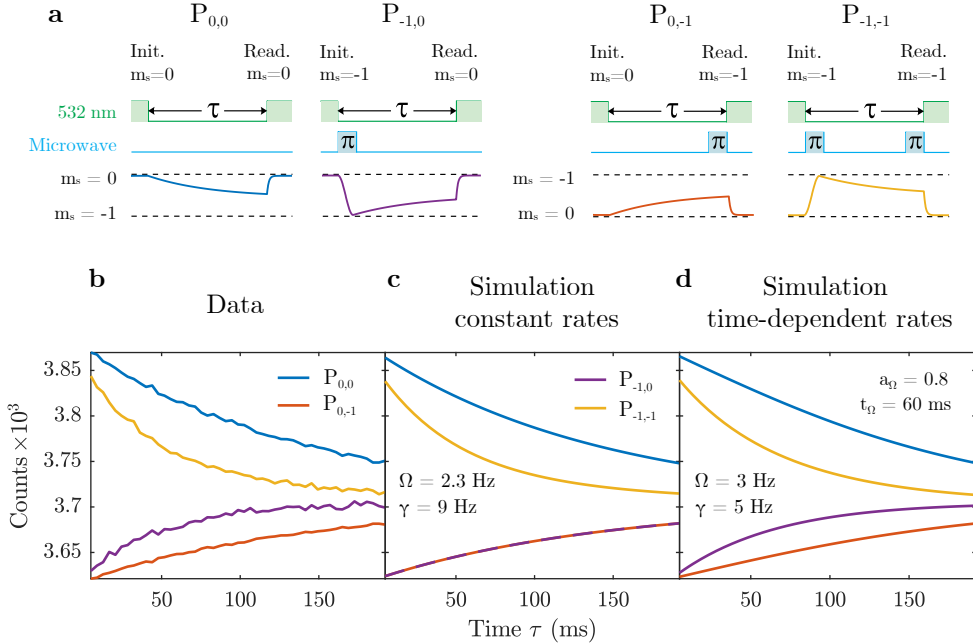


Figure 6.5.: T₁ relaxation at 4 K and time-dependent rates. (a) Measurement sequences for $P_{0,0}(\tau)$, $P_{-1,0}(\tau)$, $P_{0,-1}(\tau)$ and $P_{-1,-1}(\tau)$ (cf. Fig. 6.4a). Note that the color code used here also applies to (b)-(d). (b) All four measurement configurations configurations between $|m_s = 0\rangle$ and $|m_s = -1\rangle$ as a function of waiting time τ in sample "S2" at 10 mT are shown. State $|m_s = -1\rangle$ decays faster than $|m_s = 0\rangle$, possibly due to spin diffusion (see text). Note that an experimental drift of fluorescence rate with τ was compensated, using $P_{0,0} + 2P_{0,-1}$ as a constant reference. (c) Simulation using $\Omega = 2.3$ Hz and $\gamma = 7$ Hz reproduces $P_{-1,-1}$ but fails to reproduce $P_{-1,0}$. (d) Simulation using time-dependent, asymmetric rates instead of Ω (see text). Good reproduction of (a) using $\Omega = 3$ Hz and $\gamma = 5$ Hz, with a modification of Ω by $a_\Omega = 0.8$ and $t_\Omega = 60$ ms, as defined in the text. The simulations consider a π -pulse fidelity of 96%.

equal Ω and γ , we find four distinct relaxation curves (Fig. 6.5b). Considering unequal Ω and γ , an increased γ accelerates the decay from $|m_s = -1\rangle$ to $|m_s = 1\rangle$, which leads to a faster decay of $P_{-1,-1}$. However, it doesn't accelerate the equilibration of $P_{-1,0}$ and still causes the $P_{-1,0}$ and $P_{0,-1}$ curves to be identical (Fig. 6.5c). Overall, the faster equilibration of $P_{-1,0}$ than $P_{0,-1}$ can only be described by unequal rates $k_{0,-1} < k_{-1,0}$, which would only be plausible at very low temperatures where $kT < h\nu_{0,-1}$. This is, however, not given in our experiment at 4 K.

Nevertheless, a simple phenomenological description of the four distinct relaxation curves can be given using time-dependent rates $k_{0,\pm 1}(\tau) = \Omega / f(\tau)$ and $k_{\pm 1,0}(\tau) = \Omega \cdot f(\tau)$, with the rate factor $f(\tau) = 1 + a_\Omega e^{-\tau/t_\Omega}$ of amplitude a_Ω and time constant t_Ω . Indeed, we find good agreement with data using $\Omega = 3$ Hz ($T_1 = 80$ ms), $\gamma = 5$ Hz, $a_\Omega = 0.8$ and $t_\Omega = 60$ ms. With $k_{0,-1}(0) = 0.31 \cdot k_{-1,0}(0)$ and $\nu_{0,-1} = 2.6$ GHz, this would correspond to an initial spin bath temperature of 110 mK, which is 22 times smaller than the phonon temperature. However, this observation clearly violates the standard rate equation model which contains no considerations of time-dependent relaxation rates.

Looking for other explanations, we find the picture of spin diffusion due to dipole-dipole cross-relaxation within the NV spin ensemble, opening up room for further phenomena (Fig. 6.6a). Indeed, a simple estimation of the spin-spin interactions suggests relatively high diffusion rates and significant effects on the observable relaxation. Specifically, for sample S2 with an NV concentration of 16 ppm, we find a nearest-neighbor distance of 11 nm between resonant NVs ($\frac{1}{4}$ of all NVs with same orientation) and a resulting dipole-dipole interaction rate of 24 kHz. This yields a time of only 14 ms for the spins to diffuse over a distance of 210 nm, corresponding to the beam waist radius of the laser ($\lambda = 532$ nm, $\text{NA} = 0.82$). Therefore, this is the approximate time for the spin polarization created in the laser focus to diffuse into the surrounding bulk. Since this time is on the same order of magnitude as our observed relaxation times, spin diffusion may indeed play an important role in our measurements (see A.4).

To obtain a more accurate picture of spin diffusion, we perform a quantitative simulation of the diffusion of spin polarization, approximating the laser focus, with its high length to diameter aspect ratio of five, as a two-dimensional Gaussian. Using the same interaction parameters as above, we find that the diffusion process has a big influence already during the initialization pulse of 50 ms, where the diffusion causes much of the surrounding spins to be polarized as well (Fig. 6.6b). Subsequently, spin diffusion by itself causes a decay of the locally probed polarization (Fig. 6.6c) (see A.4).

Furthermore, the faster decay of the $|m_s = -1\rangle$ population compared to $|m_s = 0\rangle$ (see Fig. 6.5) might be explainable by spin diffusion, as attempted in the following. On the one hand, obviously, a faster diffusion rate of $|m_s = -1\rangle$ would accelerate the decay of the observed polarization (Fig. 6.6f). However, since the cross-relaxation between $|m_s = -1\rangle$ and $|m_s = +1\rangle$ is not dipole allowed, it is unlikely that such an increased rate would arise from coupling between $|m_s = -1\rangle$ and $|m_s = +1\rangle$. On the other hand, the fast $|m_s = -1\rangle$ relaxation might be caused by polarization diffusion into hypothetical, resonant dark spins, i.e. spins that couple weakly to the NV, but do not contribute to the readout signal and are not affected by the MW π -pulse. During the initialization pulse, the dark spins are polarized as well through the spin bath. The subsequent MW π -pulse for initialization into $|m_s = -1\rangle$, however, only flips the NV spins, while the dark spins stay in $|m_s = 0\rangle$ (Fig. 6.6d). During the waiting time

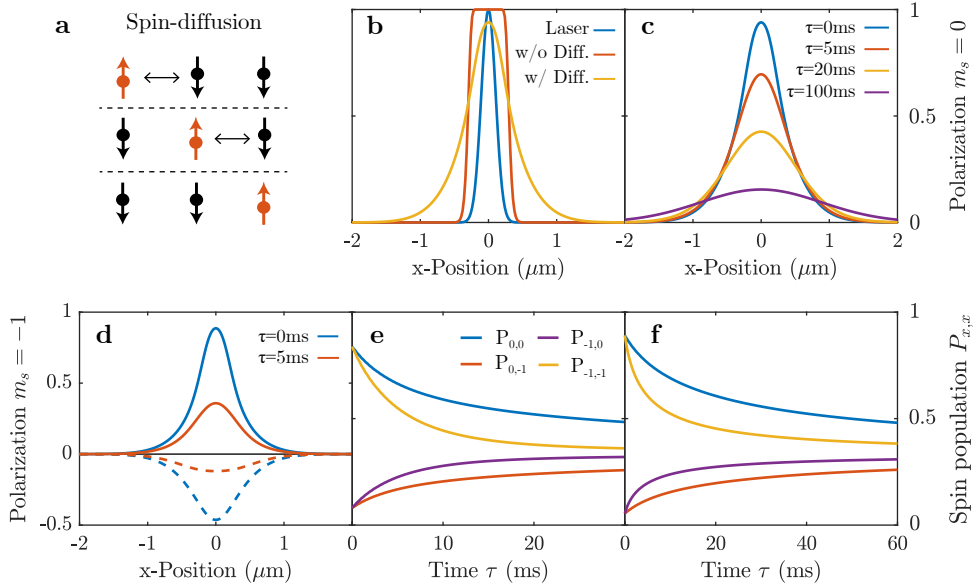


Figure 6.6.: Simulation of spin diffusion in diamond. (a) Schematic of cross-relaxation and diffusion of one particular spin (illustrated in red) due to dipole-dipole interactions. (b) Cross-section through laser profile and initialized spin polarization. The laser focus is approximated as a two-dimensional Gaussian (blue). Considering a spin-spin distance of 11 nm and interaction rate of 24 kHz (see text). Simulated $|m_s = 0\rangle$ polarization after an initialization pulse of 50 ms at an initialization rate of 1 kHz at the absence (red), and presence (yellow), of spin diffusion. (c) Diffusion and local decay of spin polarization after an initialization pulse of 50 ms at a rate of 1 kHz, after different waiting times τ . The polarization at the laser focus has decreased significantly after a few tens of ms. (d) Polarization after initialization in $|m_s = -1\rangle$. NV spins are transferred into $|m_s = -1\rangle$ by the MW π -pulse (continuous lines). Dark spins, not affected by the MW, stay in $|m_s = 0\rangle$ (dashed lines). The dark spins accelerate the decay of the NV $|m_s = -1\rangle$ population over waiting time τ . Same parameters as in (c), with an equal density of dark spins and NV spins and a coupling of 70 Hz. (e) Detected spin population $P_{x,x}$ as a function of waiting time τ , considering dark spins as described in (d). The population initialized in $|m_s = -1\rangle$ decays faster, showing similarities to the data in Fig. 6.5. (f) Spin population decay, considering a diffusion rate of $|m_s = -1\rangle$ four times higher than of $|m_s = 0\rangle$. Note that this calculation contains no dark spins. Same labels as in (e).

τ , the dark spins still couple back to the NV and thereby significantly accelerate their relaxation (Fig. 6.6e). Overall, we keep in mind that spin diffusion may play an important role in the observed spin relaxation. However, due to the uncertainty and complexity of the spin diffusion model we will continue to work with the previously described rate equation model.

To get insight into the magnetic field dependence of T_1 relaxation, we collect relaxation data between 0 mT and 200 mT, both at 4 K and 100 mK. As described above,

we measure in all four possible measurement configurations to extract Ω and γ , as described in the following: In the simple model with constant Ω and γ (see Fig. 6.1b), we find that the three quantities $P_{0,0}$, $P_{0,-1}$ and $P_{-1,0}$ decay with a single exponential $\propto e^{-3\Omega t}$, while $P_{-1,-1}$ decays with a double exponential $\propto \frac{1}{3}e^{-3\Omega t} + e^{-(2\gamma+\Omega)t}$, involving the rate γ . For the case of asymmetrical Ω with $k_{0,-1} \neq k_{-1,0}$ (cf. Fig. 6.5), we extract the rates $k_{0,-1}$, $k_{-1,0}$ and γ in the following way: We use $P_{0,0}$ and $P_{0,-1}$ to extract $k_{0,-1}$, then use $P_{-1,0}$ to extract $k_{-1,0}$ and finally use $P_{-1,-1}$ to extract γ . Rate Ω is defined as geometric mean of $k_{0,-1}$ and $k_{-1,0}$. Note that here we neglect any time-dependence of the rates.

The resulting magnetic field dependent rates at 4 K are displayed in Fig. 6.7, together with the rates measured at 20 K [93]. We find that our data reproduces the peaks at 0 mT due to cross-relaxation with other NV spins of all 4 orientations and at 51 mT due to cross-relaxation with nitrogen $\frac{1}{2}$ spins. We did not sample the peaks at 60 mT and at the GSLAC and these are thus not represented in our data. With the $|m_s = 0\rangle \leftrightarrow |m_s = -1\rangle$ and $|m_s = -1\rangle \leftrightarrow |m_s = 1\rangle$ transitions primarily driven by magnetic and electric fields, respectively, Ω and γ can give us an estimate of the magnetic and electric noise spectrum. Overall, except for the resonance around 51 mT, we find a trend towards smaller rates at higher magnetic fields, which indicates a decreasing noise level with higher frequency. Additionally, we find that Ω is larger

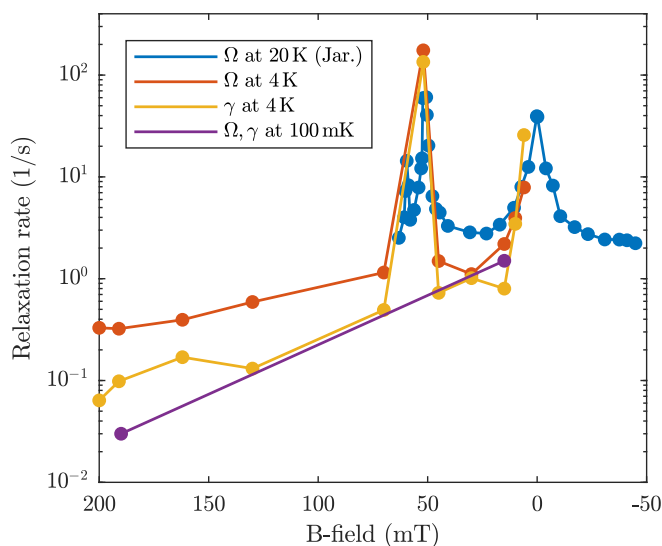


Figure 6.7.: Relaxation rates as a function of bias magnetic field. Rates Ω and γ measured between 0 mT and 200 mT, at 4 K and 100 mK, together with the data from [93] at 20 K (see Fig. 6.2b). The rates at 4 K are obtained from relaxation data similar to the one shown in Fig. 6.5a, and are extracted as described in the text. We can reproduce the resonances at 0 mT and 51 mT, and find decreasing rates at higher fields. Note that the data point of γ at 51 mT may be an artifact of our method. The two data points at 100 mK are obtained as described in Fig. 6.8.

than γ at magnetic fields > 10 mT. A possible explanation is that cross-relaxation with other NV spins is possible at any magnetic field since the resonance condition is always given with NVs of the same orientation, causing a weaker magnetic field dependence of Ω than of γ . At mK temperatures, as discussed in detail later, we find lower relaxation rates and a more pronounced difference at low and high magnetic field.

Entering the mK regime, the assumption of equal equilibrium populations breaks down due to the Boltzmann distribution. In this case, the ratio of higher to lower state population at temperature T is given by $e^{-\frac{h\nu}{k_B T}}$, where $h\nu$ is the energy difference between the states. This equilibrium population shift is represented by asymmetrical rates, therefore making use of the more complete model with all six rates between the three states (see Fig. 6.1b). At bias magnetic fields < 100 mT the equilibrium population $P_{0,eq}$ is larger than $P_{-1,eq}$. Therefore, the $|m_s = 0\rangle$ population is larger than the $|m_s = -1\rangle$ population, regardless of the initialized state. Inversely, at fields > 100 mT, $P_{-1,eq}$ is larger than $P_{0,eq}$ due to the GSLAC of $|m_s = -1\rangle$ and $|m_s = 0\rangle$. The result in both cases is that the two $P_{x,0}$ and the two $P_{x,-1}$ populations, x standing for 0 and -1, converge to two different equilibrium populations, with a larger difference at lower temperatures (Fig. 6.8a).

The data measured at 100 mK and bias fields of 15 mT is shown in Fig. 6.8a. While indicating unequal equilibrium populations, the four curves do not converge to only two population levels. Instead, for $\tau \rightarrow \infty$ we find a large remaining population difference between $P_{0,0}$ and $P_{0,-1}$, and a smaller difference between $P_{-1,0}$ and $P_{-1,-1}$.

A simulation of this data taken at 15 mT shows partial agreement with data when using $T = 75$ mK and $T_1 = 170$ ms ($\Omega = \gamma = 1.5$ Hz) (Fig. 6.8b). However, while the relaxation time appears to be on the right order of magnitude, in the simulation we see that $P_{0,0}$ and $P_{-1,0}$ converge to the same level, failing to reproduce the data. However, a much better description of the data is given considering two different temperatures $T_{m_s=0}$ and $T_{m_s=-1}$, for the two cases where initialization is performed into $|m_s = 0\rangle$ and $|m_s = -1\rangle$, allowing for different population equilibrations. Fig. 6.8c shows the simulation using again $T_1 = 170$ ms, but with $T_{m_s=0} = 75$ mK and $T_{m_s=-1} = 170$ mK, obtaining good qualitative agreement.

Furthermore, spin relaxation is measured beyond the GSLAC at 190 mT, again at 100 mK, where the equilibrium population is larger for $|m_s = -1\rangle$ which has lower energy (Fig. 6.8d). A corresponding simulation with $T = 230$ mK and $T_1 = 8$ s shows again partial agreement (Fig. 6.8e). We find better agreement with data using two temperatures $T_{m_s=0} = 500$ mK and $T_{m_s=-1} = 230$ mK, again with $T_1 = 8$ s. The higher spin bath temperature for $|m_s = 0\rangle$ than for $|m_s = -1\rangle$ initialization would be consistent with $|m_s = 0\rangle$ being the higher energy state. Overall, the measured T_1 time at 190 mT is 50 times longer than at 15 mT, implying that the relaxation at low field could be dominated by interactions with other spins.

Different temperatures at the two initialization states might be caused by spin diffusion: During the initialization pulse, $|m_s = 0\rangle$ polarization diffuses out of the laser focus into the spin bath. This corresponds to a cooling of the spin bath at bias magnetic fields below the GSLAC, and a heating of the spin bath at fields above the GSLAC. The MW π pulse to initialize into $|m_s = -1\rangle$, however, not only transfers the population of the probed NV spins, but also a part of the spins in the environment. Therefore, the π pulse heats (below GSLAC) or cools the spin bath (above GSLAC).

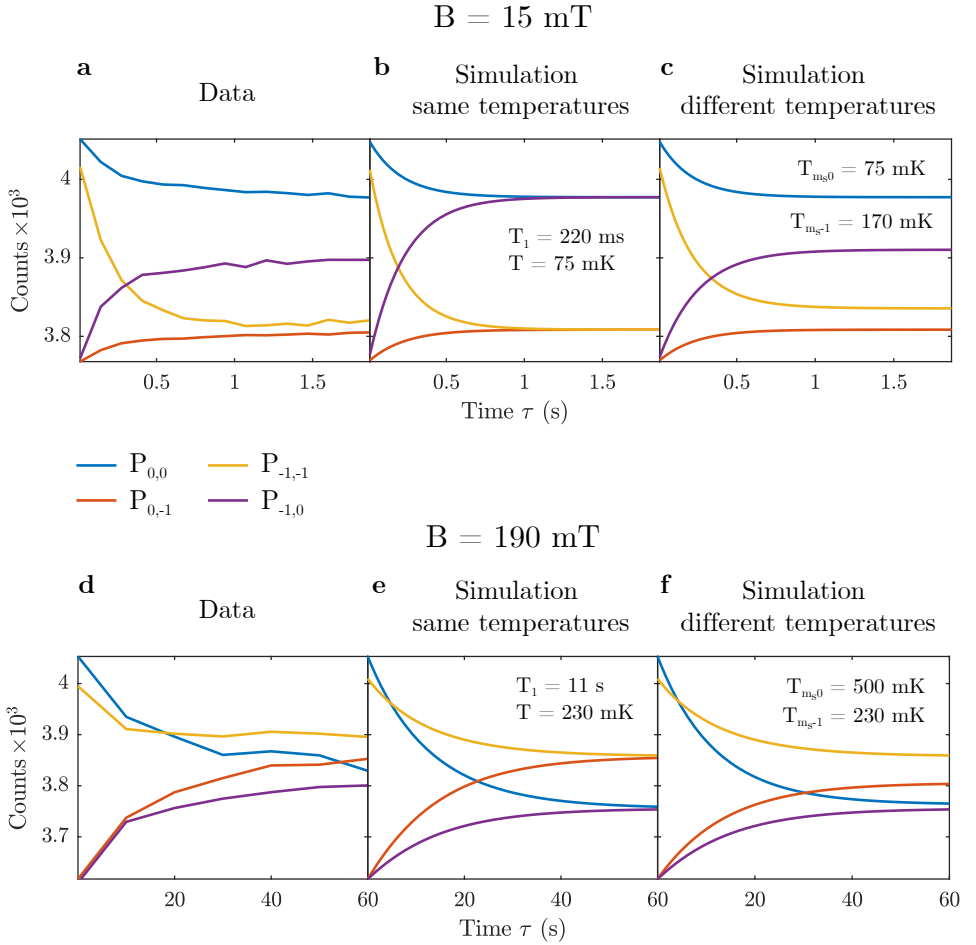


Figure 6.8.: T_1 relaxation at 100 mK and shifted equilibrium population. (a) Spin relaxation data between $|m_s = 0\rangle$ and $|m_s = -1\rangle$ measured at 15 mT. Note that an experimental drift of fluorescence rate with τ was compensated, using $P_{0,0} + 2P_{0,-1}$ as a constant reference. (b) Simulation using rate modifications according to the Boltzmann distribution between all three states, with $T_1 = 170 \text{ ms}$ ($\Omega = \gamma = 1.5 \text{ Hz}$) and $T = 75 \text{ mK}$. (c) Simulation using two different temperatures for the case where spin initialization is performed into $|m_s = 0\rangle$ and $|m_s = -1\rangle$, respectively. Good agreement with the data in (a) is found with $T_{m_s=0} = 75 \text{ mK}$ (initialization into $|m_s = 0\rangle$), and $T_{m_s=-1} = 170 \text{ mK}$ (initialization into $|m_s = -1\rangle$), again with $T_1 = 220 \text{ ms}$. (d) Corresponding spin relaxation data recorded at 190 mT, revealing a ~ 50 times slower decay and an inverted equilibrium population compared to (a). (e) Simulation using $T_1 = 8 \text{ s}$ ($\Omega = \gamma = 30 \text{ mHz}$) and $T = 230 \text{ mK}$. (f) Simulation using $T_1 = 8 \text{ s}$ and spin-state initialization dependent temperatures $T_{m_s=0} = 500 \text{ mK}$ and $T_{m_s=-1} = 230 \text{ mK}$, yielding better agreement with the data recorded in (d) than the simulation in (e). All simulations consider a π -pulse fidelity of 95%.

At fields below the GSLAC, the effective spin bath temperature could therefore be lower for $|m_s = 0\rangle$ and higher for $|m_s = -1\rangle$ initialization, while the phononic spin bath thermalization appears to happen over a time-scale longer than our measurement time. This would be consistent with the long T_1 times in [6], where a global measurement on the entire diamond is insensitive to local spin diffusion and only the phononic thermalization is measured.

6.3. Summary and Outlook

In this chapter, we introduced the basics of T_1 relaxation in NV centers, and presented previous research on magnetic field dependent relaxation rates and low-temperature dynamics of NV spins down to mK temperatures. After explaining the experimental T_1 measurement sequence, we performed a relaxation measurement in a high-NV-density sample at room temperature. Going to low temperatures, we presented relaxation data with all four population curves with initialization and readout in the $|m_s = 0\rangle$ and $|m_s = -1\rangle$ state. A thorough analysis reveals the presence of asymmetrical and time-dependent relaxation rates between the spin states, pointing towards the possibility of a non-zero spin bath polarization. A measurement of relaxation rates versus bias magnetic field revealed information about the noise spectrum. Finally, at mK temperature, we found smaller relaxation rates than at 4 K and permanent population imbalance between the states that indicates a thermal polarization of the spins.

In further experiments, we aim at further testing the spin bath polarization hypothesis. This may be done by conducting a detailed analysis of the relaxation dynamics for different initialization powers and lengths, different confocal spot sizes and various and sample densities. An exciting experiment would be spatial imaging of the spin diffusion, using two optical foci which can be mutually scanned. Furthermore, a high-resolution spectrum of Ω and γ over bias magnetic field could yield better insights into the physics of the observed resonances, and relaxation rates at much higher fields would reveal the high-frequency end of the noise spectrum.

At mK temperatures, we could measure the Boltzmann distribution of the spin state populations as a function of magnetic field, and examine the long-time behavior of the complete spin re-thermalization. Systematically studying the evolution of the T_1 times between 4 K and 100 mK could provide insight into relaxation mechanisms not covered by the simple model in [93], which doesn't contain a temperature dependence of T_1 at low temperature. Additionally, spin-to-charge transfer could enable single-shot readout of the spin state. This would significantly improve the signal-to-noise ratio in T_1 measurements, which is especially useful at long relaxation times. Lastly, an exciting application would use the slow T_1 relaxation at low temperatures for sensitive measurements of external magnetic or electric noise sources – a concept that could be combined with NV scanning probe microscopy for spatial imaging.

7. Summary and Outlook

The goal of this thesis was to set up a dilution refrigerator NV magnetometry setup and image magnetic fields at mK temperature for the first time. On the journey, we addressed interesting superconductor physics by imaging Meissner screening and vortices at 4 K, and realized an improved out-of-plane (OOP) NV magnetometer orientation. We then put the dilution refrigerator into practice and used transport experiments to observe superconductivity in the oxide interface LAO/STO at mK temperature. In the same setup, we imaged electric currents and determined the absence of magnetic dipoles in the interface using scanning NV magnetometry. Furthermore, we examined T_1 relaxation at 4 K and 100 mK, where we found a significant increase of the T_1 time at mK temperature.

This project, and particularly the dilution refrigeration setup, offers potential for numerous exciting experiments. On the one hand, novel materials, previously unexplored in terms of mK magnetometry, should be examined using NV scanning probes. Promising candidates involve strongly correlated electron systems such as graphene and unconventional superconductors. On the other hand, the existing measurement procedures should be further optimized in terms of sensitivity and robustness, particularly concerning the bleaching of the NV ESR contrast (see A.3). Furthermore, the heat load of the MW delivery is particularly detrimental if mK temperatures are required. To that end, all-optical NV magnetometry might offer a promising protocol using coherent optical fields instead of a MW field to drive the spin. Finally, an entirely different approach would be the use of alternative color centers such as SiV centers for diamond-based magnetometry, promising good sensitivities at mK temperature, as well as all-optical control.

7.1. Summary

This thesis covered diverse subjects, primarily around low-temperature NV magnetometry. In particular, these were low-temperature NV magnetometry on superconductors, an optimized NV orientation for better sensitivity and applicability in scanning probe magnetometry. Furthermore, the thesis included transport and magnetometry measurements on an oxide interface and T_1 relaxation of the NV center at ultra-low temperature.

Chapter 2 provided the basis to understand NV magnetometry and dilution refrigeration. The optical initialization and readout of the NV spin was introduced through the level scheme of its ground state, excited state and long-living singlet state. The DC magnetic field measurement method was explained with the Zeeman splitting in the ground state and the optically detected ESR. We discussed the principle of scanning probe magnetometry for nanoscale imaging of magnetic stray fields, and pointed out the ideally suited NV center with atomic size and shallow implantation depth.

Furthermore, the sensor-sample distance dependency of resolution and sensitivity was examined for magnetic dipoles, demonstrating the crucial role of proximity especially for high sensitivity.

Entering the ultra-low temperature regime, we investigated the working principle of dilution refrigeration, using the phase separation between concentrated ^3He and dilute $^3\text{He}/^4\text{He}$. We then presented the concrete realization of the dilution refrigerator used in this work. The central components of the cryostat were the five cold plates, the dilution mixing chamber, the distillation chamber and the pulse tube pre-cooling. The top-loaded probe stick was used to bring the experiment to ultra-low temperatures, while maintaining an optical access to address the NV center. Lastly, we examined the dilution refrigeration cycle on the basis of the control panel of the gas handling system, where we discussed the relevant pumps, valves and working modes.

In the longest chapter of this thesis, chapter 3, we looked at NV magnetometry on the type-II superconductor YBCO, and determined the London penetration depth λ_L . Specifically, we imaged Meissner effect and vortices and performed a thorough analysis.

Concerning the Meissner effect, we developed a numerical model, which was capable of calculating the superconducting current density in a disk upon application of a perpendicular magnetic field, according to the 2nd London equation. This model allowed for simulation of the magnetic field measured by a scanning probe in a certain distance, as well as fitting to experimental data in order to extract λ_L . The simulation showed good qualitative agreement with a two-dimensional NV magnetometry image of a superconducting disk. Furthermore, a fit of the model to a high-resolution, one-dimensional magnetometry scan allowed for quantitative extraction of a penetration depth $\lambda_L = 249 \pm 3$ nm. Back-propagation of the magnetic field map yielded a map of the circular current in the disk, which is again in good agreement with the model. [15]

Concerning vortex imaging, we started by imaging an ensemble of vortices and found agreement with the expected vortex density according to the magnetic flow of one flux quantum. We examined a vortex in more detail and found a pronounced asymmetry of the magnetic field map due to the oblique NV orientation in standard (100) diamond. Finally, we used a high-resolution line scan to fit with three different analytical models. Due to the close proximity of the NV scanning probe, the simple monopole model completely failed to reproduce the data and yield a reasonable estimate of λ_L . Both Pearl and Carneiro model yielded a very good fit to the data and an accurate measure of $\lambda_L = 249 \pm 3$ nm, consistent with the value obtained in the Meissner effect measurements. [13]

Chapter 4 discussed the benefits of using OOP-oriented NV centers for magnetometry purposes along with their realization. We examined the improved optical excitation and collection efficiency of OOP NVs, as well as their superior sensitivity in magnetic field reconstructions. Furthermore, we discussed the facilitated interpretation of the resulting magnetometry images and the better applicability when large OOP bias magnetic fields are required. We realized such scanning probes using (111)-oriented diamond, and were able to identify the OOP-oriented NVs by ESR using an aligned field. Polarization rotation of the excitation laser alternatively allowed to distinguish all four NV orientations, and demonstrated the usefulness of polarization rotation to optimize optical addressing of non-OOP NVs. Finally, we were able to

employ the OOP-oriented NVs in nanoscale magnetometry, where we demonstrated the antisymmetric fields across edges of an OOP magnetized sample, which facilitates the interpretation of the data. [64]

In chapter 5, we examined the oxide interface LAO/STO and discussed the conditions at which it becomes conductive or superconductive. In our samples we measured electronic transport, imaged current flow and looked for signals of magnetic dipoles. The transport measurements revealed superconductivity by showing conductance steps at a critical temperature, current or field. Furthermore, we observed a spatially resolved photoconductivity by scanning the laser over the sample. We imaged the stray field of a current flow through an LAO/STO using NV magnetometry. Lastly, we looked for signals of the reported magnetic dipoles, which questioned the incompatibility of magnetism and superconductivity. However, we could exclude magnetic dipoles between a factor of four and four orders of magnitude smaller than the one in previous research, depending on the assumed distribution of the magnetic moment. We thereby showed that these dipoles are not intrinsic to LAO/STO.

In chapter 6 we discussed T_1 relaxation in an high-density NV ensemble at 4 K and 100 mK. We examined relaxation dynamics in the same sample which was used in previous research, allowing for a direct comparison of the results. In general, we observed similar relaxation rates at 4 K, but a closer analysis showed that only time-dependent rates could satisfy the experimental data, a phenomenon that might be explainable with spin diffusion. A simple model allowed to extract both rates Ω and γ at magnetic fields up to 200 mT, revealing a prevalence of magnetic noise and a general decrease of the noise level. Finally, we measured T_1 relaxation at 100 mK where the NV spin starts to acquire a significant thermal equilibrium polarization. We found long T_1 times on the order of seconds and indeed observed unequal spin populations after relaxation corresponding to temperatures between 75 mK and 300 mK. However, we unexpectedly found different spin populations for the two initialization states, tentatively explainable by two different temperatures.

7.2. Outlook

The experiments in each of the chapters have the potential for several follow-up experiments, which can clarify uncertain aspects, measure unknown parameters and expand into new areas.

Concerning superconductivity, an expansion of our results would be the study of different superconductor types. Only in deep type-II superconductors, the magnetic field penetration obeys the London equations. Type-I and boarder type-I/type-II superconductors obtain a different shape of field penetration, which could be measured through Meissner imaging, and used to determine the ratio of λ_L and ξ . Analogously, vortices in superconductors at the crossover between type-I and type-II regimes have a different shape than vortices deep in the type-II regime. Furthermore, the study of how far in the type-I regime a real vortex is stable could bring new insights to superconductivity. Furthermore, since many superconducting elements have a critical temperature $T_c < 4$ K, we could use the dilution refrigerator to examine these low T_c superconductors, which have not been studied with scanning probe magnetometry before.

Our OOP NV scanning probes in (111) diamond could be further improved using an optimized parabolic nanopillar shape with better waveguiding properties, in order to obtain increased count rates and magnetic field sensitivity. Deterministic alignment of the nanopillars onto the corresponding NV centers could significantly increase the yield of such scanning probes, which is otherwise low due to the three unwanted NV orientations. Due to their intrinsic advantage in sensitivity, the OOP orientation might become a standard in NV scanning probe magnetometry, provided that the supply of high-purity (111)-oriented diamond further increases in the future.

The oxide interface LAO/STO can still be explored in other ways by our experimental setup. To learn more about the photoconductivity of LAO/STO, we could examine its conductivity as a function of laser position, using different laser powers and channel widths. Furthermore, we could use NV magnetometry to image the electrical current flow after a previous laser exposure, and thus directly observe how the current is influenced by the laser. By using more sensitive NV scanning probes and AC magnetometry, we could image superconducting currents and therefore examine the distribution of the superconducting density in the interface. In case the sample shows magnetism, we could also image the distribution of the magnetism and superconductivity, and thereby shed light onto their unconventional combination.

Concerning T_1 relaxation, we could still explore the temperature regime between 4 K and 100 mK and examine the transition from the short to the long T_1 times. At mK temperature, we could measure the T_1 relaxation up to longer decay times, to observe the complete spin thermalization despite the different initial temperatures. With these long T_1 times, it would be highly beneficial to use spin-to-charge transfer to obtain single shot readout of the spin state [99], allowing for shorter measurement times or lower NV density samples.

To reliably interpret the data, we should test the spin diffusion hypothesis, since the observed relaxation may not represent the real phononic T_1 time, but rather some dynamics of the spin bath. This we could do by increasing the initialization and detection volume by defocusing the confocal microscope. In that case, a change of the observed relaxation time would indicate a large influence of spin diffusion, since the fundamental T_1 time should remain unchanged. Additionally, we could simulate the spin dynamics in more detail, and examine how we could use it for insightful experiments. Finally, we could use the long T_1 times for sensitive measurements of magnetic or electric noise sources, a technique that could be combined with NV scanning probe microscopy for spatial imaging.

Furthermore, we will research other materials that show exciting properties at ultra-low temperature using NV magnetometry. Graphene is such a candidate which is predicted to have intrinsic magnetism at ultra-low temperature (Fig. 7.1a). Below 1 K, the electron spins in a graphene nano-ribbon are predicted to order antiferromagnetically across the ribbon with the largest net spins at the edges [100], causing a stray magnetic field which would be detectable by a magnetometer (Fig. 7.1b,c). The corresponding spin correlation length and thus the allowed ribbon width is not known yet [100], but even a narrow ribbon width on the order of 20 nm could potentially be resolvable by NV magnetometry.

On the other hand, graphene shows spin polarization in quantum Hall states. In the fractional quantum Hall states, however, it is not clear whether spins are polarized [101] and whether they can form domains [102]. Also, the quantum Hall states

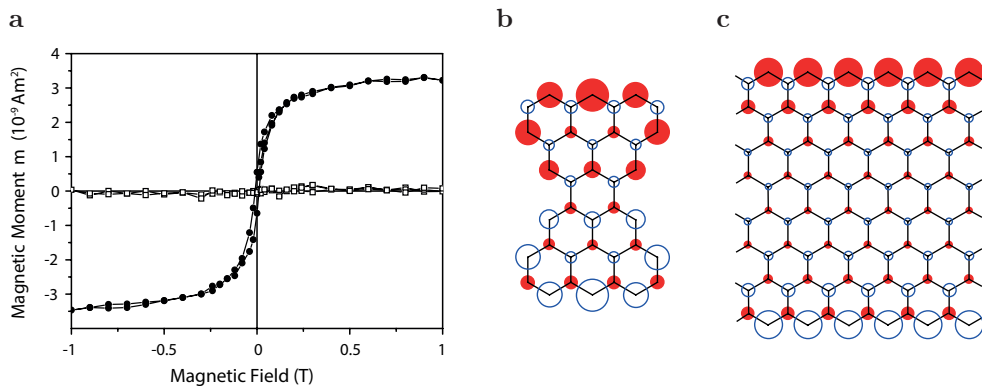


Figure 7.1.: Magnetism in graphene. (a) Magnetic moment vs. bias magnetic field for standard graphene (white squares) and proton irradiated graphene (black circles). The irradiation damages the graphene and causes ferromagnetic edges throughout the sample, yielding a high magnetization saturation with a small hysteresis. (b) Simulation of spin polarization in a small bowtie-shaped graphene flake. Filled red and empty blue circles denote opposite sign of the spin, and the size denotes the degree of polarization. (c) Simulated spin polarization for an armchair nano-ribbon. Figures adapted from [100].

are known to support broken symmetry states [103], which have however not been addressed by direct imaging yet. To clarify the nature of these states and examine their spatial properties, one could apply NV magnetometry in our mK setup.

Other promising candidates to address, using NV magnetometry at mK temperatures, are unconventional superconductors. The p -wave superconductor Sr_2RuO_4 [104] for example exhibits time-reversal symmetry breaking and is therefore expected to exhibit spontaneous supercurrents along sample edges and domain walls [105]. Even though these supercurrents would cause magnetic stray fields, they have not been imaged yet [106], possibly due to a small domain size. In this case, NV magnetometry could employ its high spatial resolution and detect the small magnetic fields.

Furthermore, Sr_2RuO_4 is reported to host half-quantum vortices [19], however no direct spatial imaging of these has been performed yet. Therefore, the quantitative NV magnetometer in close proximity could directly measure the flux of the vortex and deliver reliable evidence for the half-quantum number of the vortex.

Apart from new sample materials, additional strategies involve the optimization of our NV magnetometers at mK temperature which we will outline in the following. One would be the automatized optimization of parameters for NV magnetometry. On the one hand, we have applied several improvements to our measurements sequences that enhance sensitivity and thermal load, such as pulsed ESR and narrow sampling width around the ESR dip. On the other hand, however, the relatively tedious process of tuning the relevant parameters often led to not realizing these improvements. Therefore, an improved, intelligent software that automatically optimizes the measurement parameters could make the lab work more efficient and significantly increase the real

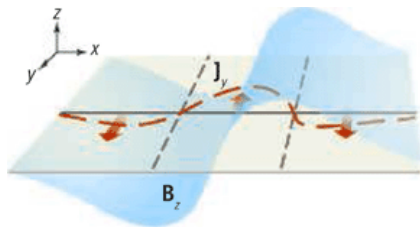


Figure 7.2.: Currents and magnetic fields at a domain wall in the unconventional superconductor Sr_2RuO_4 . A domain wall between two domains related by time-reversal symmetry lies in the y-z plane (between the two gray lines). It obtains chiral spontaneous supercurrents (red dashed line) parallel and antiparallel to the domain wall. The resulting magnetic field is depicted by the blue area and should be experimentally measurable. Figure adapted from [105].

magnetic field sensitivity.

Furthermore, all-optical NV magnetometry might entirely circumvent the use of a microwave antenna. Due to the large heating at the sample by the MW delivery hardware, all-optical magnetometry would be highly relevant for experiments in the dilution fridge, especially when temperatures below 100 mK are required during continuous measurement. For all-optical magnetometry, it is necessary to have coupling of the excited $|m_s = 0\rangle$ and $|m_s = \pm 1\rangle$ states, through diamond lattice strain or by working at the excited state level anti-crossing (ESLAC). A further ingredient is an NV optical linewidth smaller than zero-field splitting and a resonant laser with a tunable modulation frequency to generate two coherent optical fields. When these two frequencies correspond to the transition from $|m_s = 0\rangle$ and $|m_s = \pm 1\rangle$ to a common excited state, a "Λ scheme" is formed and population can be transferred between the GS $|m_s = 0\rangle$ and $|m_s = \pm 1\rangle$ states (Fig. 7.3a). However, after a few optical cycles with photon emission, the NV falls into a coherent dark state with no population in the excited state and therefore no photon emission, a process called coherent population trapping (CPT) [107]. When sweeping the frequency of one of the two optical fields, the occurrence of CPT at the resonance frequency shows a pronounced loss of fluorescence with up to 100% contrast (Fig. 7.3b).

Since the resonance frequency for CPT is given by the energy difference of the two ground states, the magnetic field can be measured by the Zeeman splitting, in analogy to the MW driven ESR measurements performed in this work (Fig. 7.3b). Due to the high measurement contrast, CPT could thus be used for sensitive magnetometry while having a much smaller thermal footprint without MW delivery. Furthermore, an adaptation to this approach would use the all-optical NV spin control. Here, CPT is not used to read out the NV spin, but to initialize it in a superposition of $|m_s = 0\rangle$ and $|m_s = \pm 1\rangle$, once the laser frequencies match the CPT condition [108]. Subsequently, the spin state could be read out using the standard procedure with a green, non-resonant laser. Although this standard readout yields only a contrast on the order of 10%, the fast initialization rate around 50 MHz [108], and the high count rate with the non-resonant excitation, may provide a highly sensitive magnetometry protocol.

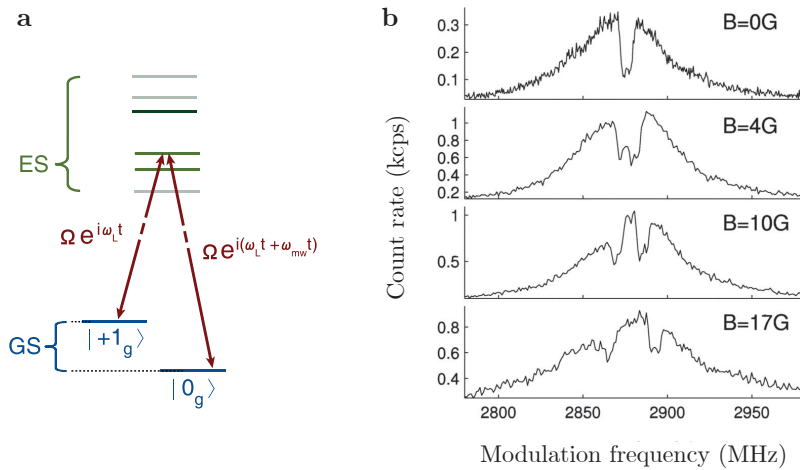


Figure 7.3.: All-optical control for NV magnetometry. (a) Λ scheme coupling the $|m_s = 0\rangle$ and $|m_s = +1\rangle$ spin states in the ground state over a shared excited state. Two optical fields with frequency ω_L and $\omega_L + \omega_{MW}$ drive the two transitions at a rate Ω . Figure adapted from [108]. (b) Magnetometry through coherent population trapping (CPT). The count rate as a function of laser modulation frequency shows a substantial decrease of brightness when the two optical fields match the Λ configuration. Measurements at magnetic fields between 0 G and 17 G demonstrate the Zeeman splitting between $|m_s = +1\rangle$, allowing for magnetic field sensing analogously to ESR. Figure adapted from [107].

Lastly, an entirely new route would be the use of SiV centers for scanning probe magnetometry. The SiV center in diamond consists of an interstitial silicon atom between two diamond lattice vacancies and has a spin $S = \frac{1}{2}$ and an orbital ground state splitting of 40 GHz. Importantly, it offers straightforward all-optical control through a "Lambda scheme" that is created by slightly misaligning the bias magnetic field from the SiV symmetry axis [109]. Analogously to the NV center, the Zeeman splitting can be used for magnetic sensing, and embedded in a diamond scanning probe the SiV could provide nanoscale resolution in imaging. Furthermore, due to its inversion symmetry, the SiV center is less sensitive to electric field noise and thus offers narrow optical linewidths, even when close to the surface and after applying nanofabrication procedures to the diamond [110]. Together with its good spin coherence times at mK temperature [110], the SiV thus constitutes a promising magnetometer at mK temperature to be explored in the future.

A. Appendix

A.1. Dilution Refrigerator Manual

This manual aims to support the user to safely handle the CF-CS81 dilution refrigerator from Leiden Cryogenics (Fig. A.1). The focus lies on the cryostat cooldown and warmup procedures as well as the insertion and extraction of the probe stick.

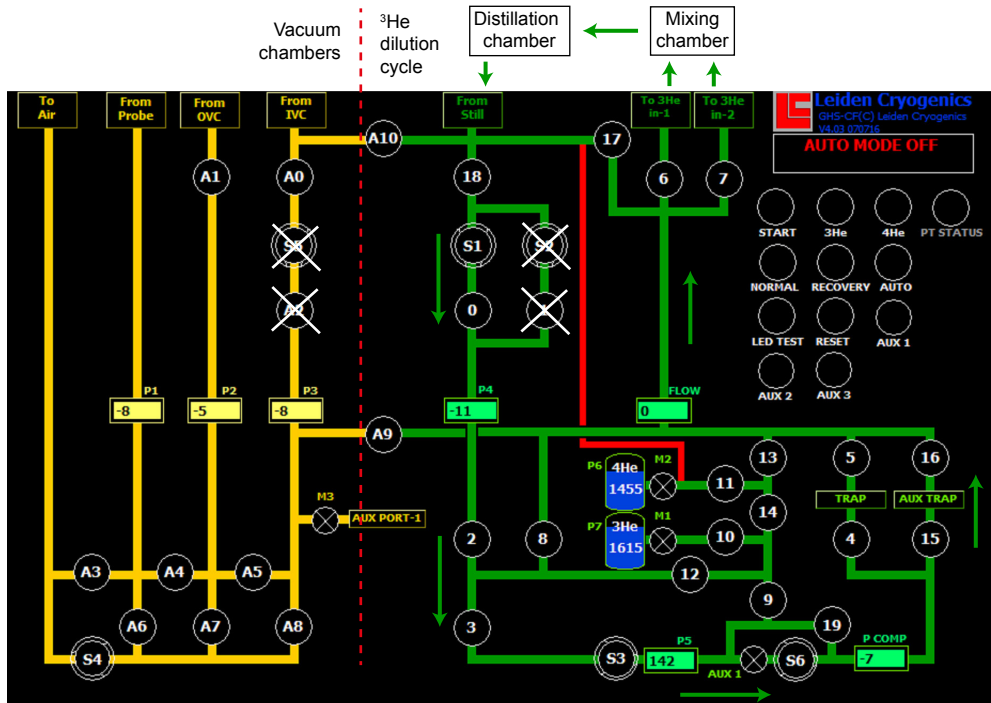


Figure A.1.: Control panel of the DF-CS81 dilution refrigerator from Leiden Cryogenics.

Cooldown from RT to 4 K

- Pump IVC with rough pump S4. Open S4, A8, A0. Wait until IVC pressure reaches a few mbar.
- Pump IVC with external turbo pump. Start turbo and carefully open it to the IVC using A4, A5 and A0. Pump until 8×10^{-3} mbar is reached in the IVC. Pumping

with an external turbo is much faster, since the circuit is shorter and has larger tube diameters.

- Pump Still with S1, S4, A8, A9, 8, 2, 0, S1 and 18. Typical pressure is 6×10^{-4} mbar.
- Pump traps with S1 by opening 5 and 16, while S4, A8 and A9 are open. This can be done in parallel to pumping the Still.
- **Start of optional circulation test:** This needs to be done with a warm cryostat (room temperature). It is recommended to do it every time the cryostat is warm.
- Make sure the Still pressure is below 6×10^{-4} mbar by pumping as described above.
- Close A8 and 8.
- Insert 1 bar of He through M3, measured in P3. Make sure to first pump on the external He line, to get cleaner He.
- Close M3, close 18, open 6.
- Measure the time until Still pressure reaches 1 mbar.
- Close 6 and open A8, 8 and 18, to pump the Still again.
- Do the same for the impedance 7. **End of optional circulation test.**
- Pump Still to 6×10^{-4} mbar as described above.
- Flush the IVC four times with helium to remove most of the remaining air. Important to avoid gas freezing inside the cryostat. To that end, close A8 and open A0 and insert 0.5 bar of He, then pump it through A8 and S4. Repeat three times.
- Pump IVC and OVC with external turbo pump. Open M4, IVC-probe and A1. Pump until bottom pressure is reached i.e. IVC and OVC at around 5×10^{-3} mbar. After that, insert 10 mbar to IVC (MaxiPiraniGauge), through M3 and A0. Keep pumping OVC.
- Connect full-range temperature sensor: Connect the readout cable from 50mK-probe sensor (channel 7) to the MC-PT1000 port.
- Cooldown cryostat to 80 K with Liquid Nitrogen (LN_2) and pulse tube as follows: Turn on pulse tube compressor. Connect LN_2 line and insert between 1 bar and 2 bar in LN_2 dewar, until you reach 80 K (4K-plate and magnet).
- At this point, turn on sorb pump heater using 30 mA to prevent exchange gas being pumped by the sorbs. Make sure that you collect the LN_2 coming out of the cryostat with a tube, for example filling up the cold traps. Then turn off LN_2 cooling and cool down to 4 K only with the pulse tube. The temperature may rise a bit when you first turn off LN_2 cooling. Check the cooling progress through the decreasing pressure.

Insert the Probe Stick at 4 K

- Install probe stick shield around experiment below MC-plate. Before disconnecting the cables, keep a safety distance between tip and sample during the handling. Be aware that the tip and the sample have some drift during the cooldown. Usually they drift upwards (around $100 \mu\text{m}$ - $200 \mu\text{m}$), so you will have to drive down after the cooldown.

- Use gloves to touch the probe stick. Clean the thermal clamping contacts with IPA. Clean vacuum seal position before closing. Insert the probe stick into the flexible tube on top of the cryostat. Fix it with the 6 screws to obtain a vacuum-tight seal.
- Pump out probe with external turbo, until reaching about 5×10^{-3} mbar. Usually pump overnight.
- Make sure that $B = 0$.
- Switch off the sorb pump heater to decrease exchange gas in IVC.
- Open the big manual gate valve and carefully drive down the probe. Usually, one person stands on top of the cryostat and checks that everything is fine (cables etc.). The other person driving the probe stick is ready to stop, if the resistance suddenly increases and the probe stick gets stuck and bends. Make sure that the metal rods fit through the holes when getting to the bottom. Drive down almost to the limit and then drive up to the standard height of 335 mm. Thermally connect the probe stick by applying 25 bar to the clamping mechanism. Put 10 mA on the sorb pump heater to release some He exchange gas.
- Pump out OVC if the pressure rises above bottom of sensor range.
- The cryostat heats up to around 60 K when inserting the warm probe. Wait about 12 h to reach 4 K again.

Cool Down to mK Temperature

- Only cool down to mK temperature with either the probe stick or the heat shield inside the cryostat. Make sure no heat load is on the probe: Turn off MW and laser, set scanner voltages to 0 V and positioner readout voltage to 0 V.
- Pump out the warm traps with S4, A8, A9, 5, 16. Then cool down the traps, make sure they have enough LN_2 .
- Pump out the exchange gas from the IVC with the external turbo (through probe), before cooling down to mK. Apply 30 mA on sorb pump heater and Still plate during pumping. Additionally, you can turn off the pulse tube compressor for 15 min to increase the temperature to 10 K and release more exchange gas. Stop pumping and turn off the heaters when reaching 1×10^{-3} mbar in the IVC.
- Start condensing ^4He and ^3He by pushing the "Auto" button on the gas handling system (GHS). Check that the helium condensation goes fine (decreasing pressure in the tanks). Condensation of ^4He should take around 3 h and of ^3He around 1 h.
- When the system is cold and the flow is low (< 1500 mbar/min), open only one ^3He line (line 7) and open both traps. Put 10 mA on the Still plate heater to maintain a certain flow. For high heat loads, open both ^3He lines and increase the flow using > 10 mA on the Still plate heater.
- Usually, temperatures of < 50 mK are reached on the MC-probe and sample without heat load.
- Be careful using large heat loads at mK temperature, e.g. from high MW powers. Otherwise the temperature increases a lot, above 1 K, and the cooling power of the dilution fridge reaches its limits. Make sure not to use more MW power than needed, and turn it off when not measuring. Keep the MW duty cycles short if possible (e.g. with pulsed ESR). Continuous ESR causes a lot of heat.

Warm Up from mK to 4K

- Make sure that $B = 0$.
- Turn off the Still plate heater. Try to reach a small flow < 1000 ml/min. A high flow would put a larger load on the turbo when changing the mode to Recovery (backing pump turns off for 30 s).
- To start the recovery of the mixture: Disable Auto mode by pressing the "Auto" button, and press "Recovery" and "Auto".
- To speed up the recovery, you can increase the heat load by releasing exchange gas (10 mA on sorb pump heater), Still plate heater (10 mA) or some MW power (-10 dBm). Aim for at least 2 h for the recovery, stay below 1 mbar of Still pressure.

Extracting the Probe Stick at 4 K

- If the Cryostat is at mK temperature, wait at least until all ^3He is recovered, before you start to drive up the probe stick.
- Make sure that $B = 0$.
- Turn off the sorb pump heater.
- Make sure that all scanner voltages are at 0 V. Change the voltage limits back to RT (3 V).
- Carefully drive up the probe stick, ready to stop if there is a large resistance. One person can stand on the cryostat and hold the probe stick lifter straight. Don't forget to remove the cables before you get to the top. Be careful not to drive too far up.
- When at the top, carefully close the manual gate valve to the ICP. Reconnect the Fischer cables 1 and 2 to keep the scanners grounded during warmup. To warm up the probe stick, insert 100 mbar of clean Helium gas into the probe chamber. Wait 2 hours, until the probe is warm. Vent the probe stick with Helium and open the top. Fix the probe stick with the aluminum piece holder and drive down the flexible tube. Two people take out the probe stick: One person stands on top of the cryostat (taking care of the top) and one on the floor (taking care of the bottom of the probe stick).

A.2. Cooling Power

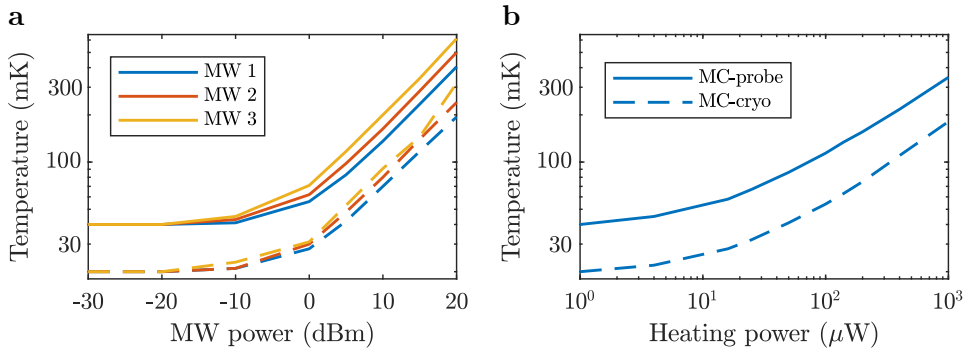


Figure A.2.: Measured cooling power of CF-CS81 dilution refrigerator as a function of MW power and heating power. (a) Temperature as a function of applied MW power for three different MW configurations (see below), all thermally connected to MC-probe stage. Note that due to the 1.5 m long cable from the MW generator to the cryostat, the actual power at the cryostat entrance is 2 dB lower than the stated power. Solid lines denote the temperature at the MC-probe, the lowest stage in the probe stick, and the dashed lines denote the temperature at the adjacent MC-cryo cryostat plate. MW 1 is an open-end coax cable. MW 2 is a shorted coax cable using a gold bond wire. MW 3 passes through a 5 mm long bond wire antenna on a sample holder and exits the cryostat through a different coax line. Significant heating is observable from -15 dBm on. The linear slope of $\sim \frac{1}{2}$ in the log-log plot above 0 dBm suggests a quadratic temperature dependence of heating rate on MW power [30]. (b) Same measurement using a dissipative resistance heater, thermally connected to MC-probe. Similar relations are observed as in (a), although the heating is stronger since all power is dissipated at MC-probe, and not partially on the MW lines along the probe stick as in (a).

A.3. NV Bleaching

Bleaching of the NV center ESR contrast has been a major challenge in the mK setup. In all scanning probe magnetometry experiments at low temperatures in this setup (4K or mK), we have observed an accelerated decay of ESR contrast and brightness, preventing measurements with high signal-to-noise ratio after just a few days (Fig. A.3). Furthermore, in a bleached tip we often found a distinct change to the negatively charged NV^- state (Fig. A.4a), which explains this loss of contrast and brightness. Intriguingly, exposure to an SEM electron beam or UV light at room temperature has restored the ESR contrast and the NV^-/NV^0 ratio (Fig. A.4b). First trials to revive NV^- in-situ at low temperature using UV have not been successful, as the delivery e.g. of UV light through the optical path is difficult. However, new plans involve the use of a UV LED directly at the microscope head.

This bleaching problem already at 4K was unexpected, since another LT setup we operate at 4K, an attoLIQUID 1000, does not show this problem. A clear difference between the two setups is the exchange gas based cooling in the LT setup, while

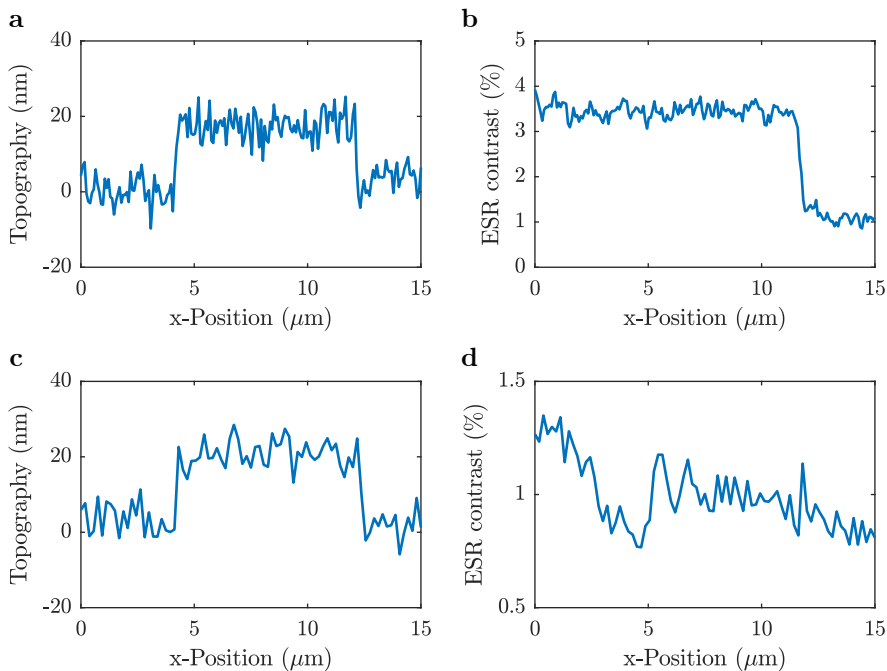


Figure A.3.: Bleaching of ESR contrast during measurement. (a) AFM topography over a $10\ \mu\text{m}$ channel of LAO/STO. Same scan as presented for current imaging in Fig. 5.8. (b) Simultaneously measured ESR contrast. The contrast stays constant until it suddenly drops by a factor of 3, possibly related to the topographical edge (c) Topography of a consecutive scan over the same channel. (d) The ESR contrast decreases further, below 1%, where it is hardly usable for magnetometry scans. This time, the decrease is continuous and not attributable to a topography feature.

the mK setup has a vacuum chamber and provides cooling through direct thermal coupling. Since both scanning in AFM contact and laser exposure accelerated the contrast loss, we identified the following possible causes for bleaching:

- Adsorption of gas at the surface of the cooled tip, possibly induced by the green laser light.
- Increased picking up of dirt due to high vibration level from the pulse-tube.
- Charging of the insulating tip due to vacuum environment, bending valence and conduction band close the the tip surface, and thereby stabilizing NV^0 .

At this point, having deposited several conductive coatings to the scanning tip without attaining significant improvements for the bleaching problem, the charging hypothesis is rather unlikely. While the reduction of the vibration level would be hard to realize, current efforts are aiming to provide a cleaner environment for the tip. Additionally, exchange gas based cooling would provide more consistent temperatures to all surfaces and thus further prevent adsorption of gas at the scanning probe.

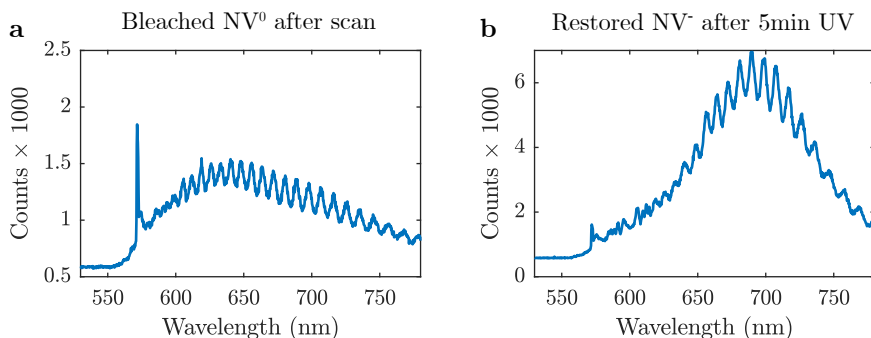


Figure A.4.: NV^0 and NV^- fluorescence spectrum before and after UV exposure. (a) Room-temperature spectrum of a bleached tip after using for scanning probe magnetometry in the dilution refrigerator at 4 K. The NV is both low in ESR contrast and in brightness. The emission centered around 640 nm indicates an NV^0 phonon sideband. The peak at 572 nm is the Raman line of the 532 nm laser. (b) Same scanning probe after 5 min of UV-A exposure (Thorlabs M365FP1), still mounted in the tip stack. The spectrum has shifted towards 700 nm and become much brighter, demonstrating the conversion to the NV^- charge state, as confirmed later through an increased ESR contrast. Note that in both spectra, the ripples arise from an interference due to a partial reflection at the top surface of the diamond scanning probe.

A.4. Code Snippets

Meissner Effect Simulation

This code is designed to simulate the Meissner effect in a superconducting disk, in terms of currents and magnetic fields as derived in Sec. 3.2.1 (cf. Fig. 3.5). In particular, we use the 2nd London equation and consider a perpendicular bias magnetic field. To obtain the final current distribution in the disk, we iterate between calculation of currents and updated magnetic fields. We can use this model to fit to experimentally measured field data B_{NV} as a function of lateral position in a magnetometry scan. Thus, the London penetration depth λ_L and the NV-superconductor distance z_{SC} can be extracted. In this code snippet, we consider a 1D linescan (cf. Fig. 3.8), however, the 2D case is simulated analogously (cf. Fig. 3.7).

```

1  % Script to fit experimental Bfield data with the Bfield from
2  % simulated current distribution in a superconducting disk.
3  % Define fixed and free parameters, define fitting function, fit.
4
5  %%%%%%%%%%%%%%%%%%%%%%%%%%%%%%%%%%%%%%%%%%%%%%%%%%%%%%%%%%%%%%%%%%%%%%%%%
6  % Fixed parameters
7  %%%%%%%%%%%%%%%%%%%%%%%%%%%%%%%%%%%%%%%%%%%%%%%%%%%%%%%%%%%%%%%%%%%%%%%%%
8
9  %% Load x-positions and Bfields from experiment
10 experiment = load('experiment.xx');
11 x = experiment.x;
12 Bfield = experiment.Bfield;
13
14 %% Sample parameters
15 rSC = 3e-6;           % Radius of superconducting disk
16 zSC = 119e-9;        % Height of superconducting disk
17 zStep = 140e-9;      % Step size around SC disk
18 rPillar = 0.27e-6;   % Distance between disk edge and AFM step
19
20 %% Resolution in simulation, number of current loops
21 rSCres = 300;         % Radial resolution
22 zSCres = 12;         % Axial resolution
23
24 %% Summarize fixed parameters in array
25 fixParameters = [rSC, zSC, rSCres, zSCres, zStep, rPillar];
26
27 %%%%%%%%%%%%%%%%%%%%%%%%%%%%%%%%%%%%%%%%%%%%%%%%%%%%%%%%%%%%%%%%%%%%%%%%%
28 % Initial fitting parameters
29 %%%%%%%%%%%%%%%%%%%%%%%%%%%%%%%%%%%%%%%%%%%%%%%%%%%%%%%%%%%%%%%%%%%%%%%%%
30
31 zDistance0 = 70e-9;   % z-distance of sensor to disk
32 lambda0 = 250e-9;     % London penetration depth
33
34 NVtheta0 = 54.7;      % Polar angle theta of NV center
35 BzBias0 = 1.6e-3;    % Bias field along z
36 xFactor0 = 1.2;      % Calibration factor on x-position
37 xCenter0 = -1.2e-6;  % Position of disk center
38
39 %% Summarize initial fitting parameters in array
40 v0 = [zDistance0, lambda0, NVtheta0, BzBias0, xCenter0, xFactor0];
41

```

```
42 %%%%%%%%%%
43 % Fitting
44 %%%%%%%%%%
45
46 %% Define fitting function: simulated sata - measured data
47 fun = @(v) BNVCcurrentLoops(v,fixParameters,x) - Bfield;
48
49 %% Fit: least-square nonlinear solver
50 vFit = lsqnonlin(fun,v0);
51
52 %% Retrieve fitted parameters from Fit
53 zDistance = vFit(1);
54 lambda = vFit(2);
55 NVtheta = vFit(3);
56 BzBias = vFit(4);
57 xCenter = vFit(5);
58 xFactor = vFit(6);
```



```
59 % Calculate Bfields
60 %%%%%%%%%%%%%%%%%%%%%%%%%%%%%%%%%%%%%%%%%
61
62 %% Bfield due to currents in disk
63 Bz = 0; % Axial Bfield
64 Br = 0; % Radial Bfield
65
66 %% Add Bfield contributions Bz and Br from all current loops
67 for i = 1:rSCres
68     for j = 1:zSCres
69         Bz = Bz + BzCurrentLoop(r(i,j),I(i,j),ro,zDistanceStep+z(i,j));
70         Br = Br + BrCurrentLoop(r(i,j),I(i,j),ro,zDistanceStep+z(i,j));
71     end
72 end
73
74 %% Calculate Bx from Br
75 for i = 1:xRes
76     Bx(i) = Br(i) .* xScaled(i)./ro(i);
77 end
78
79 %% Calculate the NV vector components
80 NVphi = 0; % Azimuthal angle of NV, set manually
81 NVx = sind(NVtheta) * cosd(NVphi);
82 NVy = sind(NVtheta) * sind(NVphi);
83 NVz = cosd(NVtheta);
84
85 BNV = (Bx*NVx + By*NVy + Bz*NVz) + NVz*BzBias; % projection on NV axis
```

```

1  function [ I ] = CurrentSimulation(lambda,rSC,zSC,rSCres,zSCres)
2
3  % Function to simulate the current density in a superconducting disk at
4  % a bias magnetic field along z, according to the 2nd London equation:
5  % In SI units: rot j = -(ne^2)/m*B = -1/lambda^2 / mu0 * B
6  % Cylinder symmetry: rot j = j/r + dj/dr
7  % Therefore: dj/dr = -j/r -1/(lambda^2*mu0) * Bz
8  % Numerical method: calculate the currents in a 2D array of current
9  % loops (in r and z), and calculate the new Bfield at each position.
10 % Iterate several times to obtain final current distribution.
11 % Damped iteration to avoid divergence.
12
13 mu0 = 4*pi*10^-7;           % Bohr magneton
14 factor = -(1/lambda)^2 / mu0; % Factor in london equation
15
16 %%% Create 2D array for currents an Bfields in disk
17 dr = rSC/rSCres;
18 dz = zSC/zSCres;
19 rArray = linspace(0.5*dr,rSC-0.5*dr,rSCres);
20 zArray = linspace(0.5*dz,zSC-0.5*dz,zSCres);
21 [z,r] = meshgrid(zArray,rArray);
22
23 %%% Simulation parameters
24 BzBiasSim = 1;           % Bias field in simulation, set to 1
25 iterations = 10;        % Iterations between currents and Bfields
26 dampFact = 1.8;        % Damping factor in iteration
27 diffIterations = 200;   % Iterations for differential equation
28
29 %%% Initialize current loops and Bfields
30 I = zeros(rSCres,zSCres); % 2D array of currents
31 I2 = zeros(rSCres,zSCres); % I2 for Iteration
32 Bz = ones(rSCres,zSCres) * BzBiasSim; % Bz, start with BzBiasSim
33
34 %%%%%%%%%%%%%%%%%%%%%%%%%%%%%%%%%%%%%%%%%%%%%%%%%%%%%%%%%%%%%%%%%%%%%%%%%
35 % Simulation of currents and Bfields
36 %%%%%%%%%%%%%%%%%%%%%%%%%%%%%%%%%%%%%%%%%%%%%%%%%%%%%%%%%%%%%%%%%%%%%%%%%
37
38 %%% Iterate between calculation of current loops and new Bfields
39 for k = 1 : iterations
40
41     %%%%%%%%%%%%%%%%%%%%%%%%%%%%%%%%%%%%%%%%%%%%%%%%%%%%%%%%%%%%%%%%%%%%%%%%%
42     % Calculate current loops
43     %%%%%%%%%%%%%%%%%%%%%%%%%%%%%%%%%%%%%%%%%%%%%%%%%%%%%%%%%%%%%%%%%%%%%%%%%
44
45     %%% First calculate current loops in center of disk
46     for n = 1:zSCres
47         for i = 1:diffIterations % Euler method. Iterate ...
48             differential equation, gradually increase second term
49             I2(1,n) = 0.5*dr*(i/diffIterations)^0.1 * ...
50                 (dr*dz*factor*Bz(1,n) - I2(1,n)/r(1,n));
51         end
52     end
53     %%% Calculate all other current loops
54     for m = 2:rSCres
55         for n = 1:zSCres
56             for i = 1:diffIterations % Euler method. Iterate ...
57                 differential equation, gradually increase second term
58                 I2(m,n) = I2(m-1,n) + dr*(i/diffIterations)^0.1 * ...

```

```
        (dr*dz*factor*0.5*(Bz(m,n)+Bz(m-1,n)) - ...
        (I2(m,n)+I2(m-1,n))/(r(m,n)+r(m-1,n)));
56     end
57     end
58     end
59
60     I = ((dampFact-1)*I + I2) / dampFact;    % Damping of iteration
61
62     %%%%%%%%%%%%%%%%%%%%%%%%%%%%%%%%%%%%%%%%%
63     % Calculating new Bz
64     %%%%%%%%%%%%%%%%%%%%%%%%%%%%%%%%%%%%%%%%%
65
66     for m = 1:rSCres
67         for n = 1:zSCres
68             % Bz contributions of each current loop
69             manyBz = BzCurrentLoop(r,I,r(m,n),-z+z(m,n));
70             manyBz(isnan(manyBz)) = 0;
71             % Add all current loop contributions to BzBias
72             Bz(m,n) = sum(sum(manyBz)) + BzBiasSim;
73         end
74     end
75 end
```

```

1 function [ Bz ] = BzCurrentLoop(rLoop,I,x,zDistance)
2
3 % Function to calculate Bz from a current loop with I and radius rLoop,
4 % at position x and zDistance
5
6 mu0 = 4*pi*10^(-7);
7
8 z = zDistance;
9 ro = abs(x);
10
11 k2 = 4*rLoop*ro ./ ((rLoop+ro).^2 + z.^2);
12 [K,E] = ellipke(k2);
13
14 Bz = I.*mu0./(2.*pi) .* 1./sqrt((rLoop+ro).^2 + z.^2) .* ...
      ((rLoop.^2-ro.^2-z.^2)./((rLoop-ro).^2+z.^2).*E + K);
15
16 end

```

```

1 function [ Br ] = BrCurrentLoop( rLoop,I,x,zDistance)
2
3 % Function to calculate Br from a current loop with I and radius rLoop,
4 % at position x and zDistance
5
6 mu0 = 4*pi*10^(-7);
7
8 z = zDistance;
9 ro = abs(x);
10
11 k2 = 4*rLoop*ro ./ ((rLoop+ro).^2 + z.^2);
12 [K,E] = ellipke(k2);
13
14 Br = I.*mu0./(2.*pi) .* 1./sqrt((rLoop+ro).^2+z.^2) .* (z./ro) .* ...
      ((rLoop.^2+ro.^2+z.^2)./((rLoop-ro).^2+z.^2).*E - K);
15
16 end

```

Spin Diffusion Simulation

Dipole-dipole interactions between close-by NV spins cause cross-relaxation and thus spin diffusion. The following function is used to simulate the spin diffusion upon initialization by a focused laser pulse, and a waiting time τ , as in a T_1 measurement (cf. Fig. 6.6). The simulation is done in 2D, as an approximation to the long aspect ratio of five of the laser focus (NA= 0.82, $\lambda = 532\text{nm}$). However, simulation in 1D or 3D could be done analogously. In particular, we simulate the polarization signal by iterating in small steps between polarization creation in the Gaussian laser profile, and simultaneous diffusion through a Gaussian convolution. The former we scale with the laser initialization rate, and for the latter we consider a diffusion profile corresponding to the the spin-spin interaction rate at a specific NV concentration. After the initialization pulse, we only execute diffusion steps for relaxation time τ . Therefore, we can show that spin diffusion out of the initialization volume can be a strong factor for the locally observed polarization loss, and thus significantly decrease the measured T_1 time.

```

1 function polarization = SpinFunction2D(x,initRateHz,laserTime,timeTau)
2
3 % Function to calculate the diffusion of spin polarization, as a
4 % function of laser initialization rate, initialization pulse time,
5 % and waiting time tau.
6 % Laser initialization and spin diffusion are iterated in small steps.
7 % spin distance, flip-flop rate and laser focus size are calculated.
8
9 %%%%%%%%%%%%%%%%%%%%%%%%%%%%%%%%%%%%%%%%%%%%%%%%%%%%%%%%%%%%%%%%%%%%%%%%%
10 % Calculate interaction between spins
11 %%%%%%%%%%%%%%%%%%%%%%%%%%%%%%%%%%%%%%%%%%%%%%%%%%%%%%%%%%%%%%%%%%%%%%%%%
12
13 dDensity = 3.51;           % Density of diamond, g/cm^3
14 nAvo = 6.02e23;           % Avogadro number
15 mu0 = 1.257e-6;          % Vacuum permeability, H/m
16 muB = 9.27e-24;          % Bohr magneton, J/T
17
18 NVppm = 16;               % ppm of NVs in diamond
19 NVratio = NVppm*1e-6;     % Ratio of NV centers
20 nCarbon = (dDensity/12)*nAvo; % Carbon atoms in 1cm^3
21 nNV = nCarbon*NVRatio;    % NVs in in 1cm^3
22 nSpin = nNV/4;           % Resonant spins in 1cm^3
23 dSpin = 0.01/nSpin^(1/3); % Distance between nearest spins, m
24
25 Bfield = 4/3*muB*mu0/(4*pi*dSpin^3); % Bfield at next spin, factor ...
    4/3 is average of one fast two slow axis of spin coupling
26 freq = 28e9*Bfield;      % Zeeman shift, corresponds to flip-flop rate
27
28 NAobj = 0.82;            % NA of objective
29 lambda = 532e-9;         % Laser wavelength
30 omega0 = lambda/(pi*NAobj); % Laser focus radius
31
32 %%%%%%%%%%%%%%%%%%%%%%%%%%%%%%%%%%%%%%%%%%%%%%%%%%%%%%%%%%%%%%%%%%%%%%%%%
33 % Parameters and functions
34 %%%%%%%%%%%%%%%%%%%%%%%%%%%%%%%%%%%%%%%%%%%%%%%%%%%%%%%%%%%%%%%%%%%%%%%%%
35
36 nPixel = length(x);
37 dx = (max(x) - min(x)) / (nPixel - 1); % Pixel spacing in m

```

```

38 xRatio = distanceSpins / dx;           % NV distance, in pixels
39
40 %%% Times and rates with respect to spin-spin interaction rate "freq"
41 loopsLaser = round(laserTime * freq); % Laser time
42 loopsNoLaser = round(timeTau * freq); % Waiting time tau
43 initRate = initRateHz / freq;         % Initialization rate
44
45 blurSigma = sqrt(2) * xRatio;          % Diffusion: sigma^2 = 2at
46 nBlurFunc = 8 * round(blurSigma) + 1; % Size of diffusion function
47
48 % Gaussian diffusion function for convolution of polarization
49 blurFunc = fspecial('gaussian',nBlurFunc,blurSigma);
50
51 omega0Pixel = omega0 / distanceSpins * xRatio; % Laser radius omega0
52 laserSigma = omega0Pixel / 2;           % Laser radius sigma
53
54 % Gaussian laser profile
55 laserFunc = fspecial('gaussian',nPixel,laserSigma);
56 % Scale with initialization rate
57 laserFunc = laserFunc * initRate / max(max(laserFunc));
58 % Correction for high rates
59 laserFunc = 1 - 1 ./ (1 + laserFunc);
60
61 polarization = zeros(nPixel,nPixel); % Create 2D polarization array
62
63 %%%%%%%%%%%%%%%%%%%%%%%%%%%%%%%%%%%%%%%%%%%%%%%%%%%%%%%%%%%%%%%%%%%%%%%%%
64 % During initialization pulse
65 % Spin polarization and diffusion
66 %%%%%%%%%%%%%%%%%%%%%%%%%%%%%%%%%%%%%%%%%%%%%%%%%%%%%%%%%%%%%%%%%%%%%%%%%
67
68 %%% Iterate between laser initialization and diffusion, small steps
69 for i = 1:loopsLaser
70     polarization = 1 - (1-polarization).*(1-laserFunc); % Initialization
71     polarization = conv2(polarization,blurFunc,'same'); % Diffusion
72 end
73
74 %%%%%%%%%%%%%%%%%%%%%%%%%%%%%%%%%%%%%%%%%%%%%%%%%%%%%%%%%%%%%%%%%%%%%%%%%
75 % After initialization pulse
76 % Only spin diffusion
77 %%%%%%%%%%%%%%%%%%%%%%%%%%%%%%%%%%%%%%%%%%%%%%%%%%%%%%%%%%%%%%%%%%%%%%%%%
78
79 % Only diffusion
80 for i = 1:loopsNoLaser
81     polarization = conv2(polarization,blurFunc,'same'); % Diffusion
82 end

```

B. Bibliography

- [1] H. London, G. R. Clarke, and E. Mendoza, “Osmotic pressure of ^3He in Liquid ^4He , with proposals for a refrigerator to work below 1 K ,” *Physical Review*, vol. 128, p. 1992, 1962. [Online]. Available: <https://doi.org/10.1103/physrev.128.1992>
- [2] P. C. Maurer, G. Kucsko, C. Latta, L. Jiang, N. Y. Yao, S. D. Bennett, F. Pastawski, D. Hunger, N. Chisholm, M. Markham, D. J. Twitchen, J. I. Cirac, and M. D. Lukin, “Room-temperature quantum bit memory exceeding one second,” *Science*, vol. 336, p. 1283, 2012. [Online]. Available: <https://doi.org/10.1126/science.1220513>
- [3] F. Jelezko, T. Gaebel, I. Popa, A. Gruber, and J. Wrachtrup, “Observation of coherent oscillations in a single electron spin,” *Physical Review Letters*, vol. 92, p. 076401, 2004. [Online]. Available: <https://doi.org/10.1103/physrevlett.92.076401>
- [4] B. M. Chernobrod and G. Berman, “Spin microscope based on optically detected magnetic resonance,” *Journal of Applied Physics*, vol. 97, p. 014903, 2005. [Online]. Available: <https://doi.org/10.1063/1.1829373>
- [5] J. A. Bert, B. Kalisky, C. Bell, M. Kim, Y. Hikita, H. Y. Hwang, and K. A. Moler, “Direct imaging of the coexistence of ferromagnetism and superconductivity at the $\text{LaAlO}_3/\text{SrTiO}_3$ interface,” *Nature Physics*, vol. 7, p. 767, 2011. [Online]. Available: <https://doi.org/10.1038/nphys2079>
- [6] T. Astner, J. Gugler, A. Angerer, S. Wald, S. Putz, N. J. Mauser, M. Trupke, H. Sumiya, S. Onoda, J. Isoya, J. Schmiedmayer, P. Mohn, and J. Majer, “Solid-state electron spin lifetime limited by phononic vacuum modes,” *Nature Materials*, vol. 17, p. 313, 2018. [Online]. Available: <https://doi.org/10.1038/s41563-017-0008-y>
- [7] P. Das, R. B. de Ouboter, and K. W. Taconis, “A realization of a London-Clarke-Mendoza type refrigerator,” in *Low Temperature Physics LT9*. Springer, 1965, p. 1253. [Online]. Available: https://doi.org/10.1007/978-1-4899-6443-4_133
- [8] G. Davies and M. F. Hamer, “Optical studies of the 1.945 eV vibronic band in diamond,” *Proceedings of the Royal Society A: Mathematical, Physical and Engineering Sciences*, vol. 348, p. 285, 1976. [Online]. Available: <https://doi.org/10.1098/rspa.1976.0039>
- [9] G. Balasubramanian, I. Y. Chan, R. Kolesov, M. Al-Hmoud, J. Tisler, C. Shin, C. Kim, A. Wojcik, P. R. Hemmer, A. Krueger, T. Hanke, A. Leitenstorfer, R. Bratschitsch, F. Jelezko, and J. Wrachtrup, “Nanoscale

- imaging magnetometry with diamond spins under ambient conditions,” *Nature*, vol. 455, p. 648, 2008. [Online]. Available: <https://doi.org/10.1038/nature07278>
- [10] P. Maletinsky, S. Hong, M. S. Grinolds, B. Hausmann, M. D. Lukin, R. L. Walsworth, M. Loncar, and A. Yacoby, “A robust scanning diamond sensor for nanoscale imaging with single nitrogen-vacancy centres,” *Nature Nanotechnology*, vol. 7, p. 320, 2012. [Online]. Available: <https://doi.org/10.1038/nnano.2012.50>
- [11] P. Appel, B. J. Shields, T. Kosub, N. Hedrich, R. Hübner, J. Faßbender, D. Makarov, and P. Maletinsky, “Nanomagnetism of magnetoelectric granular thin-film antiferromagnets,” *Nano Letters*, vol. 19, p. 1682, 2019. [Online]. Available: <https://doi.org/10.1021/acs.nanolett.8b04681>
- [12] L. Thiel, Z. Wang, M. A. Tschudin, D. Rohner, I. Gutiérrez-Lezama, N. Ubrig, M. Gibertini, E. Giannini, A. F. Morpurgo, and P. Maletinsky, “Probing magnetism in 2D materials at the nanoscale with single-spin microscopy,” *Science*, vol. 364, p. 973, 2019. [Online]. Available: <https://doi.org/10.1126/science.aav6926>
- [13] L. Thiel, D. Rohner, M. Ganzhorn, P. Appel, E. Neu, B. Müller, R. Kleiner, D. Koelle, and P. Maletinsky, “Quantitative nanoscale vortex imaging using a cryogenic quantum magnetometer,” *Nature Nanotechnology*, vol. 11, p. 677, 2016. [Online]. Available: <https://doi.org/10.1038/nnano.2016.63>
- [14] J.-P. Tetienne, N. Dontschuk, D. A. Broadway, A. Stacey, D. A. Simpson, and L. C. L. Hollenberg, “Quantum imaging of current flow in graphene,” *Science Advances*, vol. 3, p. e1602429, 2017. [Online]. Available: <https://doi.org/10.1126/sciadv.1602429>
- [15] D. Rohner, L. Thiel, B. Müller, M. Kasperczyk, R. Kleiner, D. Koelle, and P. Maletinsky, “Real-space probing of the local magnetic response of thin-film superconductors using single spin magnetometry,” *Sensors*, vol. 18, p. 3790, 2018. [Online]. Available: <https://doi.org/10.3390/s18113790>
- [16] N. Reyren, S. Thiel, A. D. Caviglia, L. F. Kourkoutis, G. Hammerl, C. Richter, C. W. Schneider, T. Kopp, A.-S. Ruetschi, D. Jaccard, M. Gabay, D. A. Muller, J.-M. Triscone, and J. Mannhart, “Superconducting interfaces between insulating oxides,” *Science*, vol. 317, p. 1196, 2007. [Online]. Available: <https://doi.org/10.1126/science.1146006>
- [17] M. Golor, S. Wessel, and M. J. Schmidt, “Quantum nature of edge magnetism in graphene,” *Physical Review Letters*, vol. 112, p. 046601, 2014. [Online]. Available: <https://doi.org/10.1103/physrevlett.112.046601>
- [18] F. Kidwingira, J. D. Strand, D. J. V. Harlingen, and Y. Maeno, “Dynamical superconducting order parameter domains in Sr_2RuO_4 ,” *Science*, vol. 314, p. 1267, 2006. [Online]. Available: <https://doi.org/10.1126/science.1133239>

-
- [19] S. B. Chung, H. Bluhm, and E.-A. Kim, “Stability of half-quantum vortices in $p_x + ip_y$ superconductors,” *Physical Review Letters*, vol. 99, p. 197002, 2007. [Online]. Available: <https://doi.org/10.1103/physrevlett.99.197002>
- [20] The nobel prize in physics 1913 - Heike Kamerlingh Onnes. NobelPrize.org. [Online]. Available: <https://www.nobelprize.org/prizes/physics/1913/summary/>
- [21] J. C. Wheatley, O. E. Vilches, and W. R. Abel, “Principles and methods of dilution refrigeration,” *Physics Physique Fizika*, vol. 4, p. 1, 1968. [Online]. Available: <https://doi.org/10.1103/physicsphysiquefizika.4.1>
- [22] N. Bar-Gill, L. M. Pham, A. Jarmola, D. Budker, and R. L. Walsworth, “Solid-state electronic spin coherence time approaching one second,” *Nature Communications*, vol. 4, p. 1743, 2013. [Online]. Available: <https://doi.org/10.1038/ncomms2771>
- [23] P. Appel, E. Neu, M. Ganzhorn, A. Barfuss, M. Batzer, M. Gratz, A. Tschöpe, and P. Maletinsky, “Fabrication of all diamond scanning probes for nanoscale magnetometry,” *Review of Scientific Instruments*, vol. 87, p. 063703, 2016. [Online]. Available: <https://doi.org/10.1063/1.4952953>
- [24] M. Pelliccione, A. Jenkins, P. Ovarthaiyapong, C. Reetz, E. Emmanouilidou, N. Ni, and A. C. B. Jayich, “Scanned probe imaging of nanoscale magnetism at cryogenic temperatures with a single-spin quantum sensor,” *Nature Nanotechnology*, vol. 11, p. 700, 2016. [Online]. Available: <https://doi.org/10.1038/nnano.2016.68>
- [25] K. Ishida, H. Mukuda, Y. Kitaoka, K. Asayama, Z. Q. Mao, Y. Mori, and Y. Maeno, “Spin-triplet superconductivity in Sr_2RuO_4 identified by ^{17}O Knight shift,” *Nature*, vol. 396, p. 658, 1998. [Online]. Available: <https://doi.org/10.1038/25315>
- [26] L. Li, C. Richter, J. Mannhart, and R. C. Ashoori, “Coexistence of magnetic order and two-dimensional superconductivity at $\text{LaAlO}_3/\text{SrTiO}_3$ interfaces,” *Nature Physics*, vol. 7, p. 762, 2011. [Online]. Available: <https://doi.org/10.1038/nphys2080>
- [27] J. A. Bert, K. C. Nowack, B. Kalisky, H. Noad, J. R. Kirtley, C. Bell, H. K. Sato, M. Hosoda, Y. Hikita, H. Hwang, and K. A. Moler, “Gate-tuned superfluid density at the superconducting $\text{LaAlO}_3/\text{SrTiO}_3$ interface,” *Physical Review B*, vol. 86, p. 060503, 2012. [Online]. Available: <https://doi.org/10.1103/physrevb.86.060503>
- [28] R. Schirhagl, K. Chang, M. Loretz, and C. L. Degen, “Nitrogen-vacancy centers in diamond: Nanoscale sensors for physics and biology,” *Annual Review of Physical Chemistry*, vol. 65, p. 83, 2014. [Online]. Available: <https://doi.org/10.1146/annurev-physchem-040513-103659>
- [29] D. Vasyukov, Y. Anahory, L. Embon, D. Halbertal, J. Cuppens, L. Neeman, A. Finkler, Y. Segev, Y. Myasoedov, M. L. Rappaport, M. E. Huber, and E. Zeldov, “A scanning superconducting quantum interference device with

- single electron spin sensitivity,” *Nature Nanotechnology*, vol. 8, p. 639, 2013. [Online]. Available: <https://doi.org/10.1038/nnano.2013.169>
- [30] G. Frossati, “Experimental techniques: Methods for cooling below 300 mK,” *Journal of Low Temperature Physics*, vol. 87, p. 595, 1992. [Online]. Available: <https://doi.org/10.1007/bf00114918>
- [31] L. Thiel, “Nanoscale magnetometry with a single spin in diamond at cryogenic temperatures,” Ph.D. dissertation, University of Basel, 2019. [Online]. Available: <https://doi.org/10.5451/unibas-007110315>
- [32] P. C. L. Tai, M. R. Beasley, and M. Tinkham, “Anisotropy of the penetration depth in superconducting tin,” *Physical Review B*, vol. 11, p. 411, 1975. [Online]. Available: <https://doi.org/10.1103/physrevb.11.411>
- [33] E. Brandt, “Flux distribution and penetration depth measured by muon spin rotation in high- t_c superconductors,” *Physical Review B*, vol. 37, p. 2349, 1988. [Online]. Available: <https://doi.org/10.1103/physrevb.37.2349>
- [34] Y. J. Uemura, A. Keren, L. P. Le, G. M. Luke, B. J. Sternlieb, W. D. Wu, J. H. Brewer, R. L. Whetten, S. M. Huang, S. Lin, R. B. Kaner, F. Diederich, S. Donovan, G. Grüner, and K. Holczer, “Magnetic-field penetration depth in K_3C_6O measured by muon spin relaxation,” *Nature*, vol. 352, p. 605, 1991. [Online]. Available: <https://doi.org/10.1038/352605a0>
- [35] D. N. Basov, R. Liang, D. A. Bonn, W. N. Hardy, B. Dabrowski, M. Quijada, D. B. Tanner, J. P. Rice, D. M. Ginsberg, and T. Timusk, “In-plane anisotropy of the penetration depth in $YBa_2Cu_3O_{7-x}$ and $YBa_2Cu_4O_8$ superconductors,” *Physical Review Letters*, vol. 74, p. 598, 1995. [Online]. Available: <https://doi.org/10.1103/physrevlett.74.598>
- [36] C. Panagopoulos, J. R. Cooper, and T. Xiang, “Systematic behavior of the in-plane penetration depth in d -wave cuprates,” *Physical Review B*, vol. 57, p. 13422, 1998. [Online]. Available: <https://doi.org/10.1103/physrevb.57.13422>
- [37] T. Pereg-Barnea, P. J. Turner, R. Harris, G. K. Mullins, J. S. Bobowski, M. Raudsepp, R. Liang, D. A. Bonn, and W. N. Hardy, “Absolute values of the london penetration depth in $YBa_2Cu_3O_{6+y}$ measured by zero field ESR spectroscopy on Gd doped single crystals,” *Physical Review B*, vol. 69, p. 184513, 2004. [Online]. Available: <https://doi.org/10.1103/physrevb.69.184513>
- [38] M. Tinkham, *Introduction to Superconductivity*. Dover Publications, 2004.
- [39] J. Bardeen, L. N. Cooper, and J. R. Schrieffer, “Microscopic theory of superconductivity,” *Physical Review*, vol. 106, p. 162, 1957. [Online]. Available: <https://doi.org/10.1103/physrev.106.162>
- [40] A. . A. Abrikosov, “The magnetic properties of superconducting alloys,” *Journal of Physics and Chemistry of Solids*, vol. 2, p. 199, 1957. [Online]. Available: [https://doi.org/10.1016/0022-3697\(57\)90083-5](https://doi.org/10.1016/0022-3697(57)90083-5)

-
- [41] V. V. Moshchalkov and J. Fritzsche, *Nanostructured Superconductors*. World Scientific, 2011. [Online]. Available: <https://doi.org/10.1142/8132>
- [42] A. Gauzzi, B. J. Jönsson-Åkerman, A. Clerc-Dubois, and D. Pavuna, “Scaling between superconducting critical temperature and structural coherence length in $\text{YBa}_2\text{Cu}_3\text{O}_{6.9}$ films,” *Europhysics Letters (EPL)*, vol. 51, p. 667, 2000. [Online]. Available: <https://doi.org/10.1209/epl/i2000-00390-9>
- [43] D. Sivia, *Data Analysis: A Bayesian Tutorial. For Scientists and Engineers*. Oxford University Press, 2006.
- [44] B. J. Roth, N. G. Sepulveda, and J. P. Wikswo, “Using a magnetometer to image a two-dimensional current distribution,” *Journal of Applied Physics*, vol. 65, p. 361, 1989. [Online]. Available: <https://doi.org/10.1063/1.342549>
- [45] V. S. Stolyarov, I. S. Veshchunov, S. Y. Grebenchuk, D. S. Baranov, I. A. Golovchanskiy, A. G. Shishkin, N. Zhou, Z. Shi, X. Xu, S. Pyon, Y. Sun, W. Jiao, G.-H. Cao, L. Y. Vinnikov, A. A. Golubov, T. Tamegai, A. I. Buzdin, and D. Roditchev, “Domain Meissner state and spontaneous vortex-antivortex generation in the ferromagnetic superconductor $\text{EuFe}_2(\text{As}_{0.79}\text{P}_{0.21})_2$,” *Science Advances*, vol. 4, p. eaat1061, 2018. [Online]. Available: <https://doi.org/10.1126/sciadv.aat1061>
- [46] L. Embon, Y. Anahory, Ž. Jelić, E. O. Lachman, Y. Myasoedov, M. E. Huber, G. P. Mikitik, A. V. Silhanek, M. V. Milošević, A. Gurevich, and E. Zeldov, “Imaging of super-fast dynamics and flow instabilities of superconducting vortices,” *Nature Communications*, vol. 8, p. 85, 2017. [Online]. Available: <https://doi.org/10.1038/s41467-017-00089-3>
- [47] L. Embon, Y. Anahory, A. Suhov, D. Halbertal, J. Cuppens, A. Yakovenko, A. Uri, Y. Myasoedov, M. L. Rappaport, M. E. Huber, A. Gurevich, and E. Zeldov, “Probing dynamics and pinning of single vortices in superconductors at nanometer scales,” *Scientific Reports*, vol. 5, p. 7598, 2015. [Online]. Available: <https://doi.org/10.1038/srep07598>
- [48] L. Ceccarelli, D. Vasyukov, M. Wyss, G. Romagnoli, N. Rossi, L. Moser, and M. Poggio, “Imaging pinning and expulsion of individual superconducting vortices in amorphous MoSi thin films,” *Physical Review B*, vol. 100, p. 104504, 2019. [Online]. Available: <https://doi.org/10.1103/physrevb.100.104504>
- [49] U. Essmann and H. Träuble, “The direct observation of individual flux lines in type II superconductors,” *Physics Letters A*, vol. 24, p. 526, 1967. [Online]. Available: [https://doi.org/10.1016/0375-9601\(67\)90819-5](https://doi.org/10.1016/0375-9601(67)90819-5)
- [50] S. J. Bending, “Local magnetic probes of superconductors,” *Advances in Physics*, vol. 48, p. 449, 1999. [Online]. Available: <https://doi.org/10.1080/000187399243437>
- [51] G. Stan, S. B. Field, and J. M. Martinis, “Critical field for complete vortex expulsion from narrow superconducting strips,” *Physical Review Letters*, vol. 92, 2004.

- [52] H. F. Hess, R. B. Robinson, R. C. Dynes, J. M. Valles, and J. V. Waszczak, "Scanning-tunneling-microscope observation of the Abrikosov flux lattice and the density of states near and inside a fluxoid," *Physical Review Letters*, vol. 62, p. 214, 1989. [Online]. Available: <https://doi.org/10.1103/physrevlett.62.214>
- [53] J. E. Hoffman, "A four unit cell periodic pattern of quasi-particle states surrounding vortex cores in $\text{Bi}_2\text{Sr}_2\text{CaCu}_2\text{O}_{8+\delta}$," *Science*, vol. 295, p. 466, 2002. [Online]. Available: <https://doi.org/10.1126/science.1066974>
- [54] Ø. Fischer, M. Kugler, I. Maggio-Aprile, C. Berthod, and C. Renner, "Scanning tunneling spectroscopy of high-temperature superconductors," *Reviews of Modern Physics*, vol. 79, p. 353, 2007. [Online]. Available: <https://doi.org/10.1103/revmodphys.79.353>
- [55] F. Tafuri, J. R. Kirtley, P. G. Medaglia, P. Orgiani, and G. Balestrino, "Magnetic imaging of Pearl vortices in artificially layered $(\text{Ba}_{0.9}\text{Nd}_{0.1}\text{CuO}_{2+x})_m/(\text{CaCuO}_2)_n$ systems," *Physical Review Letters*, vol. 92, p. 157006, 2004. [Online]. Available: <https://doi.org/10.1103/physrevlett.92.157006>
- [56] O. M. Auslaender, L. Luan, E. W. J. Straver, J. E. Hoffman, N. C. Koshnick, E. Zeldov, D. A. Bonn, R. Liang, W. N. Hardy, and K. A. Moler, "Mechanics of individual isolated vortices in a cuprate superconductor," *Nature Physics*, vol. 5, p. 35, 2008. [Online]. Available: <https://doi.org/10.1038/nphys1127>
- [57] L. Luan, O. M. Auslaender, D. A. Bonn, R. Liang, W. N. Hardy, and K. A. Moler, "Magnetic force microscopy study of interlayer kinks in individual vortices in the underdoped cuprate superconductor $\text{YBa}_2\text{Cu}_3\text{O}_{6+x}$," *Physical Review B*, vol. 79, p. 214530, 2009. [Online]. Available: <https://doi.org/10.1103/physrevb.79.214530>
- [58] A. M. Chang, H. D. Hallen, L. Harriott, H. F. Hess, H. L. Kao, J. Kwo, R. E. Miller, R. Wolfe, J. van der Ziel, and T. Y. Chang, "Scanning hall probe microscopy," *Applied Physics Letters*, vol. 61, p. 1974, 1992. [Online]. Available: <https://doi.org/10.1063/1.108334>
- [59] J. Pearl, "Current distribution in superconducting films carrying quantized fluxoids," *Applied Physics Letters*, vol. 5, p. 65, 1964. [Online]. Available: <https://doi.org/10.1063/1.1754056>
- [60] G. Carneiro and E. H. Brandt, "Vortex lines in films: Fields and interactions," *Physical Review B*, vol. 61, p. 6370, 2000. [Online]. Available: <https://doi.org/10.1103/physrevb.61.6370>
- [61] J. Ge, J. Gutierrez, J. Cuppens, and V. V. Moshchalkov, "Observation of single flux quantum vortices in the intermediate state of a type-i superconducting film," *Physical Review B*, vol. 88, p. 174503, 2013. [Online]. Available: <https://doi.org/10.1103/physrevb.88.174503>

-
- [62] J. D. A. Wood, J.-P. Tetienne, D. A. Broadway, L. T. Hall, D. A. Simpson, A. Stacey, and L. C. L. Hollenberg, “Microwave-free nuclear magnetic resonance at molecular scales,” *Nature Communications*, vol. 8, p. 15950, 2017. [Online]. Available: <https://doi.org/10.1038/ncomms15950>
- [63] L. Rondin, J.-P. Tetienne, T. Hingant, J.-F. Roch, P. Maletinsky, and V. Jacques, “Magnetometry with nitrogen-vacancy defects in diamond,” *Reports on Progress in Physics*, vol. 77, p. 056503, 2014. [Online]. Available: <https://doi.org/10.1088/0034-4885/77/5/056503>
- [64] D. Rohner, J. Happacher, P. Reiser, M. A. Tschudin, A. Tallaire, J. Achard, B. J. Shields, and P. Maletinsky, “(111)-oriented, single crystal diamond tips for nanoscale scanning probe imaging of out-of-plane magnetic fields,” *Applied Physics Letters*, vol. 115, p. 192401, 2019. [Online]. Available: <https://doi.org/10.1063/1.5127101>
- [65] E. A. Lima and B. P. Weiss, “Obtaining vector magnetic field maps from single-component measurements of geological samples,” *Journal of Geophysical Research*, vol. 114, p. B06102, 2009. [Online]. Available: <https://doi.org/10.1029/2008jb006006>
- [66] F. Casola, T. van der Sar, and A. Yacoby, “Probing condensed matter physics with magnetometry based on nitrogen-vacancy centres in diamond,” *Nature Reviews Materials*, vol. 3, p. 17088, 2018. [Online]. Available: <https://doi.org/10.1038/natrevmats.2017.88>
- [67] E. Neu, P. Appel, M. Ganzhorn, J. Miguel-Sánchez, M. Lesik, V. Mille, V. Jacques, A. Tallaire, J. Achard, and P. Maletinsky, “Photonic nanostructures on (111)-oriented diamond,” *Applied Physics Letters*, vol. 104, p. 153108, 2014. [Online]. Available: <https://doi.org/10.1063/1.4871580>
- [68] J. R. Maze, A. Gali, E. Togan, Y. Chu, A. Trifonov, E. Kaxiras, and M. D. Lukin, “Properties of nitrogen-vacancy centers in diamond: the group theoretic approach,” *New Journal of Physics*, vol. 13, p. 025025, 2011. [Online]. Available: <https://doi.org/10.1088/1367-2630/13/2/025025>
- [69] T. P. M. Alegre, C. Santori, G. Medeiros-Ribeiro, and R. G. Beausoleil, “Polarization-selective excitation of nitrogen vacancy centers in diamond,” *Physical Review B*, vol. 76, p. 165205, 2007. [Online]. Available: <https://doi.org/10.1103/PhysRevB.76.165205>
- [70] M. Lesik, J.-P. Tetienne, A. Tallaire, J. Achard, V. Mille, A. Gicquel, J.-F. Roch, and V. Jacques, “Perfect preferential orientation of nitrogen-vacancy defects in a synthetic diamond sample,” *Applied Physics Letters*, vol. 104, p. 113107, 2014. [Online]. Available: <https://doi.org/10.1063/1.4869103>
- [71] J.-P. Tetienne, L. Rondin, P. Spinicelli, M. Chipaux, T. Debuisschert, J.-F. Roch, and V. Jacques, “Magnetic-field-dependent photodynamics of single NV defects in diamond: an application to qualitative all-optical magnetic imaging,” *New Journal of Physics*, vol. 14, p. 103033, 2012. [Online]. Available: <https://doi.org/10.1088/1367-2630/14/10/103033>

- [72] Y. Zhang, Y.-W. Tan, H. L. Stormer, and P. Kim, “Experimental observation of the quantum Hall effect and Berry’s phase in graphene,” *Nature*, vol. 438, p. 201, 2005. [Online]. Available: <https://doi.org/10.1038/nature04235>
- [73] N. Nagaosa and Y. Tokura, “Topological properties and dynamics of magnetic skyrmions,” *Nature Nanotechnology*, vol. 8, p. 899, 2013. [Online]. Available: <https://doi.org/10.1038/nnano.2013.243>
- [74] N. Hedrich and B. Shields, “Manuscript in preparation,” 2019.
- [75] J. Bleuse, J. Claudon, M. Creasey, N. S. Malik, J.-M. Gérard, I. Maksymov, J.-P. Hugonin, and P. Lalanne, “Inhibition, enhancement, and control of spontaneous emission in photonic nanowires,” *Physical Review Letters*, vol. 106, p. 103601, 2011. [Online]. Available: <https://doi.org/10.1103/physrevlett.106.103601>
- [76] A. Barfuss, M. Kasperczyk, J. Kölbl, and P. Maletinsky, “Spin-stress and spin-strain coupling in diamond-based hybrid spin oscillator systems,” *Physical Review B*, vol. 99, p. 174102, 2019. [Online]. Available: <https://doi.org/10.1103/PhysRevB.99.174102>
- [77] J.-P. Tetienne, T. Hingant, J.-V. Kim, L. H. Diez, J.-P. Adam, K. Garcia, J.-F. Roch, S. Rohart, A. Thiaville, D. Ravelosona, and V. Jacques, “Nanoscale imaging and control of domain-wall hopping with a nitrogen-vacancy center microscope,” *Science*, vol. 344, p. 1366, 2014. [Online]. Available: <https://doi.org/10.1126/science.1250113>
- [78] J.-P. Tetienne, T. Hingant, L. J. Martínez, S. Rohart, A. Thiaville, L. H. Diez, K. Garcia, J.-P. Adam, J.-V. Kim, J.-F. Roch, I. M. Miron, G. Gaudin, L. Vila, B. Ocker, D. Ravelosona, and V. Jacques, “The nature of domain walls in ultrathin ferromagnets revealed by scanning nanomagnetometry,” *Nature Communications*, vol. 6, p. 6733, 2015. [Online]. Available: <https://doi.org/https://doi.org/10.1038/ncomms7733>
- [79] T. Hingant, J.-P. Tetienne, L. J. Martínez, K. Garcia, D. Ravelosona, J.-F. Roch, and V. Jacques, “Measuring the magnetic moment density in patterned ultrathin ferromagnets with submicrometer resolution,” *Phys. Rev. Applied*, vol. 4, p. 014003, 2015. [Online]. Available: <https://doi.org/10.1103/PhysRevApplied.4.014003>
- [80] A. Ohtomo and H. Y. Hwang, “A high-mobility electron gas at the $\text{LaAlO}_3/\text{SrTiO}_3$ heterointerface,” *Nature*, vol. 427, p. 423, 2004. [Online]. Available: <https://doi.org/10.1038/nature02308>
- [81] A. D. Caviglia, S. Gariglio, N. Reyren, D. Jaccard, T. Schneider, M. Gabay, S. Thiel, G. Hammerl, J. Mannhart, and J.-M. Triscone, “Electric field control of the $\text{LaAlO}_3/\text{SrTiO}_3$ interface ground state,” *Nature*, vol. 456, p. 624, 2008. [Online]. Available: <https://doi.org/10.1038/nature07576>
- [82] A. Joshua, S. Pecker, J. Ruhman, E. Altman, and S. Ilani, “A universal critical density underlying the physics of electrons at the $\text{LaAlO}_3/\text{SrTiO}_3$ interface,” *Nature Communications*, vol. 3, p. 1129, 2012. [Online]. Available: <https://doi.org/10.1038/ncomms2116>

-
- [83] B. Kalisky, E. M. Spanton, H. Noad, J. R. Kirtley, K. C. Nowack, C. Bell, H. K. Sato, M. Hosoda, Y. Xie, Y. Hikita, C. Woltmann, G. Pfanzelt, R. Jany, C. Richter, H. Y. Hwang, J. Mannhart, and K. A. Moler, "Locally enhanced conductivity due to the tetragonal domain structure in $\text{LaAlO}_3/\text{SrTiO}_3$ heterointerfaces," *Nature Materials*, vol. 12, p. 1091, 2013. [Online]. Available: <https://doi.org/10.1038/nmat3753>
- [84] P. Zubko, S. Gariglio, M. Gabay, P. Ghosez, and J.-M. Triscone, "Interface physics in complex oxide heterostructures," *Annual Review of Condensed Matter Physics*, vol. 2, p. 141, 2011. [Online]. Available: <https://doi.org/10.1146/annurev-conmatphys-062910-140445>
- [85] J. W. Park, D. F. Bogorin, C. Cen, D. A. Felker, Y. Zhang, C. T. Nelson, C. W. Bark, C. M. Folkman, X. Q. Pan, M. S. Rzhowski, J. Levy, and C. B. Eom, "Creation of a two-dimensional electron gas at an oxide interface on silicon," *Nature Communications*, vol. 1, p. 94, 2010. [Online]. Available: <https://doi.org/10.1038/ncomms1096>
- [86] S. Gariglio, N. Reyren, A. D. Caviglia, and J.-M. Triscone, "Superconductivity at the $\text{LaAlO}_3/\text{SrTiO}_3$ interface," *Journal of Physics: Condensed Matter*, vol. 21, p. 164213, 2009. [Online]. Available: <https://doi.org/10.1088/0953-8984/21/16/164213>
- [87] N. Nakagawa, H. Y. Hwang, and D. A. Muller, "Why some interfaces cannot be sharp," *Nature Materials*, vol. 5, p. 204, 2006. [Online]. Available: <https://doi.org/10.1038/nmat1569>
- [88] F. Bi, M. Huang, S. Ryu, H. Lee, C.-W. Bark, C.-B. Eom, P. Irvin, and J. Levy, "Room-temperature electronically-controlled ferromagnetism at the $\text{LaAlO}_3/\text{SrTiO}_3$ interface," *Nature Communications*, vol. 5, p. 5019, 2014. [Online]. Available: <https://doi.org/10.1038/ncomms6019>
- [89] N. Pavlenko, T. Kopp, E. Y. Tsybal, G. A. Sawatzky, and J. Mannhart, "Magnetic and superconducting phases at the $\text{LaAlO}_3/\text{SrTiO}_3$ interface: The role of interfacial Ti 3d electrons," *Physical Review B*, vol. 85, p. 020407, 2012. [Online]. Available: <https://doi.org/10.1103/physrevb.85.020407>
- [90] M. Boselli, D. Li, W. Liu, A. Fête, S. Gariglio, and J.-M. Triscone, "Characterization of atomic force microscopy written conducting nanowires at $\text{LaAlO}_3/\text{SrTiO}_3$ interfaces," *Applied Physics Letters*, vol. 108, p. 061604, 2016. [Online]. Available: <https://doi.org/10.1063/1.4941817>
- [91] D. A. Dikin, M. Mehta, C. W. Bark, C. M. Folkman, C. B. Eom, and V. Chandrasekhar, "Coexistence of superconductivity and ferromagnetism in two dimensions," *Physical Review Letters*, vol. 107, p. 056802, 2011. [Online]. Available: <https://doi.org/10.1103/physrevlett.107.056802>
- [92] H.-L. Lu, Z.-M. Liao, L. Zhang, W.-T. Yuan, Y. Wang, X.-M. Ma, and D.-P. Yu, "Reversible insulator-metal transition of $\text{LaAlO}_3/\text{SrTiO}_3$ interface for nonvolatile memory," *Scientific Reports*, vol. 3, p. 2870, 2013. [Online]. Available: <https://doi.org/10.1038/srep02870>

- [93] A. Jarmola, V. M. Acosta, K. Jensen, S. Chemerisov, and D. Budker, “Temperature- and magnetic-field-dependent longitudinal spin relaxation in nitrogen-vacancy ensembles in diamond,” *Physical Review Letters*, vol. 108, p. 197601, 2012. [Online]. Available: <https://doi.org/10.1103/physrevlett.108.197601>
- [94] A. Ariyaratne, D. Bluvstein, B. A. Myers, and A. C. B. Jayich, “Nanoscale electrical conductivity imaging using a nitrogen-vacancy center in diamond,” *Nature Communications*, vol. 9, p. 2406, 2018. [Online]. Available: <https://doi.org/10.1038/s41467-018-04798-1>
- [95] M. Pelliccione, B. A. Myers, L. M. A. Pascal, A. Das, and A. C. B. Jayich, “Two-dimensional nanoscale imaging of Gadolinium spins via scanning probe relaxometry with a single spin in diamond,” *Physical Review Applied*, vol. 2, p. 054014, 2014. [Online]. Available: <https://doi.org/10.1103/physrevapplied.2.054014>
- [96] L. Childress and R. Hanson, “Diamond NV centers for quantum computing and quantum networks,” *MRS Bulletin*, vol. 38, p. 134, 2013. [Online]. Available: <https://doi.org/10.1557/mrs.2013.20>
- [97] S. Hong, M. S. Grinolds, L. M. Pham, D. L. Sage, L. Luan, R. L. Walsworth, and A. Yacoby, “Nanoscale magnetometry with NV centers in diamond,” *MRS Bulletin*, vol. 38, p. 155, 2013. [Online]. Available: <https://doi.org/10.1557/mrs.2013.23>
- [98] B. Myers, A. Ariyaratne, and A. B. Jayich, “Double-quantum spin-relaxation limits to coherence of near-surface nitrogen-vacancy centers,” *Physical Review Letters*, vol. 118, p. 197201, 2017. [Online]. Available: <https://doi.org/10.1103/physrevlett.118.197201>
- [99] B. J. Shields, Q. P. Unterreithmeier, N. P. de Leon, H. Park, and M. D. Lukin, “Efficient readout of a single spin state in diamond via spin-to-charge conversion,” *Physical Review Letters*, vol. 114, p. 136402, 2015. [Online]. Available: <https://doi.org/10.1103/physrevlett.114.136402>
- [100] O. V. Yazyev, “Emergence of magnetism in graphene materials and nanostructures,” *Reports on Progress in Physics*, vol. 73, p. 056501, 2010. [Online]. Available: <https://doi.org/10.1088/0034-4885/73/5/056501>
- [101] I. V. Kukushkin, K. v. Klitzing, and K. Eberl, “Spin polarization of composite fermions: Measurements of the Fermi energy,” *Physical Review Letters*, vol. 82, p. 3665, 1999. [Online]. Available: <https://doi.org/10.1103/physrevlett.82.3665>
- [102] O. Stern, N. Freytag, A. Fay, W. Dietsche, J. Smet, K. von Klitzing, D. Schuh, and W. Wegscheider, “NMR study of the electron spin polarization in the fractional quantum Hall effect of a single quantum well: Spectroscopic evidence for domain formation,” *Physical Review B*, vol. 70, p. 075318, 2004. [Online]. Available: <https://doi.org/10.1103/physrevb.70.075318>

-
- [103] A. F. Young, C. R. Dean, L. Wang, H. Ren, P. Cadden-Zimansky, K. Watanabe, T. Taniguchi, J. Hone, K. L. Shepard, and P. Kim, “Spin and valley quantum Hall ferromagnetism in graphene,” *Nature Physics*, vol. 8, p. 550, 2012. [Online]. Available: <https://doi.org/10.1038/nphys2307>
- [104] K. D. Nelson, “Odd-parity superconductivity in Sr_2RuO_4 ,” *Science*, vol. 306, p. 1151, 2004. [Online]. Available: <https://doi.org/10.1126/science.1103881>
- [105] M. Rice, “Superconductivity with a twist,” *Science*, vol. 314, p. 1248, 2006. [Online]. Available: <https://doi.org/10.1126/science.1134921>
- [106] C. W. Hicks, J. R. Kirtley, T. M. Lippman, N. C. Koshnick, M. E. Huber, Y. Maeno, W. M. Yuhasz, M. B. Maple, and K. A. Moler, “Limits on superconductivity-related magnetization in Sr_2RuO_4 and $\text{PrOs}_4\text{Sb}_{12}$ from scanning SQUID microscopy,” *Physical Review B*, vol. 81, p. 214501, 2010. [Online]. Available: <https://doi.org/10.1103/physrevb.81.214501>
- [107] C. Santori, P. Tamarat, P. Neumann, J. Wrachtrup, D. Fattal, R. G. Beausoleil, J. Rabeau, P. Olivero, A. D. Greentree, S. Prawer, F. Jelezko, and P. Hemmer, “Coherent population trapping of single spins in diamond under optical excitation,” *Physical Review Letters*, vol. 97, p. 247401, 2006. [Online]. Available: <https://doi.org/10.1103/physrevlett.97.247401>
- [108] C. G. Yale, B. B. Buckley, D. J. Christle, G. Burkard, F. J. Heremans, L. C. Bassett, and D. D. Awschalom, “All-optical control of a solid-state spin using coherent dark states,” *Proceedings of the National Academy of Sciences*, vol. 110, p. 7595, 2013. [Online]. Available: <https://doi.org/10.1073/pnas.1305920110>
- [109] J. N. Becker, B. Pingault, D. Groß, M. Gündoğan, N. Kukharchyk, M. Markham, A. Edmonds, M. Atatüre, P. Bushev, and C. Becher, “All-optical control of the silicon-vacancy spin in diamond at millikelvin temperatures,” *Physical Review Letters*, vol. 120, p. 053603, 2018. [Online]. Available: <https://doi.org/10.1103/physrevlett.120.053603>
- [110] D. D. Sukachev, A. Sipahigil, C. T. Nguyen, M. K. Bhaskar, R. E. Evans, F. Jelezko, and M. D. Lukin, “Silicon-vacancy spin qubit in diamond: A quantum memory exceeding 10 ms with single-shot state readout,” *Physical Review Letters*, vol. 119, p. 223602, 2017. [Online]. Available: <https://doi.org/10.1103/physrevlett.119.223602>

Curriculum Vitae

Personal Details

Name	Dominik Rohner
Date of Birth	19 November 1988
Place of Origin	Basel, Switzerland
Address	Lothringerstrasse 87, 4056 Basel
Email	dominik.rohner@unibas.ch

Education

2015-2020	University of Basel, PhD in Experimental Physics
2011-2013	University of Basel, Master of Science in Nanoscience
2008-2011	University of Basel, Bachelor of Science in Nanoscience
2005-2007	Gymnasium Oberwil BL, Matura

Publications

- [111] D. Rohner, J. Happacher, P. Reiser, M. A. Tschudin, A. Tallaire, J. Achard, B. J. Shields, and P. Maletinsky, “(111)-oriented, single crystal diamond tips for nanoscale scanning probe imaging of out-of-plane magnetic fields”, *Applied Physics Letters* **115**, 192401 (2019).
- [112] L. Thiel, Z. Wang, M. A. Tschudin, D. Rohner, I. Gutiérrez-Lezama, N. Ubrig, M. Gibertini, E. Giannini, A. F. Morpurgo, and P. Maletinsky, “Probing magnetism in 2D materials at the nanoscale with single spin microscopy”, *Science* **364**, 973 (2019)
- [113] V. M. Acosta, L. S. Bouchard, D. Budker, R. Folman, T. Lenz, P. Maletinsky, D. Rohner, Y. Schlüssel, L. Thiel, “Color centers in diamond as novel probes of superconductivity”, *Journal of Superconductivity and Novel Magnetism* **32**, 85 (2019)
- [114] D. Rohner*, L. Thiel*, B. Müller, M. Kasperczyk, R. Kleiner, D. Kölle, and P. Maletinsky, “Real-Space Probing of the Local Magnetic Response of Thin-Film Superconductors Using Single Spin Magnetometry”, *Sensors* **18**, 3790 (2018)
- [115] Y. Schlüssel, T. Lenz, D. Rohner, Y. Bar-Haim, L. Bougas, D. Groswasser, M. Kieschnick, E. Rozenberg, L. Thiel, A. Waxman, J. Meijer, P. Maletinsky, D. Budker, and R. Folman, “Wide-Field Imaging of Superconductor Vortices with Electron Spins in Diamond”, *Physical Review Applied* **10**, 034032 (2018)

- [116] L. Thiel, D. Rohner, M. Ganzhorn, P. Appel, E. Neu, B. Müller, R. Kleiner, D. Kölle, and P. Maletinsky, “Quantitative nanoscale vortex imaging using a cryogenic quantum magnetometer”, *Nature Nanotechnology* **11**, 677 (2016)
- [117] D. Riedel*, D. Rohner*, M. Ganzhorn, T. Kaldewey, P. Appel, E. Neu, R. Warburton, and P. Maletinsky, “Low-loss broadband antenna for efficient photon collection from a coherent spin in diamond,” *Physical Review Applied*, **2**, 064011, 2014.
- [118] L. Greuter, S. Starosielec, D. Najer, A. Ludwig, L. Duempelmann, D. Rohner, and R. J. Warburton, “A small mode volume tunable microcavity: Development and characterization,” *Applied Physics Letters*, **105**, 121105, 2014.

March 10, 2020